Behaviour of Magnesium Alloy Under Load-Control Cyclic Testing

by

Bahareh Marzbanrad

A thesis
presented to the University of Waterloo
in fulfillment of the
thesis requirement for the degree of
Master of Applied Science
in
Mechanical Engineering

Waterloo, Ontario, Canada, 2015

AUTHOR'S DECLARATION

I hereby declare that I am the sole author of this thesis. This is a true copy of the thesis, including any required final revisions, as accepted by my examiners.

I understand that my thesis may be made electronically available to the public.

Bahareh Marzbanrad

Abstract

The characterization of material fatigue behaviour is crucial in the design of mechanical components. Magnesium alloys, particularly wrought magnesium alloys, are one of the most interesting materials for mechanical components due to their superior physical and mechanical properties and have, therefore, been studied extensively. Primarily, evaluations of the fatigue characteristics of wrought magnesium alloys have been conducted under cyclic stress- and strain-control conditions. However, many engineering components are subjected to cyclic bending moments or load-control cyclic conditions. These conditions can be provided by a rotating bending test (RBT), which is usually employed to extract stress versus number of cycles until failure of the sample (S-N curve). On the other hand, the S-N curve is not sufficient to evaluate cyclic deformations of the material, especially for low-cycle fatigue regimes. To estimate the fatigue behaviour of the material, it is necessary to obtain stress and strain responses of the material under different range of bending moments in load-control condition. To date, however, the evolution of hysteresis curves during rotating bending experiments for asymmetric materials such as magnesium alloys has not been reported in the literature.

In the present study, for the first time, Fiber Bragg Grating (FBG) sensors were employed to measure the strain on AZ31B extrusion samples during RBT. First, the accuracy of strain measurement by the FBG sensor in the elastic and plastic regimes was investigated by comparing the FBG measured strain with that obtained by a standard extensometer during uniaxial pull-push test. Results confirmed that the FBG sensor was able to measure the strain up to 1.3%, accurately. In the next step, the strains of the specimens were measured under different bending moments of 2.5, 5, 6.5 Nm, during RBT. Based on these experiments, the strain amplitude of the samples was decreased with increasing the number of cycles in plastic regime until the sample was stabilized, however the strain response of the material under bending moment of 2.5 (in elastic regime) remained constant during the test.

To analyze applied stresses to the sample, particularly in the plastic deformation range, the proposed Variable Material Property (VMP) method was employed. In this model, the RBT was simulated by a fixed beam problem that was under alternative loading, and the stress-strain responses of the sample were predicted. Using this simulation method, the hysteresis loops of two critical top and bottom elements of the sample cross-section under different bending moments were obtained.

Finally, the strain of the sample during rotating bending, which was measured by the embedded FBG sensor, was replaced with the strains obtained from the modeling by fitting a mapping function. The

hysteresis obtained from combination of the modeling results and FBG experiments was relatively precise. To verify this claim, the stresses of the hysteresis loops were compared with the stresses obtained from the proposed strain-control pull-push tests in which, the strain on the sample was adjusted to be equal to the strain measured by the FBG sensor. The results of this test demonstrated that the stresses of the combined VMP and FBG hysteresis loops have good compatibility with the stress responses of the experiment. Therefore, the accuracy of the cyclic deformation hysteresis obtained using modeling and experimental results were confirmed under load-control conditions. Moreover, the fatigue life of the sample was calculated using the obtained hysteresis curve based on the energy approach. The predicted fatigue life of the AZ31B extrusion samples was in good agreement with published experimental data.

Acknowledgements

I would like to express my sincere gratitude to my supervisor, Professor Hamid Jahed, and my co-supervisor, Professor Ehsan Toyserkani, for their valuable supports, advice, and encouragement in the past two years.

I hereby express my gratitude to my thesis reviewing committee members, Professor Amir Khajepour and Professor Hyock Ju Kwon for their review, comments and suggestions.

I greatly appreciate my colleagues, Ali Roostaei, Elfaitori Ibrahim, Tian You Richard Liang, Mohammad Diab, and particularly Dr. Seyed Behzad Behravesh for their valuable advice and discussions. I am also thankful to Andy Barber for his technical supports.

I wish to thank Sarah Wallace who offered her valuable help on proofreading this thesis.

I am especially thankful to my husband, Ehsan, for his assistance, collaboration and encouragement, which made this research possible. I am also extremely thankful to my lovely daughter, Vania for her understanding and patience.

Finally, I must express my great appreciation to my parents for their sincere love, supports and encouragements through my studies. I would also like to wish my deepest gratitude to my dear brother, Mohammad, and sister Shekoofeh for their continued supports and motivation. This achievement would not have been possible without them. Thank you.

Dedicated to my parents

And

To my husband

And my daughter

Table of Contents

List of Figures

List of Tables

List of Abbreviations

RBT: Rotating Bending Test

RBM: Rotating Bending Machine

FBG: Fiber Bragg Grating

VMP: Variable Material Property

CSSC: Cyclic Stress-Strain Curve

Chapter 1

Introduction

1.1 Motivation

Optimal engineering design, which balances the highest possible efficiency with the fewest negative impacts, is indispensable for a modern world. Its importance can be highlighted by considering environmental issues such as air pollution, global warming and restrictions on fossil fuel resources. One of the most significant aspects of engineering design is the selection of materials to be used to meet the required mechanical, chemical and physical characteristics. Minimizing the weight of a mobile structure is a critical consideration in the material selection for fabrication because it can conserve energy and, as a consequence, reduce the environmental effects [1]. For several years, aluminum has been considered the best choice for mobile structures when compared to other metals and alloys, mainly due to its high strength to weight ratio. Therefore, aluminum and its alloys have been used extensively to modernize different industries, particularly those with mass production, such as automotive and aerospace [1]. However, increasing demands to address the aforementioned global environmental problems have motivated scientists to search for new alternatives to current structural materials. Their research has introduced new competitors to aluminum: magnesium and its alloys. Magnesium is the lightest commercial metallic element and has the eighth most abundant source on the earth, low energy consumption during extraction, refining, and forming, and remarkable properties such as its weight to strength ratio [2, 3]. The stupendous properties of this metal are enhanced by adding elements such as aluminum and zinc, resulting in new structural alloys referred to as the AZ group. Since wrought magnesium alloys, such as extrusion and rolled AZ31B, have superior mechanical properties in comparison to the others, they are preferred for use in load bearing components, especially in the automotive and aerospace industries [4]. Hence, the use of wrought magnesium alloys is rapidly increasing. With growing demand for employing these alloys, investigating how they behave under different scenarios is essential. Since the behaviour of magnesium and its alloys is not symmetric under tension and compression, more research that analyzes this complicated behaviour is required to achieve the desired optimum engineering design [5, 6].

A large number of industrial structures and automotive components are usually subjected to cyclic bending moments or cyclic loading, and even with low amounts of the applied loading, failure of the

components can occur after a period of time [7]. This type of failure is referred to as fatigue, one of the most important types of failure. Therefore, the study of wrought magnesium alloys' behaviour under cyclic loading, and the prediction of their fatigue life are areas of substantial research interest from the point of view of designers and manufacturers. The behaviour of these materials becomes more critical when they are used in aerospace or automotive industries as the mechanical failure of any parts is not only able to stop the performance of the machine, but cause unpredictable safety problems. However, the asymmetric behaviour of wrought magnesium alloys can also influence the fatigue behaviour of the materials. In real world applications, different modes of loading combined with their asymmetric behaviour can complicate the material response analysis under different conditions.

More recently, the fatigue properties and behaviour of wrought magnesium alloys have been investigated under strain control, stress control and load control conditions [8-16]. This has led to a significant amount of information about predicting fatigue life and analyzing fatigue behaviour. For example, strain and stress control fatigue tests have been widely performed for AZ31B extrusion, and its mechanical properties and fatigue behaviour have been studied in various strain and stress amplitudes. However, load control fatigue tests, which are conducted through rotating bending tests (RBT), have been restricted to obtaining stress versus life (S-N) curve in high-cycle regimes [17]. The RBT applies a stress gradient, rather than a uniform stress, across a cross section of the sample. This stress gradient begins from a maximum tensile stress on one side of the sample, reaches zero at the neutral axis, and then continues with compressive stress to a maximum compression at the other side of the sample. When the applied bending moment is high enough, plastic deformation occurs at the surface while the core of the sample experiences elastic deformation due to the magnitude of the applied bending. In the elastic regime, the applied bending moment is translated to normal stress through the elastic flexural formula and the number of cycles is recorded until failure occurs. The resultant S-N curve contains important data that can be used for engineering design, although it is not able to reflect all aspects of the fatigue failure of the material [17, 18]. For many structural parts, failure safe design criteria are defined by specific amounts of strain on the sample, whereas no strain measurement normally exists during load control fatigue tests. Therefore, to evaluate strain during cycles of RBT, it is necessary to employ an appropriate sensor, since the conventional strain gauge or extensometer cannot be utilized for this observation.

2

In this research, a Fiber Bragg Grating (FBG) sensor, a new generation of strain measurement sensor, is employed for measuring the strain of AZ31B extrusion samples during load-control RBT cycles. This sensor can provide in-situ strain measurement. The measurement is done locally by mounting the sensor on the curvature surface of the sample exactly where the maximum strain is induced. An FBG sensor can measure high strain precisely during the test; hence, it is able to evaluate the strain in both elastic and plastic regimes. The strain measurement during cyclic loading can provide additional data to analyze the characteristics of AZ31B extrusion under load-control cyclic tests. In addition to strain evaluation, it is also necessary to obtain the stress responses of the material in low cycle regimes, to comprehensively describe the fatigue behaviour of AZ31B.

The asymmetric behaviour of AZ31B extrusion can affect the stress distribution induced by the constant bending moment in a low cycle fatigue test. When the sample is plastically deformed, the maximum stresses on the sample's surface are not identical for the tension and compression parts, although the applied bending moment is almost constant. This complicated and unpredictable behaviour of AZ31B extrusion under load-control conditions can be investigated by using elasto-plastic analysis. To avoid the complexity of elasto-plastic analytical solutions, a Variable Material Property (VMP) method is proposed [19]. This method is a numerical simulation approach, which can be employed to calculate the applied stress when elastic or plastic deformation is observed in the sample. In this simulation method, the asymmetric and nonlinear behaviour of the material in the plastic regime is characterized using a simple linear elastic solution. Obtaining the cyclic deformation hysteresis of AZ31B extrusion is required for estimating the fatigue behaviour of the material under load control cyclic test conditions. This hysteresis is obtained by incorporating the experimental strains (FBG strain) and obtained stresses from modeling (VMP stress) under load-control RBT conditions. The stress-strain hysteresis obtained is employed to predict the fatigue life of AZ31B extrusion through the elastic and plastic strain energy estimation.

1.2 Thesis Objective

The cyclic behaviour of AZ31B extrusion magnesium alloy under load-control fatigue test conditions is studied through the incorporation of FBG sensors into the coupon-testing samples. The objectives of this research are as follows:

- ➢ Engineer a method to embed FBG sensors on rotating bending samples,
- ➢ Calibrate the sensor before conducting the test in two ranges (elastic and plastic),

3

- ➢ Measure the strain during the RBT by FBG to get strain versus time and strain versus angle,

- ➢ Employ an elastic-plastic solution to obtain cyclic stress-strain characteristics for AZ31B under RBT,

- ➢ Obtain hysteresis stress-strain of the material under RBT by a combination of the numerical method, VMP, and the experimental results (FBG strain), and

- ➢ Verify the method by comparing the fatigue life estimation and experimental results.

1.3 Thesis Layout

This thesis consists of six chapters. This chapter outlines the motivation of this research and declares the thesis objectives. The chapter 2 presents background information about magnesium and its alloys particularly wrought AZ31B magnesium alloys. Following this chapter, the fatigue behaviour of wrought magnesium alloys is investigated under three cyclic deformation approaches, stress-control, strain-control and load-control. The fatigue behaviour of the material is reviewed based on the literature. Then, the FBG sensor is introduced for measuring the strain. Finally the numerical VMP method is explained for solving the nonlinear plastic and asymmetric problem based on the linear elastic solution. The experimental procedure and modification the rotating bending machine for testing are described in chapter 3. After that, the FBG sensor calibration results are presented to clarify the accuracy of the sensor. The chapter 4 focuses on the procedure of VMP modeling to obtain the cyclic hysteresis of the AZ31B under load-control bending tests. The experimental and modeling results are depicted and discussed in chapter 5. Then to uncover the fatigue behaviour of the material, accurately, the experimental results are incorporated in the obtained modeling. In the last part of chapter 5, the fatigue life of AZ31B is predicted, using the obtained hysteresis and employing the energy-life method. Finally, conclusions and recommendation for future work are summarized in chapter 6.

Chapter 2

Background and Literature Review

This chapter introduces the mechanical properties of magnesium and its alloys, focusing particularly on AZ31B extrusion. It also explains and compares the fatigue behaviour of magnesium alloys under strain-control, stress-control and load-control testing. In addition, the FBG sensor is introduced as a strain gauge, and the advantages of the sensor are explained. Finally, the numerical VMP method employed as part of this study is described.

2.1 Magnesium and Its Alloys

Magnesium, one of the world's lightest known metals, is abundant in seawater and the earth's crust and was first extracted and refined by Sir Humphrey Davy in 1808 [20]. About a century later, this metal was employed in the automotive industry, especially in the manufacture of the Volkswagen beetle [4]. At that time, magnesium was usually preferred for use as an alloying element in aluminum alloys, rather than as a structural material. However, some technical problems, and a demand for higher performance in the automotive industry, led to a decrease in the use of magnesium alloys [21]. Since 1990, the drive to reduce fossil fuel consumption due to its environmental impact has caused renewed interest in employing magnesium and its alloys in the automobile and aerospace industries and for other structural applications [2]. Currently, the use of magnesium alloys, particularly wrought magnesium given its specific characteristics, is expanding rapidly in North America and Europe [6]. The average amount of magnesium and its alloys used per automobile worldwide rose from 3kg in 2005 to 20kg by 2010, and the rising trend is continuing [6].

Magnesium is the lightest commercial metal, with an atomic number of 12, a high strength to weight ratio of around 115, and a density of 1.738 gr/cm^3. Its density is over 75% less than steel, and about 35% lighter than aluminum [3, 5, 21, 22]. Magnesium and its alloys also have good castability, weldabilty, damping capacity, and electrical and thermal conductivity [3, 5]. These properties have persuaded manufacturers to use magnesium and its alloys widely in the transportation industry. However, some of magnesium's shortcomings such as inadequate strength at high temperatures, poor cold workability and weak corrosion resistance have restricted its usage for many applications [2, 21, 23-25]. Moreover, its complicated behaviour such as asymmetric mechanical behaviour under tension

5

and compression, and anisotropic properties related to the direction of a structure, can make analyzing the behaviour of magnesium difficult, especially in wrought magnesium alloys [5, 23, 26]. The mechanical properties of the extruded magnesium alloy AZ31B were obtained by Albinmousa and are listed in Table 2-1 [16].

Table 2-1: Mechanical properties of AZ31B [16]

		Yield strength (MPa)	E (GPa)
Tension	Extrusion direction	213	44
	Transverse direction	56	41
Compression	Extrusion direction	108	44
	Transverse direction	127	46

The crystal structure of magnesium is hexagonal-close-packed (HCP), which leads it to have specific and complicated mechanical properties. HCP metals have two mechanisms for plastic deformation: slip system and twinning. The slip system of HCP crystals has four modes: basal <a>, pyramidal <a>, prismatic <a>, and pyramidal <c+a> [27]. Among them, only dislocation slips in the basal and pyramidal <c+a> planes can be activated in magnesium alloys [28, 29]. The critical resolve shear stresses for pyramidal <a>, and prismatic <a> planes of the slip systems are very high for magnesium alloys. Therefore, the twining mechanism plays a significant role in the deformation of this alloy. While there are two deformation twining systems, tension and contraction, reported for magnesium alloys only tension twinning (known as pyramidal twinning) on the (1012) plane can be activated at room temperatures during loading [30, 31]. The activated tension twining provides strain along the c-axis of the HCP crystal structure. In contrast, contraction twining can only be activated in magnesium when the strain reaches above 8% in uniaxial tests [32]. Figure 2-1 depicts the active slip systems and twin plane of magnesium.
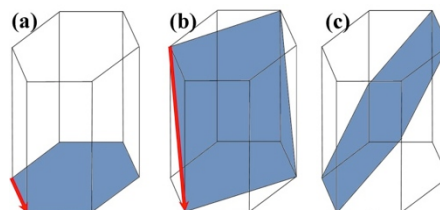
Figure 2-1: Deformation modes in AZ31 extrusion magnesium alloy: a) Basal slip <a>; b) Pyramidal slip <c+a>; c) Tensile twin plane.

Generally, the magnesium alloys are divided into two main groups, casting and wrought [33]. Some of the characteristics of magnesium and its alloys, for example high directional anisotropy in the monotonic tension and compression and strong tension-compression asymmetry behaviour in stress-strain curves, are highlighted in wrought magnesium alloys [34]. They are the result of strong crystallographic texture and the different deformation modes present in HCP crystal structures. Wrought magnesium alloys have poor cold formability in comparison with cast alloys; hence, mass-produced magnesium parts for mobile structure use are generally made from cast [11, 33]. However, wrought magnesium alloys have higher tensile yield strength and manifest properties that are preferable to those of cast ones from a mechanical properties point of view. Wrought magnesium alloys are manufactured by rolling or extrusion, or by a forging process carried out at a temperature above 330°C and followed by slow cooling to prevent crack initiation [35].

Adding various elements to magnesium such as aluminum, zinc, manganese, zirconium and rare earths can improve some of its properties. For example, aluminum is added to magnesium in order to provide solid solution strengthening and to facilitate age hardening [35]. This combination also increases tensile strength and hardness. The addition of small amounts of zinc to magnesium elevates its corrosion resistance [36]. Aluminum and zinc combined with magnesium constitute the AZ group of alloys, which have greater mechanical strength, castability, workability, formability, weldability, and corrosion resistance than pure magnesium. When zinc and zirconium are added to magnesium to produce the ZK group of alloys, the hot workability of magnesium is improved. This enhancement is important to the manufacture of parts by hot working processes such as hot rolling and forging. In AZ alloys, manganese is often added, usually less than 1wt%, to refine the grain size of the alloy [37]. This combination results in better ductility and castability, higher strength, and enhanced energy absorption. A specific weight percentage of aluminum, zinc and manganese, in addition to other elements, added to magnesium create AZ31B, an alloy with properties superior to those of pure magnesium. This alloy has been recognized by the American Society of Testing Materials [38]. Based on the codification, this alloy contains about 3wt% aluminum and 1wt% zinc; the letter B was added to the AZ31 label as it was the second alloy developed under this qualification. The chemical composition of AZ31B is listed in Table 2-2.

7

Table 2-2: Chemical composition of AZ31B extrusion [35, 36]

Composition	Aluminum (Al)	Zinc (Zn)	Manganese (Mn)	Iron (Fe)	Nickel (Ni)	Copper (Cu)	Magnesium (Mg)
Weight %	3.1	1.05	0.54	0.0035	0.0007	0.0008	Bal.

2.2 Fatigue Properties and Analysis

The most common reason for mechanical failure in structural components is fatigue [7]. Structures in the automotive and other industries are subjected frequently to oscillating loads resulting in cyclic stresses. This cyclic stress, over a long period of time, may lead to microscopic physical damage in a material, although the stress is less than tensile or compression yield stress. With an increased number of cycles, the microscopic damage can accumulate and develop into a crack. Strong enough applied stress amplitude in fluctuating loads, and a sufficient number of cycles, can extend the crack and cause the failure of the material. These are the stages of fatigue failure of a material under cyclic loading [18]. Therefore, the importance of accurately evaluating materials from a fatigue point of view and estimating their fatigue lifespan is substantial.

Nowadays, three major approaches are employed to analyze the fatigue behaviour of materials: stress-based, strain-based and fracture mechanics [18]. The latter is not investigated as part of this thesis research. Many studies have investigated the fatigue behaviour of wrought magnesium alloy AZ31B under stress and strain control tests. However, many engineering components are also subject to cyclic bending moments or load-control conditions. Based on the literature, previous load control experiments have been limited to RBT, which provides an S-N curve for high-cycle fatigue regimes; however, identification of the cyclic deformation hysteresis is also required to estimate the fatigue behaviour of materials comprehensively [17, 39-43]. Hence, it is necessary to evaluate the behaviour of wrought magnesium alloys, especially AZ31B extrusion, under RBT in both elastic and plastic regimes. In the following section, stress-control, stain-control and load-control cyclic tests will be discussed briefly.

2.2.1 Stress-Based Fatigue Analysis

Stress-based fatigue analysis was the earliest developed approach to analyzing the fatigue behaviour of materials. In stress-based analysis, a nominal cyclic stress is applied to the material [17], usually in the elastic range, until failure occurs, typically after a high number of cycles [18]. The stress

amplitude is held constant by considering mean stress and stress raising factors. The hysteresis stress-strain curve can be extracted for the various stress amplitudes. In these tests, some plastic deformation can also be observed due to the cyclic stress amplitude. The hysteresis stress-strain curves obtained from these tests reveal some of the fatigue properties of the material.

Servo-hydraulic machine is one of the most commonly used to perform stress-control cyclic tests. This machine applies axial loads, tension and compression alternately to the sample in each cycle to create cyclic loading. The stress applied is held constant in the cross section of the sample during the test. To control the applied stress, the load is actually controlled because the cross section is assumed constant; therefore, there is no practical difference between stress control and load control.

2.2.2 Strain-Based Fatigue Analysis

Another approach to evaluate the fatigue behaviour of a material is strain-based fatigue analysis. Mechanical parts are usually designed to have enough strength against plastic deformation during service. However, some inhomogeneity in the fabricated parts comes from welds and notches, and the stress concentration may induce localized plastic strains [18]. The strain-based fatigue test is a comprehensive test suitable for mechanical parts and structures that experience plastic deformation and have a short fatigue life, however, it is also used for high-cycle fatigue regimes where elastic deformation is dominant. This test is usually performed by servo-hydraulic testing machines that apply axial strain to a gauge section of the sample. The strain is usually measured by an extensometer, which is attached to the uniform gauge length of the sample during the fatigue test. The machine controls the strain amplitude by applying the required stress on the sample. Hence, the magnitude of the stress changes during the test as the number of cycles increases.

Cyclic loading is responsible for the cyclic hardening or softening behaviour of the material. Low-strength ductile metals exhibit cyclic hardening, whereas extensively work-hardened metals tend to experience cyclic softening. These reactions are observed most often at the beginning of loading and gradually stabilize after 10 to 40% of the total fatigue life [17]. The hysteresis loops, stress-strain curves and strain versus life (ε-N) curve, are obtained based on the cyclic behaviour. A cyclic stress-strain curve (CSSC) is usually extracted from the stabilized hysteresis cycles for strain control tests conducted at different strain amplitudes. The curve is plotted from the initial starting point and connects the tips of the stabilized hysteresis loops for the strain amplitudes applied during testing. Since the CSSC determines the resistance of a material against cyclic deformation, it is important and

is reported as a property of material [17].

In the strain control approach, the induced mean stresses can have beneficial or detrimental effects on a material's fatigue life due to the compressive and tensile mean stresses, respectively. The relationship between fatigue life and total strain amplitude (both elastic and plastic strain) is expressed by Morrow's equation. Morrow's model was modified by considering the mean stress for the elastic part as follows:

$$\varepsilon_a = \frac{\Delta\varepsilon}{2} = \frac{(\acute{\sigma}_f - \sigma_m)}{E}(2N_f)^b + \acute{\varepsilon}_f(2N_f)^c \tag{2-1}$$

$$\frac{\Delta\varepsilon}{2} = \frac{\Delta\varepsilon_e}{2} + \frac{\Delta\varepsilon_p}{2} \tag{2-2}$$

Various mean stress correction models, such as Smith-Watson-Topper [44], DIT [8], Lorenzo's [45], and the Coffin-Manson method, have been introduced subsequent to Morrow's model in an attempt to predict fatigue life with more accuracy [18]. Recently, it has been determined that mean stress not only affects the elastic, but also the plastic, portion of the total strain. A modification to the Coffin-Manson model reflects this fact and results in more accurate life predictions [8].

2.2.3 Load–Control: Rotating Bending Fatigue Test

Load control conditions are provided through the RBT. In this test, a uniform bending moment is applied to the sample. Since there is a constant applied load, it is known as a constant load amplitude test. In this test, when the sample experiences elastic deformation during rotational bending, the applied bending moment is translated to a normal stress with the elastic flexural formula, $\sigma = My/I$ [46]. The applied stress increases from zero at the neutral axis (center of the sample), to the maximum absolute value at the surface of the sample. Therefore, the maximum tensile and compressive stresses are located at the bottom and top of the cross section, respectively [17].

RBT is usually employed to find the endurance limits of the material being studied under high-cycle fatigue [18]. However, at higher applied loads, the induced stresses are not uniform within the cross section of the sample, and the elastic flexural formula is no longer applicable for the stress calculation. The fatigue life of materials is usually represented by an S-N curve, noting the number of cycles to failure and stresses applied. It is influenced by stress level, mean stress, residual stress and

10

stress localization, all of which can be affected by holes, fillets, grooves or corrosion. The effect of mean stresses on fatigue life is significant, and is considered as the second most important parameter after stress level [18]. In the high-cycle fatigue regime, tensile mean stresses cause micro cracks and accelerate the rate of crack propagation, while compressive mean stresses retard crack growth. In contrast, the effect of mean stresses is negligible in the low-cycle fatigue region due to the amount of plastic deformation. It has been reported that shear mean stresses have no effect on the crack initiation, although it has some impact on crack propagation [18]. As mentioned in the strain-based approach, the relation between stress amplitude, mean stress and fatigue life can be expressed by various methods and modified to have an adequate estimation of the fatigue life of materials.

In RBT, unlike stress-and strain-control observations, stress-strain hysteresis of materials has not been examined under the load-control test condition. To obtain the hysteresis and predict the fatigue behaviour, the values of stress and strain in the sample during cyclic loading should be measured. However, the evolution of the strain in a material with respect to the number of cycles run during RBT has not been reported yet. This is an aspect of load-control fatigue that warrants further investigation and forms part of the present research.

2.2.4 Fatigue Properties of Wrought Magnesium Alloys

Since the use of wrought magnesium alloys is so prevalent due to their advantages, these alloys have been studied in many research projects [34]. The fatigue behaviour of wrought magnesium alloys under stress-and strain-control conditions has been investigated and fatigue life predicted with a variety of methods [8, 9, 32, 47-55]. In addition, to determine mechanical properties of this material such as strength and ductility, monotonic tension and compression tests have been performed. These tests have been conducted extensively on AZ31B extrusion magnesium alloy [56, 57]. The results showed strong asymmetric stress-strain behaviour of this material due to its strong texture. It was reported that the tensile yield stress of AZ31B is around 213 MPa, and its compressive yield stress ranges between -50 and -108 MPa [16, 56]. When the longitudinal axis of the sample is parallel to the extrusion direction, as is the case in the extrusion direction (ED) samples, the C-axis of all grains is aligned perpendicular to the extrusion direction. When a compressive load is applied parallel to the ED, with the grains in this configuration; the extension twinning system ($(10\bar{1}2)$ -$<10\bar{1}1>$) of HCP crystals has the lowest critical resolved shear stress and hence, will be activated easily [14, 58]. In contrast, when a tensile load is applied to the sample in the same direction, the first deformation mechanism that will be activated is dislocation slip in the basal and non-basal planes [58]. As a result,

the C-axis of the grains will become almost perpendicular to the loading direction. Hence, very high stress is required to reach the yield stress and move the dislocations [59]. This is why the yield stress of extruded magnesium AZ31B alloy is higher under tensile stress than under compressive stress. The compressive yield stress of an extruded sample in which the longitudinal axis is perpendicular to the extrusion direction (transvers direction or TD) should be greater than the tensile yield stress. This statement was supported by experimental results [16].

Another difference between the behaviour of AZ31B magnesium alloy under tension versus compression stress is observed in the strain-hardening rate of the material. Under tension stress, AZ31B shows less work hardening than when under compression stress [16]. This occurs because the number of basal slip systems in HCP crystals is so small and the dislocation multiplication is negligible during tension in comparison with FCC and BCC systems [60-62]. During compression, the deformation mechanisms, twinning and dislocation slipping (basal and non-basal slip), are activated simultaneously and cause considerable strain hardening [14].

Besides asymmetric behaviour, the anisotropic behaviour (directional dependence) of wrought AZ31B has also been verified. Albinmousa [16] performed monotonic tension and compression on samples of AZ31B extrusion in three different orientations: ED, 45°, and TD. He confirmed the sigmoidal behaviour caused by twining, detwinning and slip deformation mechanisms through uniaxial tension and compression tests conducted on ED and TD specimens. Unlike in ED specimens, the tensile yield strength was much lower than the compressive yield for TD specimens. He also reported a linear hardening behaviour in monotonic torsional loading tests and pseudoelasticity in all monotonic tests. Lv et al did a similar test for rolled AZ31B. In this research, the tensile and compressive behaviour of both rolling direction (RD) and transverse to the rolling TD specimens were investigated [63]. These researchers observed that the strength and elongation of the TD specimens under tension and compression were higher than in the RD specimens, and that the compressive yield strength in both directions was much lower than the tensile yield strength due to easier twining deformation under compression. According to Lv et al., the basal planes inclined more in RD than TD specimens due to their basal textures. Also, the Schmidt factor for basal <a> within the grains in TD samples was smaller than in RD samples. In other research, the directional isotropic behaviour of wrought magnesium alloy AZ31B was studied by RBT [39]. Ishihara et al. used a rotating bending machine (RBM) to obtain the fatigue life of the rolled and extruded magnesium in different directions. They found that the fatigue resistance of the extruded samples with ED direction

was higher than those with TD. Also, for rolled magnesium, the fatigue life and fatigue limits of the RD specimens were almost the same as those of the TD specimens, although the fatigue properties of TD samples under high stress amplitudes were more robust than those of the RD specimen. In the SD specimens (another perpendicular direction), the fatigue life was shorter than either the RD or TD specimens at high stress amplitudes. In SD samples, the tensile load was applied perpendicular to the basal plane of the HCP crystal; therefore, the specimens show lower fatigue life in comparison with the other directions. The twin deformations were responsible for this weakness in the material since fatigue cracks preferentially nucleated from these twin locations. The researchers also reported that the fatigue life of extruded magnesium alloy was higher than the rolled alloy because of the higher yield strength of extruded magnesium alloy. The rod-like structure of the extruded material caused a reduction in the rate of fatigue crack propagation and increased the fatigue life [39]. Generally, the microstructure, direction and texture of the sample can change which deformation mechanisms are activated in the material. These important factors impact on the mechanical properties of wrought magnesium alloy. The asymmetric stress-strain behaviour in monotonic tests of wrought magnesium alloys significantly affects their fatigue life and fatigue damage observations.

In the cyclic axial strain-control tests of wrought magnesium alloy, asymmetric cyclic hardening and sigmoidal behaviour in hysteresis loops are observed due to the asymmetry of the mechanical properties in tension and compression. The asymmetric behaviour becomes more recognizable under increasing strain amplitudes, although the asymmetric behaviour reduces as the number of cycles increases [32, 51, 64]. As was the case for monotonic tensile and compressive tests, different deformation mechanisms are responsible for the tensile and compressive reversals. Based on the literature [14, 32, 58, 65, 66], twinning deformation is dominant in compressive reversal, while detwinning deformation begins in the early stages of tensile reversal. When the load is reversed, most of the twinning is substituted by detwinning deformation. A small residual twin accumulates slowly as the number of cycles increases, causing an increase in the critical resolved shear stress. In this case, the twining deformation mechanism can be activated easily in compressive loading, resulting in the hardening behaviour under cyclic loading. As the strain amplitude increases, the cyclic hardening in the compression part becomes more significant than that in the tension part. However, the small grain size and different basal texture can result in a symmetrical hysteresis stress-strain curve under strain-control tests [67]. When this occurs, deformation twins cannot be activated easily during compression, behaviour in contrast to that observed in materials with fibrous texture and large grain

13

size that induce the sigmoid hysteresis loop [68]. In addition, anisotropic stress-strain responses and asymmetric behaviour cause a difference between the magnitudes of the peak and the valley of stresses and also produce the tensile mean stress during strain control testing. The mean stress escalates when the strain amplitudes are more than 0.6% [67].

The fatigue properties of wrought magnesium alloy were also investigated by uniaxial stress-control cyclic tests. Asymmetric hysteresis is observed when the stress amplitude is high enough to induce plastic deformation in the material. Similarly to the abovementioned cases, the plastic deformation mechanisms are different in tension and compression reversals. A large plastic strain is created in compression during the first cycle but is recovered rapidly, and the asymmetric behaviour decreases quickly within the first three cycles [8]. In this situation, the compressive mean strain increases at the beginning of the cycles and then becomes constant as the number of cycles increases [8]. Moreover, the compressive mean strain grows as the stress amplitude increases. Kang et al. studied the uniaxial ratcheting of AZ31B extrusion under stress-control cyclic tests with different mean stresses [56]. According to their reported results, the ratcheting behaviour occurred and the peaks and valleys of the strains alternated with respect to the mean stress. In addition, they observed different ratcheting features when changing the amount of mean stress. Lin et al. reported the same trend for hot-rolled AZ91 magnesium alloys in stress-control conditions [69]. They concluded that as the stress ratio increases, or the peak stress decreases, the fatigue life improved due to the changes in total absorbed strain energy. The plastic strain energy density decreased very quickly during the early cycles based on the cyclic hardening and then remained constant during the cyclic deformation tests. They found that the absorbed plastic strain energy increased as the stress ratio decreased and the peak stress rose. Therefore, high stress ratios and low peak stresses reduce the total strain energy absorbed and can improve the fatigue life of AZ91 magnesium alloy.

Shiozawa et al. evaluated the fatigue behaviour of three extruded AZ31, AZ61 and AZ80 magnesium alloys under strain- and stress-control conditions [64]. They observed the tensile mean stress under strain-control, and compressive mean strain under stress-control, conditions for selected magnesium alloys. They claimed that the effect of the tensile mean stress was stronger than the effect of the compressive mean strain on the fatigue resistance, because the induced value of the tensile mean stress was greater than the compressive mean strain during different conditions. In addition, they determined the fatigue behaviour in low-cycle regimes for the three extruded magnesium alloys was material dependent under strain-control tests, however, in stress-control tests, the behaviour was

material independent and could be estimated with the plastic strain range accurately.

Most research into the fatigue life and fatigue properties of wrought magnesium alloys has studied the material under strain-and stress-control cyclic tests conducted with a push-pull and RBM. The effects of texture and microstructure of a material play an important role in improving its mechanical properties and consequently fatigue life and fatigue properties. Moreover, some factors, which alter the total absorbed strain energy, can affect the fatigue life of the material. The higher elongation in strain-control tests and the higher tensile yield strength in stress-control tests are responsible for increasing the fatigue life. For example, for rolled AZ31, the low-cycle fatigue life of TD samples was higher than for RD samples in both stress- and strain-control cyclic tests [52, 67].

2.2.5 Comparison between Strain-and Stress-Control

Since the stress and strain responses of asymmetric wrought AZ31B are different under cyclic stress- and strain-control, it is clear that the stabilized hysteresis curves should be dissimilar. In strain-control tests, the stabilized hysteresis curves remain sigmoidal and asymmetric, whereas the stabilized hysteresis curves become symmetric in stress control tests. One of the significant differences between stress- and strain-control tests for this alloy is the compressive mean strain and tensile mean stress induced during each test. The ratcheting behaviour is observed in stress-control tests due to the compressive mean strain. Comparisons between stress- and strain-control become critical when obtaining the CSSC of the extruded magnesium alloy is essential. The CSSC can reveal characteristics of the materials under cyclic loading that are different from the behaviour of the material under uniaxial loading. To compare the CSSC of the AZ31B extrusion under cyclic stress- and strain-control tests, the stabilized hysteresis curves of the CSSC in both conditions, reported by three independent research publications, were considered.

Hassegawa et al. conducted cyclic tests of extruded magnesium alloy AZ31 for four different strain amplitudes and five stress amplitudes under strain- and stress-control conditions, respectively [8]. They extracted the plastic strain amplitude and mean strain versus life for the stress- and strain-control tests separately. On the other hand, Huppmann et al. conducted this series of tests with counter pressure for conventional AZ31extrusion [32]. They reported the maximum stresses versus life of the material for different strain amplitudes under strain-control. They also calculated the mean strains and strain amplitudes versus life, individually, under stress-control conditions. In the current thesis research, to obtain peak and valley stresses in order to generate the CSSC, simple calculations

were done.

The data obtained from these calculations and the CSSC from the research done by Albinmousa are summarized in Figure 2-2 [16]. As mentioned in Section 2.2.4, the hysteresis curves under stress-control exhibit ratcheting behaviour due to compressive mean strains. To investigate this further, it was necessary to eliminate the ratcheting by subtracting compressive mean strains from the hysteresis obtained under stress-control conditions. Figure 2-2 demonstrates that the CSSC trend under both conditions is similar, although it is impossible to ignore the considerable deviation that exists between them.

This comparison was necessary because in the present research, the CSSC of AZ31B extrusion generated by Albinmousa [16], was employed to model the fatigue behaviour of the material under load-control bending tests by using the numerical method. It was assumed that the CSSC is a material characteristic and is independent of the cyclic loading condition (stress-control, strain-control or load-control).
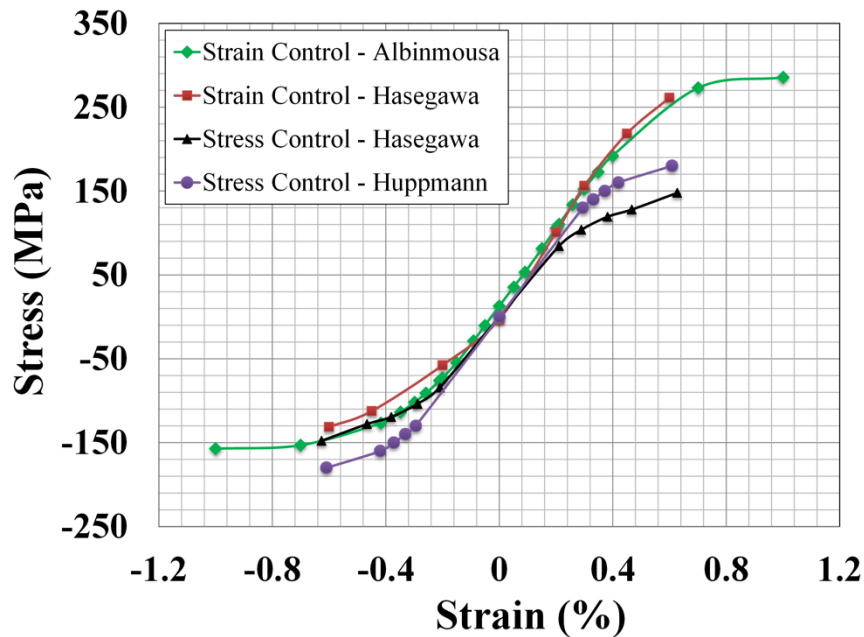
Figure 2-2: Comparison between CSSC in stress- and strain-control tests, adapted from [8, 16, 32]

2.3 Fiber Bragg Grating Sensors

FBG sensors have been widely used in the telecommunication industry and are also used in optical multiplexers, demultiplexers, laser stabilization, and notch filters [70, 71]. Their most important attribute from the point of view of this research is their ability to identify or monitor physical quantities. The FBG has been employed as a sensor to detect a variety of quantities such as strain, temperature, pressure, and vibration [72].

2.3.1 History

In 1978, Ken Hill demonstrated that the refraction index changes in germanium doped fibers and observed photosensitivity in these fibers [73]. When a wave of argon laser light is propagated along the fiber core, permanent gratings are formed. A narrow wavelength band peak can be reflected based on this specific grating. In 1989, Gerald Meltz used the interference pattern of ultraviolet light technique to create the periodical structures inscribed (Bragg grating) in the FBG core [74]. In 1995, the first commercial FBG sensors became available [75].

2.3.2 Structure and Theory

A fiber optic is usually a hair-thin filament of fused silica (SiO_2) and consists of two parts, a core and cladding. The core is a very small inner part, with a diameter of 4 to 9 μm, and the cladding is an outer part of 125 μm in diameter. To increase the mechanical stability and to prevent crack growth in the glass fiber, it is coated with acrylate, polyimide, or organic modulated ceramic [75] . Figure 2-3a shows the layers of an FBG as a schematic, and Figure 2-3b shows a real FBG sensor.
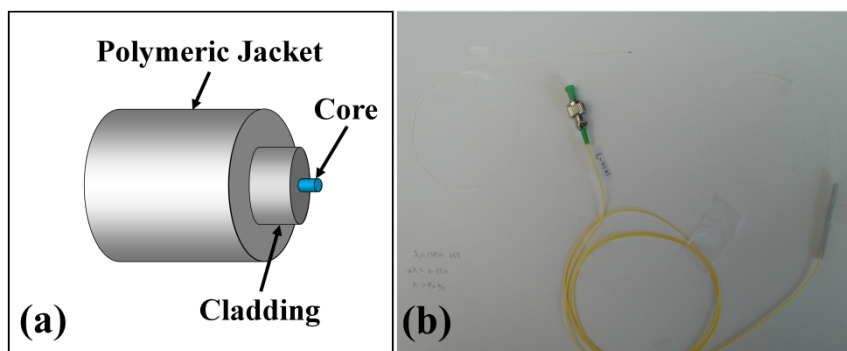
Figure 2-3: (a) FBG schematic, (b) FBG sensor

Usually light travels inside the core, because the refractive index of the core is higher than the cladding. This index difference is normally produced by doping the core with germanium. The refractive index of the core can then be changed by ultraviolet light because the germanium doping is photosensitive. A higher level of germanium doping causes a higher refractive index in the core. The Bragg grating can be written into the germanium doped core by an intense ultraviolet light to create the FBG. Writing Bragg grating into the fiber core generates a set of high intensity and narrow wavelength band peaks. The inscribed section is coated with polyimide again after the manufacturer removes the original coating to write the Bragg grating [71, 72].

The difference between the refractive index of the grating plane and that of the core, can affect the reflected light, which is propagated along the core of the fiber. The reflection of the light becomes weaker based on the Fresnel effect [72]. On the other hand, each grating plane can reflect a very small part of the incoming light depending on the level of germanium doping (and consequently the refractive index of the core). When the phase shifts of reflected light from each grating plane differ, destructive interference occurs, although equal phase shifts can accumulate and create a strong reflection peak. By considering the summation of the reflection from each grating plane, the whole grating reflection is obtained. According to Bragg's law, which is the fundamental assumption behind the FBG sensor's operation, λ_B is the reflected wavelength or the Bragg wavelength, which is defined by Equation (2-3)

$$\lambda_B = 2n_{eff}\Lambda_G \tag{2-3}$$

Hence, the reflected wavelength is a function of the effective refractive index of the grating in the core of the FBG (n_{eff}), and the periodicity of the grating (Λ_G). The wavelength inside the fiber is shorter than the wavelength in a vacuum, and the effective refractive index is expressed by comparing the speeds of light traveling inside the fiber and the vacuum. When the wavelength of the incoming light is precisely the same as the Bragg wavelength (λ_B), and all of the grating plane reflections are in phase, the level of energy increases and a sharp peak is created [75].

On the other hand, the grating length and strength can affect the properties of FBG. The bandwidth of the reflection peak can vary due to the grating length. However, with the strong grating limit used for special types of FBG, the bandwidth depends only on the grating strength. Moreover, the reflectivity of the peak depends on both the grating length and strength. In addition, the ultraviolet light dose, the level of germanium doping, and hydrogenation procedure utilized can also affect the reflectivity.

18

Usually, the bandwidth of the reflection peak is defined by Full-Width-Half-Maximum (FWHM), which is the width of 50% of the main peak. Generally, the FWHM, the Bragg wavelength (λ_B), and the reflectivity are used to specify the properties of the FBG being used [72, 76].

2.3.3 Grating Structure

The periodicity of the optical fiber grating and/or the refractive index can affect the structure of the FBG. Four states of grating period (uniform, chirped, tilted and superstructure), and two characteristics of the refractive index (profile and offset), can change the structure of the grating [77]. Usually the refractive index profile is uniform or apodized, and the offset is positive or zero. Figure 2-4 shows the different types of common grating structures.

When the FBG sensor has uniform grating, the Bragg reflection main peak is surrounded by a series of side-lobes, which can make it difficult to identify the main peak. To reduce this problem and suppress the side-lobes, the apodization technique is employed during the FBG fabrication. The structure of the grating in this configuration is graded, and the refractive index tends to be zero at the end of the grating. Therefore, a narrow bandwidth of the FBG reflection main peak is created. To apodize the FBG, two functions (Gaussian and raised-cosine) are used [76]. For the experiments conducted as part of this thesis research, the grating structure of the FBG under test was apodized.
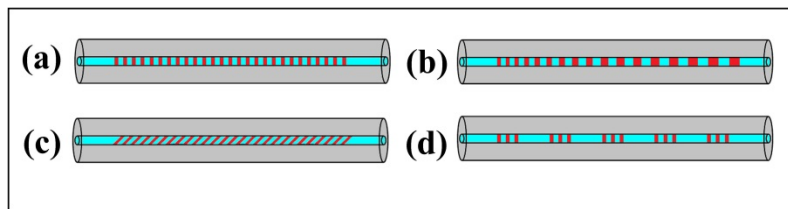
Figure 2-4: Schematic diagram of different types of grating: (a) uniform FBG; (b) chirped FBG; (c) tilted FBG; (d) superstructure FBG, adapted from [78]

2.3.4 Fiber Bragg Grating Sensor

FBG are employed as sensors to measure physical quantities such as strain and temperature due to their fundamental nature and structure [79]. According to Equation (2-3), the Bragg wavelength (λ_B) is a function of the periodicity of grating (Λ), and the effective refractive index (n_{eff}). It is clear that

any external factor that changes one of those parameters can displace the FBG reflection main peak and consequently the Bragg wavelength (λ_B). When a lateral force is applied to the FBG, the length of the grating increases or decreases with respect to the external force as a result the periodicity of the grating (Λ) changes. Moreover, the effective refractive index may be changed by the photo-elastic effect. In addition, with a temperature variation, which can cause thermal dilation or contraction, the length of the grating also changes. This can also impact the effective refractive index through thermo-optic effects. Hence, a Bragg wavelength that shifts via the external force and temperature can identify the mechanical strain and temperature changes of a material sample when the FBG is attached as a sensor. The relation between the wavelength shifts, strain, and temperature changes is specified according to the following equations:

$$\frac{\Delta\lambda}{\lambda_0} = k\times\varepsilon + \alpha_\delta\times\Delta T \tag{2-4}$$

$$\varepsilon = \varepsilon_m + \varepsilon_T \tag{2-5}$$

$$\alpha_\delta = \frac{\delta n/n}{\delta T} \tag{2-6}$$

where, $\Delta\lambda$ is the wavelength shift, λ_0 is the base wavelength at test start, k is the gauge factor, ε is the total strain caused by force (ε_m) and temperature (ε_T), α_δ is defined by the change of the refractive index, and ΔT is the temperature change (K). It is important to mention that the magnitude of the gauge factor can be varied via the core diameter changes and doping concentrations, although these variations make only 1.5 % of difference in the photo-elastic coefficient, p, where k is equal to 1-p [80].

When the FBG sensor is attached to the sample, the strain caused by temperature changes is calculated by the following equation:

$$\varepsilon_T = \alpha_{sp}\times\Delta T \tag{2-7}$$

In this equation, α_{sp} is the expansion coefficient of the sample (1/K). Therefore, the mechanical strain is obtained by inserting Equations (2-5, 2-6 & 2-7) into Equation (2-4)

$$\varepsilon_m = \frac{1}{k} \times \frac{\Delta\lambda}{\lambda_0} - (\alpha_{sp} + \frac{\alpha_\delta}{k}) \times \Delta T \tag{2-8}$$

When the temperature is constant during the experimental procedure, the mechanical strain is calculated simply by the first term of the Equation (2-8). However, if the strain of the sample is zero, the external force does not exist and so the FBG sensor acts as temperature compensation sensor. Therefore, the temperature change can be obtained by

$$\Delta T = \frac{1}{k \times \alpha_{sp} + \alpha_\delta} \times \frac{\Delta\lambda}{\lambda_0} \tag{2-9}$$

On the other hand, when the mechanical strain is zero, and the FBG is not fixed on the sample the FBG sensor detects the temperature changes according to the following equation:

$$\Delta T = \frac{1}{k \times \alpha_{glass} + \alpha_\delta} \times \frac{\Delta\lambda}{\lambda_0} \tag{2-10}$$

In this case, α is the expansion coefficient of the fiber (SiO_2) and not of the sample. The value of α_{glass} is almost zero; hence, the most important factor in this situation is related to refractive index changes (α_δ) [75].

Frequently, FBG sensor are not only used as sensors to measure strain and temperature, but also for measuring many other physical quantities such as pressure, vibration and displacement which cause disturbances on the grating of the FBG when properly designed [72]. Furthermore, an FBG sensor can be employed for multiple purposes in wide dynamic and temperature ranges as well as for strain/deformation and temperature measurement in different applications and situations. Various mechanical packages have been introduced to provide good conditions for the sensors, which may have to stay in place for a long time in harsh environments. Montero et al. determined the effects of humidity and adhesive type on results extracted by FBG sensors [81]. For example, they observed up to a 65% variation in data results due to a long stay at high humidity. Therefore, the FBG must be isolated through proper packaging design. The protection used by Montero et al. was M-COAT-B, with M-COAT-A and PU 140. They also calculated the strain in fatigue testing for aged F114 steel samples by using infrared thermography techniques. After employing the selected protection package, the average of error was reduced significantly. Maron and Kersey also designed a package, consisting of three-purpose function FBG sensors to be used for measuring temperature, pressure and vibration

in harsh environments [82]. They used a capillary tube made of a material with high strength and corrosion resistance to isolate the FBG sensors and protect them from humidity and high temperature [83]. These researchers confirmed the FBG sensors' capacity to measure the deformation of materials and temperature changes under challenging conditions.

Other researchers have employed FBG sensors to monitor the fatigue crack growth rate during fatigue testing. Two FBG sensors were mounted in front of the crack tip and inside the hole of a CT specimen with a superficial groove and small feed-through hole [84]. In this research, Brotzu et al. traced the fatigue crack growth on the surface and in the hole of the specimen. They also demonstrated the capability of the sensor to specify the differences between exterior and interior strains [84].

In other research, a Flat-Cladding FBG sensor was used to characterize the fatigue behaviour of AZ31B extrusion magnesium alloy during strain-control cyclic tests [85]. Gu et al. mounted the three Flat-Cladding FBG sensors and an extensometer on a sample and observed the behaviour of this material under a variety of strain amplitudes ranging from ± 0.1% to ± 0.6%. They reported that the asymmetric behaviour of this alloy was enhanced, and that cyclic hardening occurred, with increased strain amplitude. They claimed that the obtained results were in good agreement with those from the extensometer. Feng et al. also used a Flat-Cladding FBG sensor and extensometer simultaneously, to obtain the hysteresis of an aluminum alloy under a large strain amplitude of ± 0.8% cyclic test [86]. They reported that the measured strains were compatible with those obtained from the extensometer during the strain control cyclic test. These two studies verified the reliability of FBG sensors in low- and high-cycle fatigue testing. Overall, there is evidence that the sensors are effective in many applications for precisely detecting various physical quantities in different environments, although factors such as the type of adhesive used and the embedding method employed should be considered, as for any other sensors, to obtain the best results.

2.3.5 Advantages of Fiber Bragg Grating Sensors

Nowadays, the most prevalent technologies used to measure strain are electrical foil gauge, electrical vibrating wire, and FBG sensors. However, the FBG sensor provides superior advantages and higher performance than the other technologies. Because FBG sensors use light instead of electrical conductors, they are immune to electromagnetic interference and high voltage [72]. An FBG sensor is electrically passive and nonconductive and therefore can be used under harsh conditions, such as

lightening and high voltage [71]. It can be exposed to various temperatures, such as in cryogenic environments, due to its low thermal conductivity and it is possible to change the chemical composition and create special versions of FBG sensors for use in elevated temperatures of up to 1000°C [83, 87]. These sensors have good metallic corrosion resistance and high long-term durability [84]. Therefore, they are suitable for use in harsh environments [83]. In addition, measurement of different physical quantities such as strain, temperature and pressure can be done by connecting several FBG sensors together in a linear series without adding complexity to the measuring system [81].

One of the most beneficial features of FBG sensors, which make them ideal for use in this thesis research, is their ability to measure high strain better than conventional thin film strain gauges. Moreover, these gauges cannot be used with the hourglass sample RBMs due to the size and shape of the sample and the operation of the machine. Extensometers, which are able to measure large strain amplitudes, have similar installation problems. On the other hand, both conventional thin film and extensometer sensors are capable of measuring the strain for a large area, unlike the FBG sensor, which measures the strain locally [85]. Therefore, the FBG sensor can be used for welded, dissimilar-material and particularly for samples undergoing RBT where the maximum changes of strain occur in the minimum cross section [88]. FBG sensors can be easily installed on the curvature of the sample and passed through the bearing housing because of their very small size. As a result, such sensors have become the new alternative and competitive candidate for measuring material strain during RBT.

However, FBG sensors have some disadvantages, which need to be taken into consideration for this thesis research. The FBG sensor is sensitive to temperature changes; for each 1°C increase in temperature the ratio of the wavelength change compared to the initial wavelength is equivalent to 0.0008% mechanical strain [75]. Moreover, the distance between the sensor and the curvature surface can cause calibration errors. Hence, it is important to be aware of temperature changes and calibration error during strain measurement.

2.4 Variable Material Property Method

The VMP method is a numerical method that can be employed for solving nonlinear elastoplastic problems by using a simple linear elastic approach [19, 89]. In the elastic solution adapted for this method by this author, stress is a linear function of strain so that Young's modulus as a field variable

must be updated during an iterative solution. Young's modulus is degraded by increasing the number of iterations until the results converge to the nonlinear elasto-plastic reference property of a material. Therefore, this method can be proposed for asymmetric and isotropic problems with nonlinear plastic behaviour, thus avoiding more complicated conventional analytical solutions. This method simulates the behaviour of the material under uniaxial and cyclic loading, and can also provide the hysteresis curve of the material obtained under cyclic loading [90].

2.4.1 Loading

The behaviour of materials under applied loading is a function of each material's unique properties. After deriving the constitutive equation of the material, the material properties must be specified. The Young's modulus (E) is an important property of a material is updated to an effective Young's modulus (E_{eff}) during the iterations. To implement this approach, the material section under applied loading should be discretized into finite elements. Then, the elastic solution is applied for each element individually, based on the actual stress-strain curves of the material. Therefore, the first iteration for each element will lie on a line with a slope of the obtained E from the real stress-strain curve. To find E_{eff} for subsequent iterations, a projection method is employed, as long as the applied stress is higher than the yield strength. Based on this method, point a obtained during the first iteration has the same strain as point $á$ on the actual stress-strain curve (see Figure 2-5). Hence, the stress value of the point, $\sigma_{á}$, can easily be obtained from the real curve.
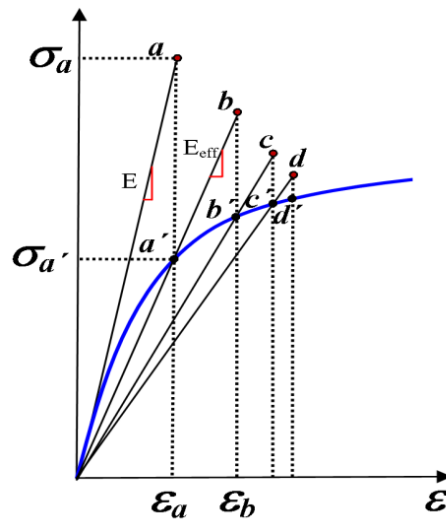

Figure 2-5: Projection method

24

The first updated value of E_{eff} is calculated by taking the ratio of the stress and strain at the corresponding point of the real stress-strain curve by the following equation:

$$E_{eff} = \frac{\sigma_{\acute{a}}}{\varepsilon_a}$$

(2-11)

This value is less than that of the E of the material and is used to obtain the strain at point b using theory of composite beam, and consequently the equivalent stress at point $\acute{b}$. The goal is to eventually find the final updated E_{eff}, which is always less than that of the previous iteration. This procedure continues for each element until convergence occurs and point a finds the real stress value, and lies on the actual stress-strain curve. It is clear that the final effective modulus, and consequently the deformation of each element are different in nonlinear materials.

2.4.2 Unloading

During unloading, materials behave differently, especially when the hardening occurs under plastic deformation. The unloading behaviour of materials usually depends on the hardening rules such as kinematic and isotropic; however, not every material responds in the same way to those rules. The VMP simulation for unloading is similar to the loading model, meaning that the elastic solution is employed and the projection method is used to find the stress and strain of the material. It is important to mention that the location of the ending point, which is obtained from the loading curve for each element, is considered as a starting point for the unloading. Moreover, the negative value of the loading is applied to the starting point to provide the unloading solution. Unlike during loading, each element has its own unloading curve, which depend on the hardening rule. However, for materials with complicated behaviour, the real stress-strain unloading curve is utilized instead of the standard hardening rule. Hence, the elasto-plastic stress response of the element after loading and unloading can be calculated by VMP simulation and extended to all elements. The proposed model also is practicable for reloading and, therefore, can be employed to extract the cyclic hysteresis behaviour of the material through a consecutive process: loading, unloading, and reloading. Hence, the VMP approach is a reliable method that can be applied to nonlinear, anisotropic and asymmetric materials, to find realistic elasto-plastic solutions and stress responses of the materials under loading and unloading.

Jahed and Dubey established this method and employed it to solve an inelastic problem, involving a thick-walled cylinder made of Tresca materials that was under internal pressure [19]. They confirmed

25

the ability of the VMP method to analyze nonlinear behaviour by using a simple linear solution, and verified its compatibility with analytical solutions. This method was also used by Kalatehmollaei et al. to investigate the behaviour of asymmetric AZ31B extrusion under load-control conditions [90]. They could observe the changes of the neutral axis while the sample experienced plastic deformation during the RBT. They also reported the calculated residual stresses after unloading by using this method. In addition, the fatigue life was predicted, based on the energy method, and the results compared with experimentally collected data. They demonstrated that the model results were in good agreement with many experimental results.

2.5 Life Prediction Approach

Since fatigue life prediction is essential for engineering design, finding a reliable method is indispensable. Various approaches have been proposed to predict the fatigue life in low- and high-cycle fatigue regimes [8, 48, 91-93]. These methods have been modified with considering mean stress to achieve more precise prediction. Three fatigue parameters; strain amplitude, stress amplitude and total strain energy density are considered to predict the fatigue life of a material. However, stress and strain amplitude parameters cannot be developed for anisotropic and asymmetric materials, such as AZ31B. In addition, the Coffin-Manson model cannot provide a reasonable life prediction for this type of material. According to Park et al., the stress and strain parameters of rolled AZ31B were unstable during the fatigue life, although another fatigue damage parameter (total strain energy density) was constant up to $\frac{N}{N_f} \approx 0.9$ [94] They concluded that the fatigue life prediction of wrought magnesium alloy would be more reliable based on the total strain energy density. Albinmousa et al. performed fatigue life prediction for AZ31B extrusion, using a strain- and energy-based model proposed by Jahed and Varvani [16, 95]. They showed that predictions made with the energy-based method were more precise than those made with the other method. Based on the Jahed-Varvani model the total strain energy density is calculated by

$$\Delta w_T = \Delta w_P + \Delta w_{e+} \tag{2-12}$$

$$\Delta w_P = \int_{-\varepsilon_1}^{+\varepsilon_2} \sigma d\varepsilon \tag{2-13}$$

26

$$\Delta w_{e^+} = \frac{\sigma_{max}^2}{2E} \qquad (2\text{-}14)$$

where, Δw_P is the plastic strain energy density, which is the energy required for plastic deformation in a material. This value is calculated by obtaining the area inside the hysteresis stress-strain curve of each cycle. The second term of Equation (2-12) is introduced as a positive elastic energy density, which is determined based on the maximum stress. Figure 2-6 shows a schematic hysteresis and specifies the plastic and elastic strain energy density of a cycle. The total strain energy is associated with the number of cycles to failure, N_f. Inputting the calculated total strain energy from Equation (2-12) to Equation (2-15), the fatigue life is accurately estimated by

$$\Delta w_T = w_f (N_f)^c + E_f (N_f)^b \qquad (2\text{-}15)$$

w_f, E_f, c, and b refer to the material characteristics, which are constant coefficients for any given material [47, 96].
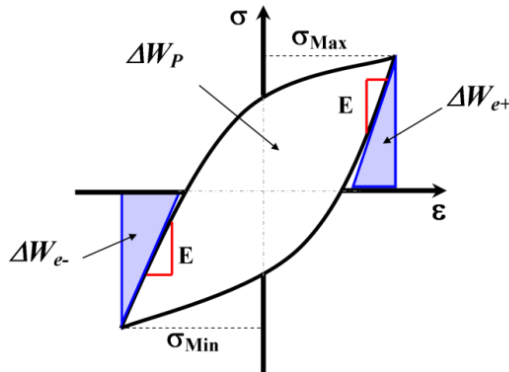
Figure 2-6: Illustration of plastic and elastic energy

Chapter 3

Experimental Procedure

3.1 Material Characterization

In this study, the material under investigation was wrought magnesium alloy, specifically AZ31B extrusion. It was extruded in a temperature range between 360°C and 382°C, at an extrusion exit speed of 50.8 mm/s with an extrusion ratio of 6, and was then air quenched [16].

3.1.1 Sample Preparation and Dimensions

To conduct the fatigue experiments, hourglass samples that conformed to the rotating bending machine were cut from the extruded section of AZ31B. The thickness of the sample sections was 15 mm. The position of the samples and their longitudinal direction are shown in Figure 3-1. The specimens were finely polished to minimize surface roughness effects. To relieve the stress from the as-received AZ31B material, the ASM-recommended stress relief process was carried out on the specimens [97]. To eliminate the influence of residual stress during RBT, a heat treatment was applied to evaluate the fatigue strength without any residual stress. The heat treatment process was conducted at a temperature of under 260°C (500°F) for 15 minutes, followed by air-cooling.
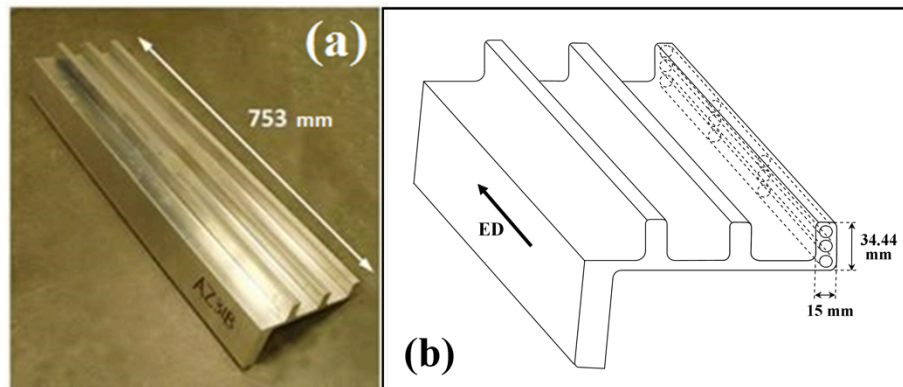
Figure 3-1: a) Extruded sample b) Schematic of the extruded section, geometry and the position of samples

The shape and dimensions of the specimens used for the RBT are shown in Figure 3-2. The length of

28

the specimens was 70 mm and the diameter of their necks was 7 mm. Figure 3-3 depicts the rotating bending sample.
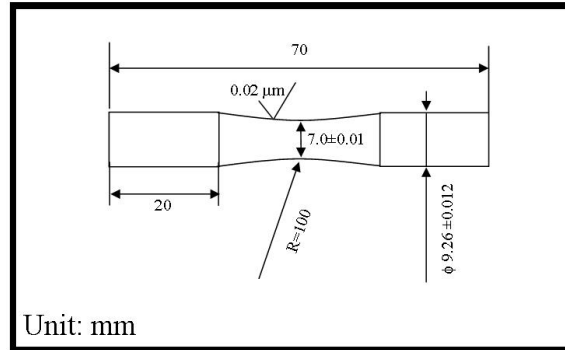
Figure 3-2: Shape and dimension of the AZ31B extrusion specimens

Figure 3-3: Rotating bending sample

3.2 Experimental Methodology

3.2.1 Rotating Bending Machine (RBM)

RBT is usually employed to help determine the material fatigue life. For this purpose, a straight shank or tapered-end sample is rotated at an adjustable speed of between 500 to 10,000 RPM by an RBM (see Figure 3-4). A constant load is applied to the sample during the rotation, and a digital counter records the number of rotations or cycles. In this machine, the force of the rotation is generated by an electrical motor and is then transmitted to the sample through two bearing housings. The straight shank sample is gripped by collets, which are set in the spindle parts of the bearing housings. A constant load is applied to the end of the bearing housings, creating a constant and uniform, pure bending moment in the cross section of the sample. This uniform bending moment provides flexural stresses on both sides of the neutral axis of the sample. Therefore, during each rotation, the sample experiences maximum compressive stress in the top side of the cross section and

maximum tensile stress on the bottom side, intermittently. In other words, each hypothetical point of the sample surface is alternately subjected to loading, unloading, and reloading, in each complete revolution.

Figure 3-4: R. R. Moore Rotating Bending Machine [98]

To investigate the fatigue behaviour of a material and obtain the S-N curve, different loads are applied to the samples and the number of cycles recorded until the specimens fail or reach a certain number of cycles. Using the RBM, the following equation can be employed to calculate the stress applied to the sample in the elastic region:

$$S = \frac{16WL}{\pi D^3} \qquad\qquad (3\text{-}1)$$

where, S is the extreme stress (MPa); W is the total load applied to the specimen (kg); L is the moment arm (mm), which is the distance from the end support to the load point; and D is the minimum diameter of the specimen (mm). To save calculation time, a table (Appendix 1) has been prepared by the manufacturer of the machine (R. R. Moore Company), and lists a loading factor for each specified minimum diameter of the specimen. The stress is calculated by dividing the total load into the loading factor of the specimen from the table [98]. However, as previously mentioned, the stress under load control bending tests in the plastic regime needs a new method of calculation. This is the subject of this research, which is explained in the next chapter.

This research moves one step beyond the traditional fatigue RBT by adding an FBG sensor to measure the strain experienced by a sample undergoing the test. The RBM was modified by installing

a stepper motor in parallel to the main motor to reduce the rotation of the machine (Figure 3-5). A gear was installed on the main shaft of the RBM's drive, and the stepper motor was coupled to the main motor by a plastic belt through this gear. This modification was required as the data logging system of the FBG sensor (interrogator) is able to record only two data per second (2 Hz), whereas the minimum speed of the electrical motor is 500 RPM (8 Hz).
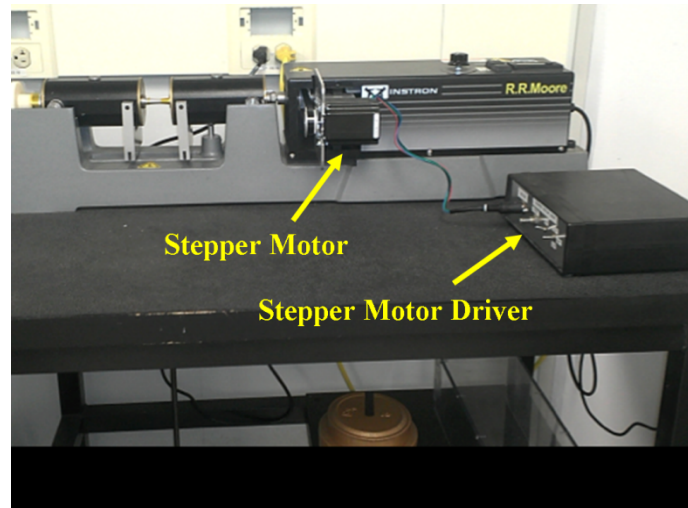
Figure 3-5: Modified Rotating Bending Machine.

3.2.2 Fiber Bragg Grating (FBG) Sensor

In this research, Corning SMF-28 optical fiber with an effective length of 5 mm (where the Bragg grating is written), a diameter of 125 μm and an initial wavelength of approximately 1550 nm was used. The Bragg grating had been written on a single mode of the optical fiber and the modulation of the grating was Gaussian-apodized. A fiber connector FC/APC, which connected the FBG to the interrogator, was attached to one side of the fiber optic cable. The optical interrogator used was a Micron Optic sm125-200 with 5 pm resolution. It had an accuracy specification of 10 pm [71, 99].

3.2.3 Sensor Mounting

In this study, two adhesives were utilized to mount the FBG sensor on the sample. In this section, these adhesives are introduced, and their curing process discussed. Moreover, the calibration of the sensors is outlined.

3.2.3.1 Bonding Method and Epoxy Selection

In the traditional strain measuring method, which uses a foil strain gauge technology, the embedding and gluing procedures, temperature, and humidity can be considered as the main sources of error for strain measurement [75]. These aspects are also the most important issues for the new generation of strain acquisition sensors, including the FBG sensor. Therefore, the choice of appropriate adhesive, bonding method, and approach to protect the sensor from the environment have to be considered carefully. In order to reduce measurement errors, all of the tests were done in an almost identical environmental situation, and the mounting and gluing were conducted under a microscope to adjust the sensor position, prevent slippage of the FBG sensor, and ensure uniformity of the gluing. In this research, two different types of epoxy were chosen, EPO-TEK 353ND and Norland optical adhesive 61.

3.2.3.2 Thermal Epoxy

The high temperature EPO-TEK 353ND adhesive is composed of a two-component epoxy resin that cures in three steps. The temperature and duration of these steps were 80°C/30min, followed by 120°C/30min and 150°C/30min, respectively [99]. This procedure results in a stiffer bond between the glass and metal when compared to the usual recommended curing process, which has one step curing at 150°C/60min [100]. This epoxy has high viscosity, 3000-5000 cps at 23°C [100]. This feature leads to reduce liquid epoxy flow, when it is employed on a curvature surface.

To obtain more-accurate results, the polyimide coating of the FBG sensor was removed. The FBG sensor was placed on a microscope plate and its polyimide coating was scraped off by using a cotton swab smeared with furniture stripper. When the coating was completely removed, the exposed FBG sensor and RBT sample were cleaned with isopropanol. Then, the center of the Bragg grating of the uncoated sensor was placed and fixed on the center of the sample, which had the smallest diameter. Red and blue markings signified 20 mm distance from the center of the Bragg grating. These marks made it possible to locate the grating of the sensor, and adjust its position on the sample, as otherwise the grating part was not visible.

To use the 353ND adhesive, the specified amounts of the thermal epoxy components were mixed, a small amount of the mixed epoxy was applied to the sample with a needle, and then it was cured by a heat gun. The curing process creates a non-negligible compressive residual strain on the sample near the surface. For accurate sensor calibration, the strain on the sample after curing was measured. It was

found to be -0.16%, and this value was added to the strains obtained by the FBG sensor. This compressive strain is clearly evident in the compressive stress found on the surface layer of the sample. This residual stress is generated by the difference between the coefficients of the thermal expansion of the metal and the cured epoxy.

3.2.3.3 Optical Epoxy

Another type of epoxy used for this project was Norland optical adhesive 61. This epoxy resin cures when exposed to ultraviolet light. The curing procedure for this epoxy does not require much time and depends on the thickness of the epoxy layer and the intensity of the ultraviolet light used. This adhesive makes an excellent bond with metal and optical fiber. For perfect curing, the maximum absorption of ultraviolet light should be within the range of 320-380 nm with an energy of 3J/sq.cm [101]. To conduct tests using this epoxy, the adhesion process was done precisely, under a microscope, to prevent the formation of bubbles between the epoxy and the specimen. After cleaning the sample with isopropanol and removing the polyimide coating from the FBG sensor as before, the middle part of the grating fiber optic was accurately mounted on the middle of the specimen. Then a small amount of the epoxy was put on the FBG sensor with a needle and cured by ultraviolet light.

During the curing process, the temperature of the sample rose due to the application of ultraviolet light and the exothermic reaction created by the curing of the epoxy. This heat can influence the structure of the metal; hence, the temperature of the sample was measured during curing. This was done by a thermocouple connected to the sample in the same way as the FBG had been (Figure 3-6). Figure 3-7a shows the temperature changes of the sample recorded by the thermocouple. This experiment revealed that the temperature rose from ambient room temperature to a maximum of 87°C and reached equilibrium at this temperature.

Moreover, the FBG sensor's output was recorded during curing to investigate the effect of the curing process on the sample. This observation demonstrated that curing induced a 0.06% compressive strain to the sample (Figure 3-7b). The induced compressive strain is translated into 25 MPa residual stress in the sample. It was clear that the strain resulting from the Norland epoxy was much less than that induced by the 353ND adhesive.
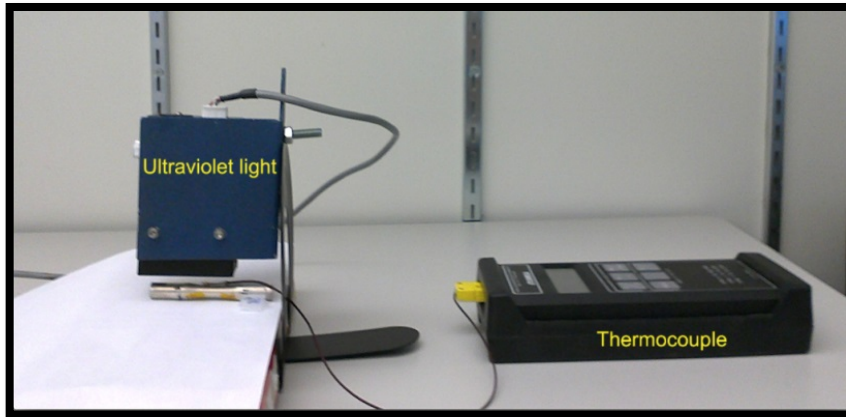
Figure 3-6: Thermocouple setup
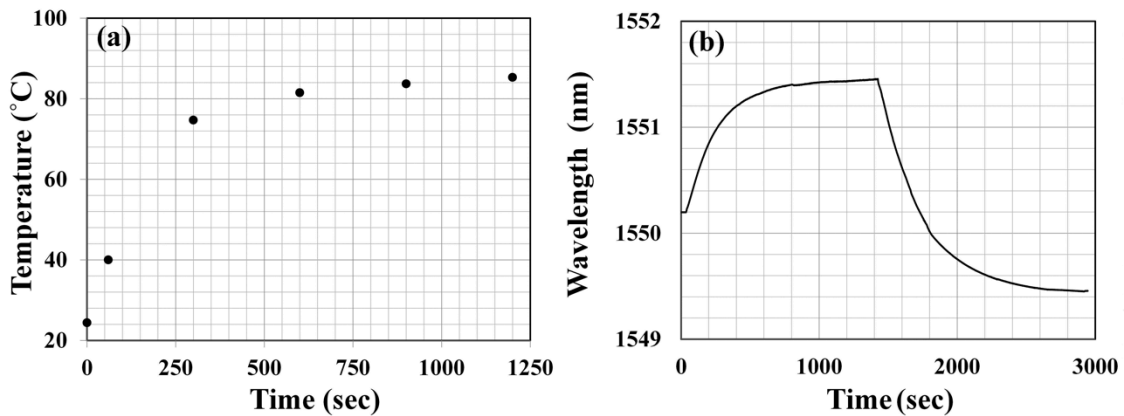
Figure 3-7: (a) Temperature change observed during curing; (b) Wavelength changes recorded during the curing process and cool down to primary temperature.

3.2.4 Sensor Calibration

To demonstrate the accuracy of the strain measured by the FBG sensor, a digitally controlled servo-hydraulic Instron testing machine was employed. In these experiments, an extensometer with a gauge length of 8 mm and an FBG sensor were simultaneously utilized to record the deformation of the samples. Figure 3-8a shows the setup of the experiment. A close up image of the sample and sensors is presented in Figure 3-8b.
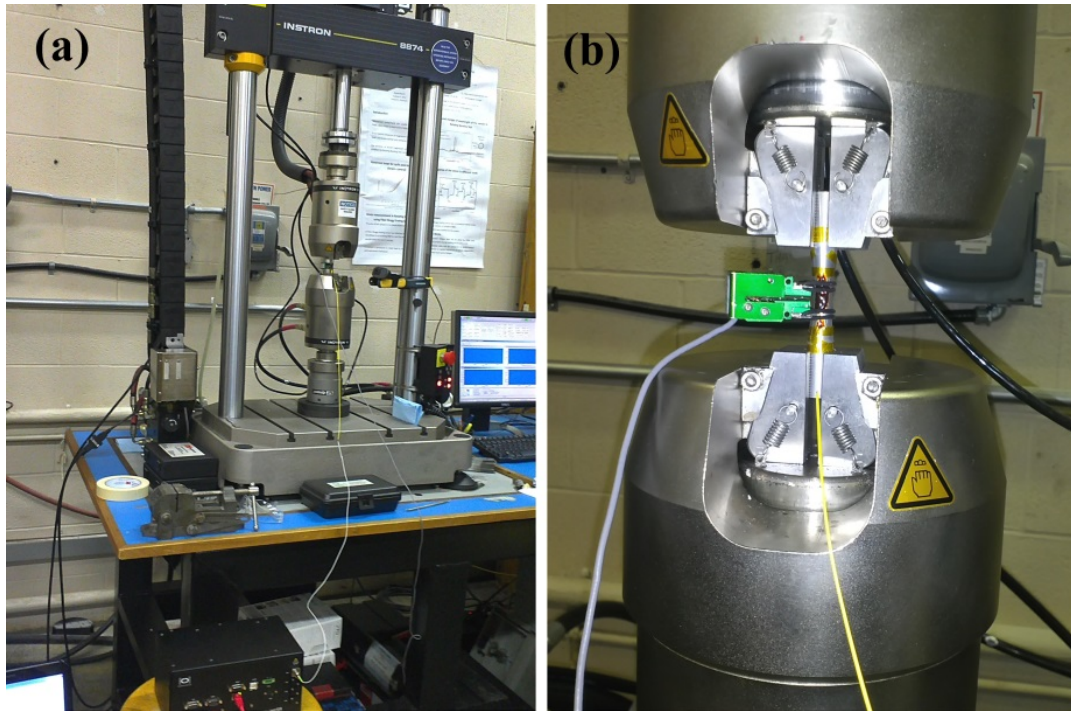
Figure 3-8: Sensor calibration setup (a) the Instron machine and the interrogator, (b) FBG sensor and extensometer mounted on the sample.

These tests were performed using both adhesives, thermal and optical epoxy, and the results are presented and compared below.

First, the thermal epoxy was selected and the FBG sensor adhered to the sample as outlined above. Figure 3-9 shows the results of a test done under stress-controlled cyclic conditions with an absolute value of stress of 50 MPa. This test was repeated for different loads. Figure 3-10 depicts the hysteresis loops for the stress controlled cyclic test with the stress amplitude about 110 MPa. This stress amplitude created a high level of strain in the first stress control cycle test to ascertain the capacity of the FBG sensor to measure strain in the higher range, and to test the stiffness of the thermal epoxy to hold the FBG sensor on the specimen. Based on the extracted results, the measured strains via the FBG sensor were in good agreement with those obtained from the extensometer, except for the maximum tension, which showed a small deviation (Figure 3-9).
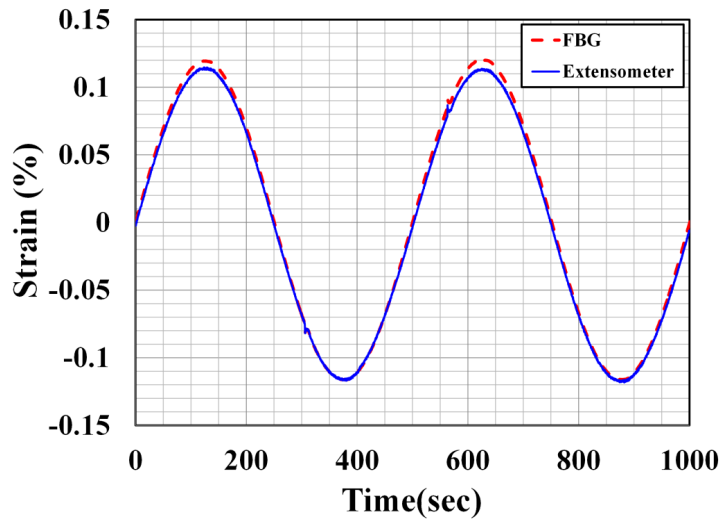
Figure 3-9: Comparison between strain recorded by extensometer and FBG sensor in stress control cyclic test, $\sigma_a = \pm 50MPa$
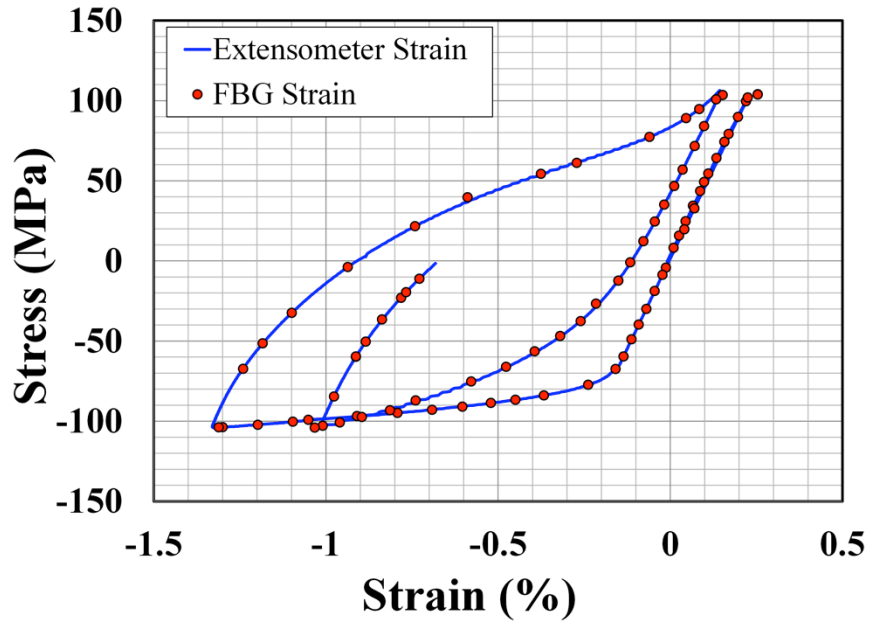
Figure 3-10: Stress-strain response for a sample of AZ31B extrusion; the strain was measured by FBG sensor and extensometer at the stress amplitude of ±110 MPa

Second, the optical adhesive was employed to adhere the FBG sensor to the specimen. Figure 3-11 depicts the strains measured by the FBG sensor and extensometer during cyclic loading with stress

amplitude of ±70 MPa. Additionally, compression testing with a stress of -60 MPa, and tension testing with a stress of about 52 MPa, were carried out. The strain results from both measurement devices are compared in Figure 3-12a and b, respectively. The results clarified that the strains obtained from the FBG sensor are completely compatible with the extensometer results.
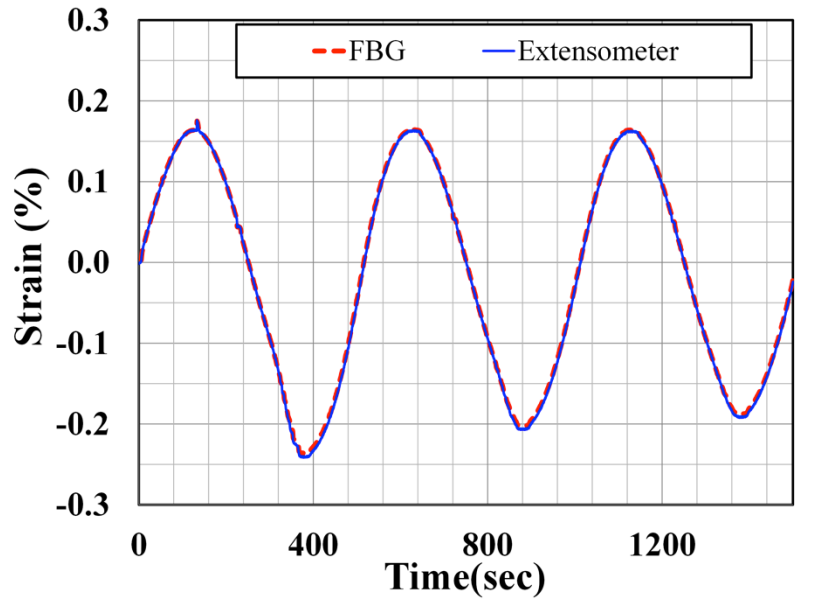
Figure 3-11: Stress control cyclic test, $\sigma_a = \pm 70 MPa$
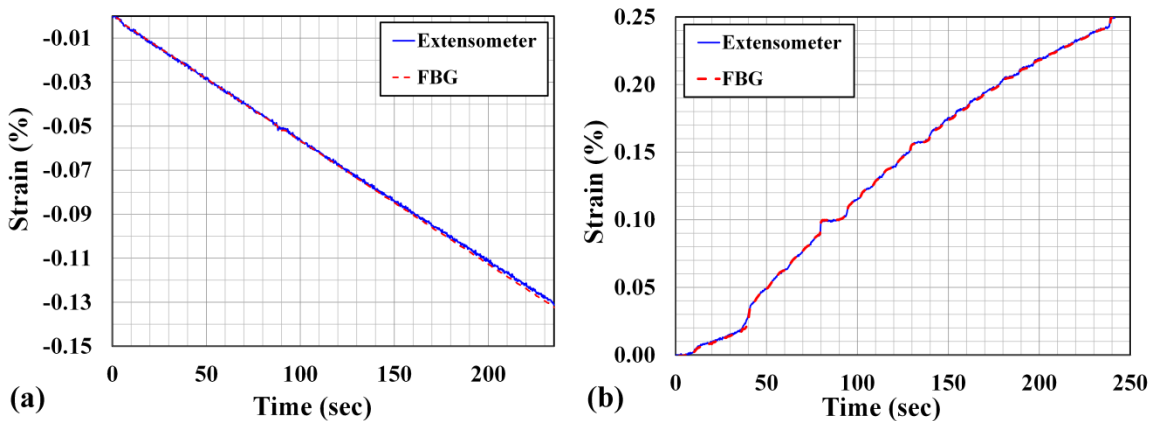
Figure 3-12: (a) Compression test, $\sigma = -60 MPa$, (b) Tension test, $\sigma = +52 MPa$

Based on the results, it is clear that both the thermal and optical adhesives make a stiff bond between silica glass and AZ31 magnesium alloy. It is important to mention that in spite of thermal epoxy

37

creating a stiffer bond (useful for higher strain amplitudes), the optical epoxy was utilized during RBT due to its curing procedure. As mentioned, thermal epoxy generated a relatively high compressive residual strain during the curing procedure, which translated into a 69 MPa compressive residual stress that is critical in RBT, although monotonic and uniaxial cyclic tests are not sensitive to surface residual stress. In addition, the accuracy of the strains measured by the FBG sensor when glued with optical epoxy was very good and was considered sufficient for the RBT designed to be used in this research. Therefore, Norland Optical Adhesive 61 was selected for use in all of the experiments conducted as part of this research.

3.2.5 Rotating Bending Test

To make an appropriate setup for installing a specimen equipped with the FBG sensor, it was necessary to design a spool to hold the extra filament of the sensor while the specimen rotated. The spool rotates with the rotation of the sample and prevents rupture of the sensor. This spool was designed by 3D-CAD design SOLIDWORKS software and printed by 3D printing (Figure 3-13). It is worth noting, that this spool reduces the applied moment on the sample by only 0.5%. This small change can be ignored in the total moment calculation. Another modification of the machine was a 3 mm diameter hole drilled in the middle of a solid drawbar of RBM to pass the FBG sensor. This drawbar, accompanied by a second bar, was inserted into the spindle of the bearing housings to grip the specimen by the collets, tightly.
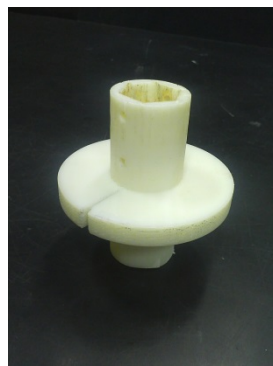
Figure 3-13: 3D printed spool

During installation, an FBG sensor was passed through the embedded hole of the spool, the groove of the drawbar, and the middle of the collet, in series, while the drawbar and the collet were in the

bearing housing. Figure 3-14 shows the assembled system before the FBG sensor was fixed on the specimen.
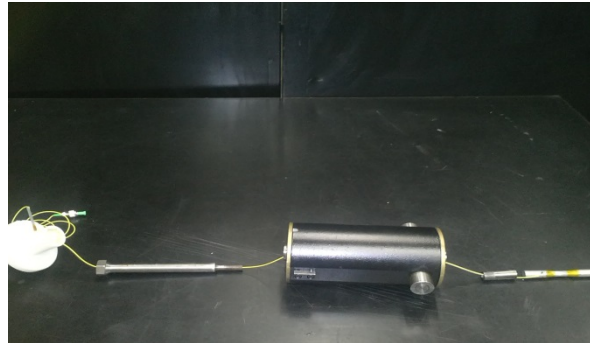
Figure 3-14: Assembled setup before mounting the FBG sensor on the specimen

Next, the FBG sensor was mounted on the sample with Norland Optical Adhesive 61, following the gluing procedure mentioned in Section 3.2.3.3. Then, the assembled setup was installed in the RBM. The FBG sensor was connected to the interrogator while measuring the strain, during which time the stepper motor adjusted the rotating speed of the machine to the rate of the interrogator (0.001 Hz). When the FBG sensor was not measuring the strain, it was disconnected from the interrogator and the main drive of the RBM was employed to rotate the sample at a speed of 20 Hz. The RBT were performed for several different loads and the strains were collected for different cycles.

3.3 Summary

In this chapter, the shape and dimensions of the RBT samples were specified. In addition, the geometry and position of the RBT samples in the original AZ31B extrusion section were clarified. The RBM was introduced, and the modifications made to the machine in order to reduce the speed of rotation were explained. After that, the specifications and curing procedure of two types of adhesive used for adhering the FBG sensors were articulated. The accuracy and precision of the sensors' strain measurements in both elastic and plastic regimes were illustrated. Temperature changes of the sample during curing of the optical epoxy were reported, and the induced residual stress in the RBT sample resulting from the curing process for two types of epoxy was measured and compared. At the end of this chapter, the installation procedure for the RBT sample equipped with the FBG sensor in the RBM was explained.

Chapter 4
Modeling

In high cycle fatigue, the stress on a sample during the RBT can be calculated by the elastic flexural formula. However, the stress response of the sample, particularly in case of asymmetric materials such as AZ31B extrusion that experience plastic deformation, cannot be calculated easily. Therefore, an elastic-plastic simulation method is proposed to find the stress response of the material under RBT, which is associated with the strain measured by an FBG sensor, to generate cyclic hysteresis in load-control tests. The details of this model are discussed in this chapter.

4.1 Elastic-Plastic Analysis of AZ31B Extrusion

AZ31B extrusion exhibits asymmetry in yield and directional anisotropic behaviour. In the following analysis, only the asymmetry is considered; the material is assumed to behave isotropically otherwise. In the pure bending case of RBT, the stress state is one-dimensional. The normal bending stress alternates between maximum tensile and maximum compressive stress in each cycle. Therefore, the nature of the dominant stress is associated with the asymmetric properties of AZ31B, and is accounted for in this analysis.

When a cylindrical AZ31B extrusion sample is subjected to a constant load applied in the form of four point bending moments (Figure 4-1), the induced stresses due to the applied moment are distributed throughout the cross section of the sample. During the rotation of the sample, each point of the surface experiences a different value of stress from the maximum in the lower part (tensile stress), to the minimum value in the upper part (compressive stress) of the cross section. Figure 4-2a is a schematic of the stress distribution applied to the sample of AZ31B, which demonstrates that the applied stress was less than the tensile and compressive yield strength of the sample (in the elastic regime). This figure depicts how a linear distribution specifies the stress response to the applied elastic loading. However, when the sample was plastically deformed, the stress distribution was nonlinear and asymmetric (see Figure 4-2b). The maximum and minimum stress levels, as well as the amount of plastic deformation in the tension and compression parts, were completely different under the two scenarios. In addition, the neutral axis was displaced due to the asymmetric behaviour of AZ31B extrusion.
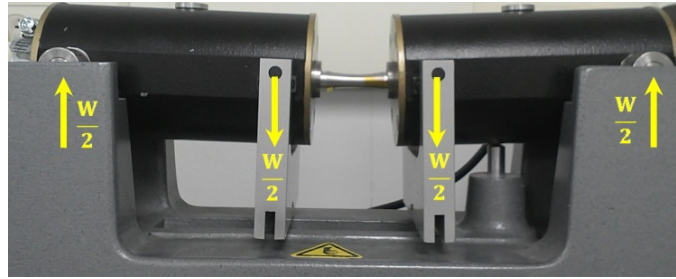
Figure 4-1: Loading of the sample in RBT
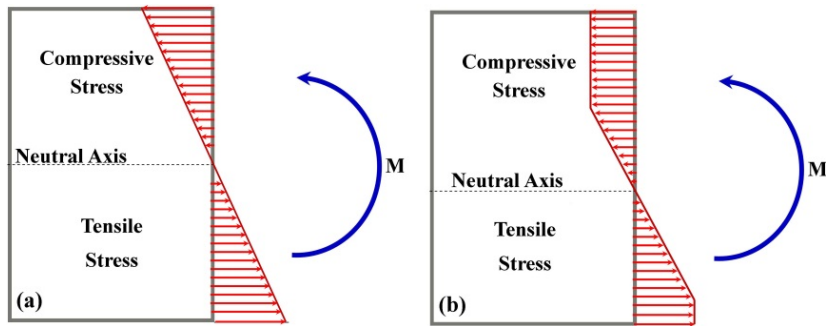
Figure 4-2: Schematic of the stress distribution in a cross section of AZ31B; a) elastic deformation; b) elasto-plastic deformation.

To simulate RBT using the proposed elasto-plastic method, it was assumed that fluctuating loading was being applied to a stationary sample in the form of four point bending moments (referred to as the alternative approach), as opposed to conventional RBT where the load is kept constant and the sample is rotating. Hassan et al. compared the conventional RBT with a fixed beam that was under alternative loading by experiment and finite element simulation [102]. Based on their simulation results, the stress ranges for both approaches (alternative and conventional), are very close and the stress distribution (stress gradient) of the cross section in both tests is the same. They also compared the modeled stress results with experimental results and claimed that they were in good agreement. However, the strain range in the conventional RBT was higher than that the strain in the alternative test and the fatigue strength of the conventional approach was lower than that of the alternative test, especially in the low-cycle regime [103, 104]. This is understandable given the nature of these two tests. When the sample is fixed, the maximum compressive and tensile stresses are applied to the top and bottom of the sample, respectively. Therefore, the failure of the sample can occur at either of these points. In conventional RBT, the sample rotates and every point on the sample's surface

experiences the maximum and minimum value of the stress at 270° (maximum tension) and 90° (maximum compression) in each revolution. In this scenario, a crack can form at the weakest point of the surface; hence, failure usually occurs after fewer cycles. Therefore, while the alternative test can be used in the proposed elasto-plastic analysis method to find a reliable stress response for the sample, the modeled strain response is less accurate and should be substituted by experimental results.

In this research, the alternative method was used to simulate the RBT, and the elastic-plastic behaviour of the AZ31B extrusion was analyzed based on the proposed VMP method [90]. For this purpose, a cross section of the sample was divided into a finite number of elements and the elastic-plastic solution was performed for each element separately. Figure 4-3 depicts the discretizing of the cross sections and identifies the location of the elastic neutral axis.
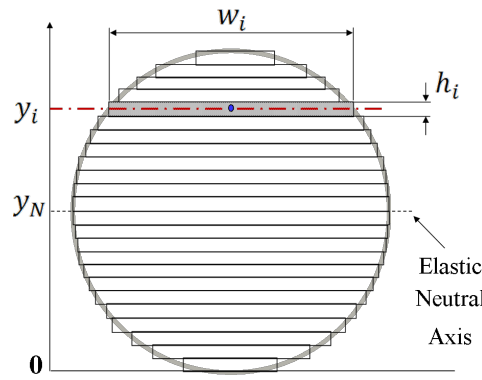
Figure 4-3: Discretizing the cross section into finite elements

The position of each element, y_i was identified by the location of its center and calculated by the Equation (4-1) in which, h_i is the height of the element and i is the element's number. The width of the element, w_i, was obtained with respect to the minimum radius of the sample and the position of the element by Equation (4-2).

$$y_i = (i \times h_i) - \frac{h_i}{2} \tag{4-1}$$

$$w_i = 2 \times \sqrt{(r^2 - (y_i - r)^2)} \tag{4-2}$$

Then, the elastic solution was obtained for all elements by employing the elastic flexural formula to calculate the stress and strain for the first iteration. In the following equations, σ_i is the stress of the element, M refers to the applied moment, and I is the moment inertia of the element.

$$\sigma_i = \frac{M(y(i) - r)}{I} \qquad (4\text{-}3)$$

$$\varepsilon_i = \frac{\sigma_i}{E} \qquad (4\text{-}4)$$

4.2 Loading

The stress and strain of the elements under different ranges of the applied loading were obtained based on the CSSC and VMP methods. To perform the VMP, it was necessary to have the material's properties in the form of the stress-strain and unloading curves at different plastic strains. The CSSC was generated from the stabilized hysteresis strain control tests for different strain amplitudes, and the monotonic tension and compression of the sample material were used as the references curve in this model. Figure 4-4 illustrates the stabilized hysteresis of the cyclic axial strain control tests for seven different strain amplitudes. The experimental results were obtained from as-received AZ31B extrusion tubular samples by Albinmousa [16]. The CSSC and the monotonic tension and compression of this material are exhibited in Figure 4-5. It is important to note that when obtaining the stress and strain responses of the first cycle in the RBT, the monotonic tension and compression were used as a reference curve.
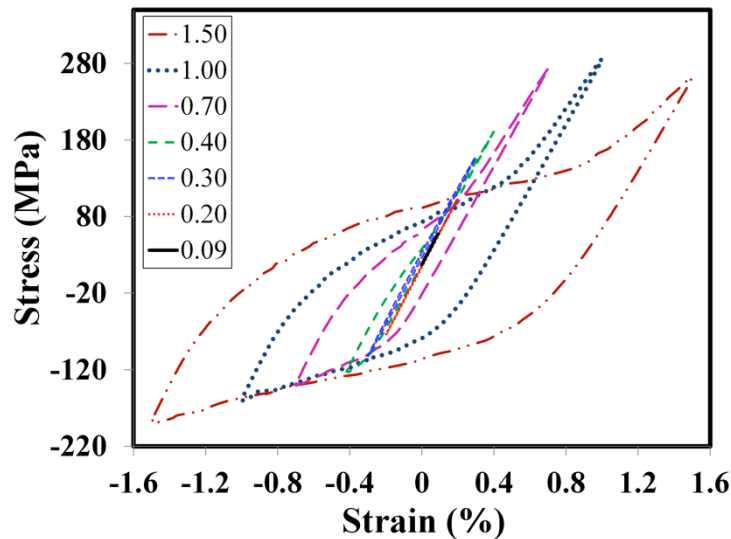
Figure 4-4: Stabilized cyclic hysteresis of AZ31B extrusion (strain-control) [16]
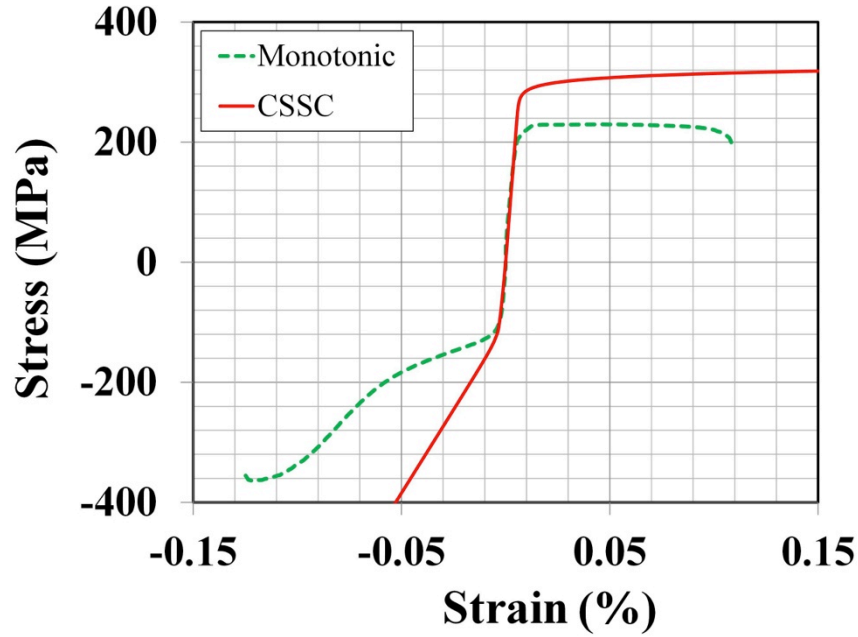
Figure 4-5: Cyclic stress-strain curve (CSSC) and monotonic tension/compression of AZ31B extrusion [16]

Utilizing the VMP and projection methods, explained in Section 2.4.1, E_{eff} for each element was updated after conducting the first iteration. Since the values of the effective Young's modulus for the elements were different, each element was treated separately by using its material properties. Hence, the beam was considered to be a composite made of a finite number of materials. Based on the theory of composite beams, the modification coefficient n was defined by the ratio of the effective elastic modulus of each element to the Young's modulus of AZ31B.

$$n = \frac{E_{eff}}{E} \tag{4-5}$$

Based on the obtained ratio n, the width and area of the element were modified to calculate the position of the neutral axis and second area moment of inertia of the section as follows:

$$w_{new} = n \times w_0 \tag{4-6}$$

Due to the change in the size of the elements, the position of the neutral axis shifted due to the asymmetric behaviour of AZ31B and was calculated by:

44

$$C = \frac{\sum A_i(y_i - r)}{\sum A_i} \tag{4-7}$$

where A_i is the area of the element and C is the position of the neutral axis. The elements' new moments of inertia were calculated based on the new position of the neutral axis and the modified width of the elements. The elastic solution was repeated for the second iteration, and according to the updated E_{eff}. Then, the new stresses and strains of each element were calculated by solving Equations (4-8) and (4-9).

$$\sigma_{new} = \frac{nM(y_i - C)}{I} \tag{4-8}$$

$$\varepsilon_{new} = \frac{\sigma_{new}}{E_{eff}} \tag{4-9}$$

At the end of the second iteration, the width of the elements returned to their initial values. The new properties obtained for each element were used for the next iteration and the VMP iterations were continued until the obtained stress and strain curve matched the reference stress-strain curve. Figure 4-6 shows the results for the bottom element under a bending moment of 10 Nm. After nine iterations the stress and strain values converged to the CSSC of the material. The convergence criterion for VMP iterations was the total difference between the elements' stress for two consecutive iterations.

$$\frac{1}{N} \times \sum_{i=1}^{N} \sqrt{\left(\sigma_{i,j} - \sigma_{i,j-1}\right)^2} < 10^{-5} \tag{4-10}$$

where N is the number of elements and j is the iteration's number. In the loading part of the VMP model, the monotonic curve was also used for obtaining the first cycle results and the corresponding curves were utilized for obtaining the remainder of the cycles following the same steps.
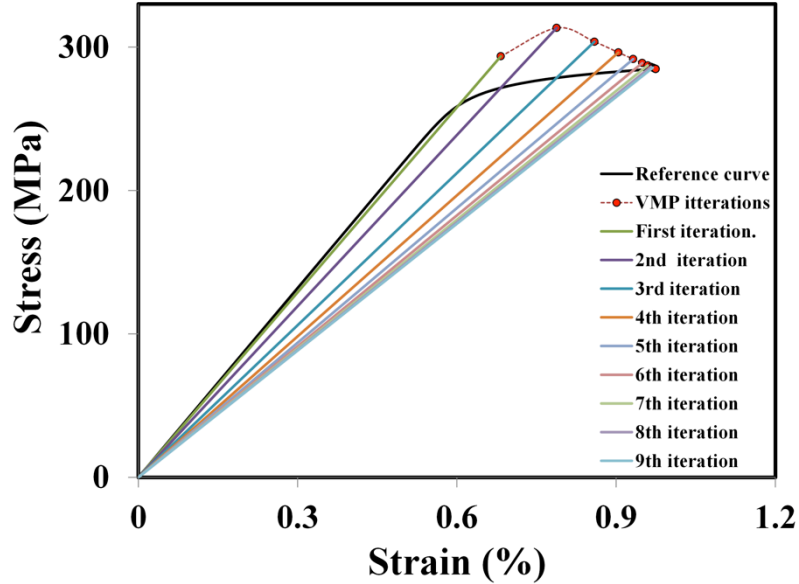
Figure 4-6: Applying projection method for loading: results are shown for the bottom element with maximum tension, (M=10 Nm)

4.3 Unloading and Reloading

At the end of the loading, each element had an individual stress and strain; therefore, the starting point for each element for conducting unloading was different and each element had its own unloading curve. As previously mentioned, the unloading of wrought magnesium alloys cannot be predicted according to kinematic and isotropic hardening rules. Hence, to analyze the unloading behaviour in the AZ31B sample, the reference curves were extracted from actual stabilized hysteresis strain-control tests in the various strain amplitudes. To obtain the reference curves for the elements, the unloading and reloading reversals of hysteresis were employed, which are schematically demonstrated in Figure 4-7. The unloading reversal, which is the downward side of the hysteresis loop, was transferred to build the unloading curve; and the reloading reversal, which is the upward side of the hysteresis loop, was transferred to build the reloading reference curve.

The measured unloading-reloading curves are shown for a wide range of over-strains in Figure 4-8 [16]. To find the corresponding unloading and reloading curves, the element's strain value at the end of loading was selected as a point on the transferred unloading/reloading curve (ε_P in Figure 4-9) and the stress of this point, σ_P, was found from the CSSC. When the strain of the element at the end of loading was positive, the lower part of Figure 4-8 (unloading parts) was employed, whereas for a

negative element strain at the end of loading, the upper part (reloading curves) was used as an input for the simulation.
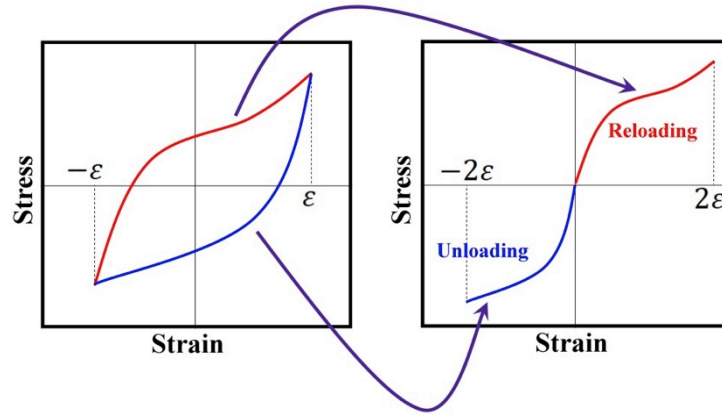
Figure 4-7: Schematic representation of the unloading and reloading curves obtained from hysteresis
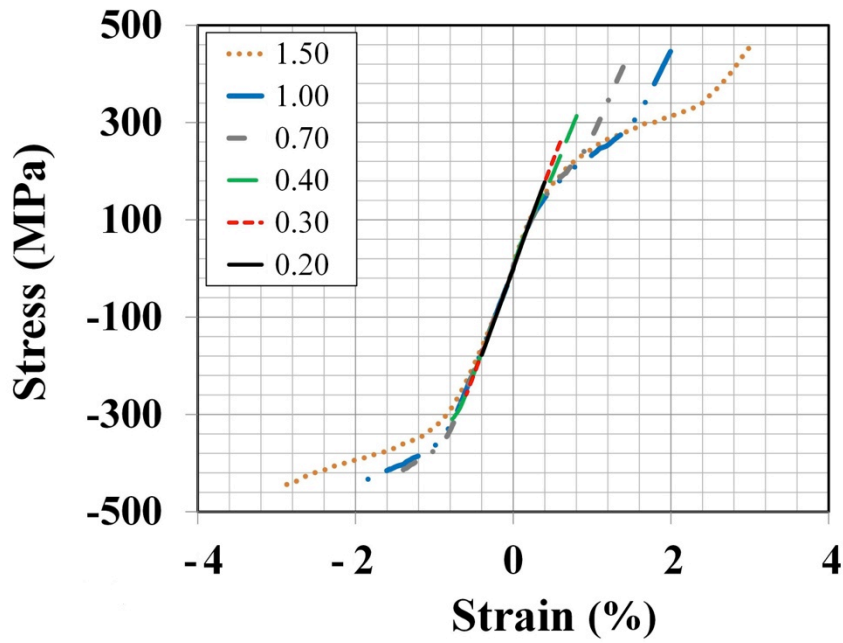
Figure 4-8: Unloading-reloading reference curves over a wide range of over-strains

If the strain at the end of loading fell in between the two curves of Figure 4-8, the unloading/reloading curve was calculated by a linear interpolation between the experimental reference curves as shown schematically in Figure 4-9. Curve A and B are assumed to be the reloading curves obtained

47

experimentally. To obtain the reloading curve between curve A and B that passes through the point P, it was necessary to find the strains of points on the curve based on the specified stresses. The corresponding strain for any stress, such as σ_X, was calculated by interpolation between the curves A and B by Equation (4-11). The same approach was taken for strains outside of the range shown in Figure 4-8 using linear extrapolation.

$$\varepsilon_X = (\varepsilon_T - \varepsilon_S) \times \frac{(\varepsilon_P - \varepsilon_M)}{(\varepsilon_N - \varepsilon_M)} + \varepsilon_S \qquad (4\text{-}11)$$
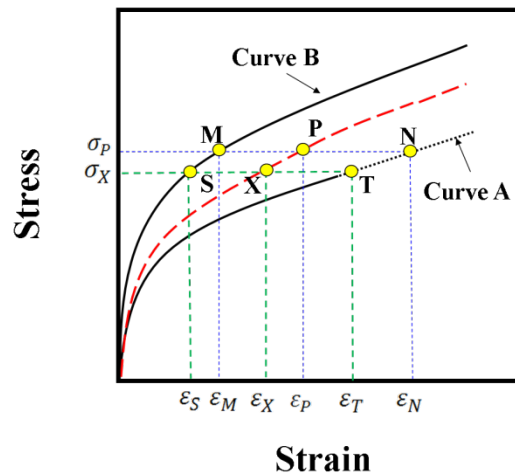
Figure 4-9: Schematic representation of the linear interpolation performed between two experimental hysteresis curves to find a curve corresponding to the strain in between

4.4 Cyclic Hysteresis

In this simulation, the cyclic hysteresis was obtained for each element of the cross section, individually. This was done by finding the stress and strain value for each element under the applied moment, (M), and applying two times the initial bending moment (-2M, minus sign signifies reverse loading) to the element. Then, the response to stress and resultant strain under unloading and reloading reversals were calculated by the VMP method following the same procedure as for the loading; however, in this case each element followed its own unloading/reloading material curve. This method was repeated to find the stress and strain under unloading and reloading curve by changing -2M to 2M to obtain a full cyclic hysteresis. The model was run for all elements separately

48

to obtain the loading, unloading and reloading reversals. Therefore, by using this method the hysteresis curves of the elements during a full cycle could be calculated. Since the top and bottom elements play critical roles in the RBT, the cyclic hysteresis curves of these elements were obtained in this research.

4.5 Combining Strain Measurements

For the experimental part of this project, the strain on the surface element was measured with an FBG sensor embedded on the sample during the RBT. To illustrate, the position of the FBG sensor relative to the RBT sample, the cross section of the sample and the surface element is schematically presented in Figure 4-10. The surface element's deformation was precisely measured, and the real trend of the strain during RBT was captured. As discussed above, the stress-strain hysteresis of all of the elements could be calculated by the VMP simulation. Therefore, by replacing the measured strain data with the corresponding strain calculated from the VMP, new hysteresis curves for RBT were obtained.
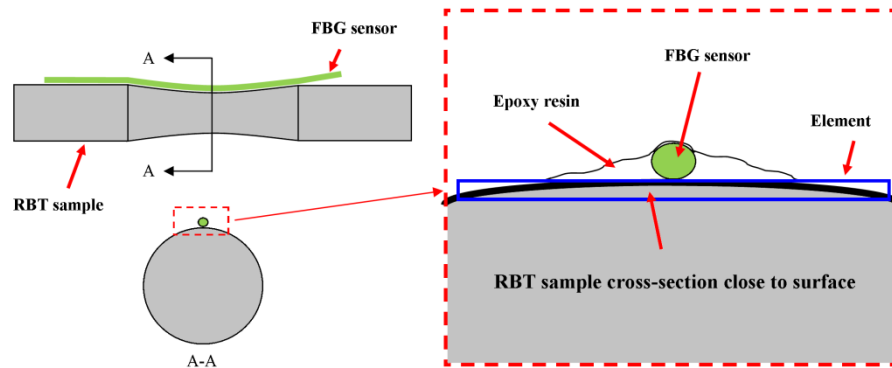
Figure 4-10: Embedded FBG sensor on the surface element.

To associate the FBG strain with the corresponding stress obtained from the VMP simulation, a mapping function was required. This function predicted a VMP strain equivalent to the FBG data. Figure 4-11a illustrates the strain versus angle curve from the FBG measurements and Figure 4-11b represents a VMP hysteresis curve for one reversal, schematically. The strain of the points A, B, and C from the FBG stress-angle curve (the maximum, minimum, and zero strains) were given a one-to-one correspondence to the strain of the points A´, B´, and C´. Then, the quadratic mapping function (Equation 4-12) was solved to find the VMP strain corresponding to the FBG strain data, shown schematically in Figure 4-12.

$$\varepsilon_{VMP} = a\varepsilon_{FBG}^2 + b \qquad\qquad (4\text{-}12)$$

In Equation (4-12), a and b are constant. To find the equivalent stress values of the FBG strain data, equivalent VMP strains were calculated by using the mapping function and then the corresponding stresses from the VMP hysteresis curve were extracted by linear interpolation. Finally, the FBG strain and VMP stress hysteresis curve were obtained by replacing the calculated values. Hereafter, this hysteresis is called VMP-FBG hysteresis.
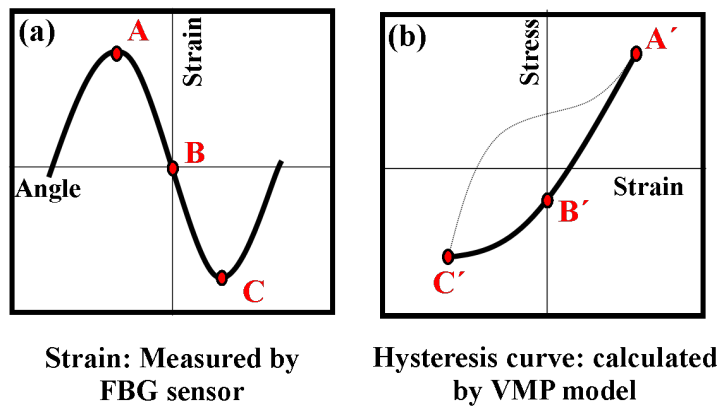
Figure 4-11: Finding the transfer function to relate: a) the strain-angle to b) the stress-strain curves
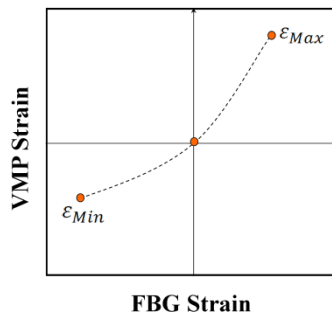
Figure 4-12: Mapping function that correlates FBG strain to VMP strain

In this research, the VMP-FBG hysteresis loops of the first and stabilized cycles were calculated using the first and stabilized cycles of the strain-control fatigue tests. However, the strain-control fatigue hysteresis curves cannot directly be employed for the cycles between these two hysteresis

curves because the number of cycles required to reach the stabilized hysteresis are not equal in both uniaxial strain-control and RBM tests. For example, when the bending moment equals 6.5 Nm, the sample needs to rotate approximately 2000 times in the RBM to become stable, whereas stabilization occurs after about 100 cycles in most of the strain amplitudes in uniaxial strain-control fatigue tests [16]. Hence, there cannot be a one-to-one correspondence between RBT cycles and uniaxial fatigue test cycles. Therefore, to evaluate RBT hysteresis by VMP simulation, equivalent strain-control cyclic hysteresis should be predicted. Figure 4-13 demonstrates the evolution of the peak and valley stresses of the hysteresis curves from the first cycle to the stabilized cycle. These curves were generated from the strain-control uniaxial tests at the strain amplitudes of 0.35% and 0.7% [16]. The selection of these curves was based on the strain range of the VMP hysteresis curves for a specific bending moment. To estimate the stress evolution of the VMP hysteresis curves between the first and stabilized cycles, the number of cycles in the strain-control test was normalized by the following equation:

$$cycle\% = \left(1 - \frac{stabilized\ cyclic\ number - Cyclic\ number}{stabilized\ cyclic\ number}\right) * 100 \qquad (4\text{-}13)$$

The cycle% is a parameter that represents the progress of the sample toward stabilization. Based on this definition, the stress versus number of cycles for two specified strain amplitudes was modified (Figure 4-14b and 14c). The stress response of the sample at any other strain between 0.0035 and 0.007 can be found by linear interpolation between these curves. Figure 4-14a depicts the first and stabilized VMP cycles for a bending moment of 6.5 Nm. The maximum and minimum points of the first and stabilized VMP curves are identified by A, B, C and D. For each point, a stress evolution curve for individual strain amplitudes was drawn out by interpolation between the 0.35% and 0.7% curves. These points, and the corresponding stresses versus cycle% (A′A, CC′, DD′, B′B), are shown in Figure 4-14b and 14c. The evolution of the peak stresses (CA), and the valley stresses (DB), can be estimated by linear interpolation between the curves A′A and CC′ in Figure 4-14b, and curves DD′ and B′B in Figure 4-14b and 14c.
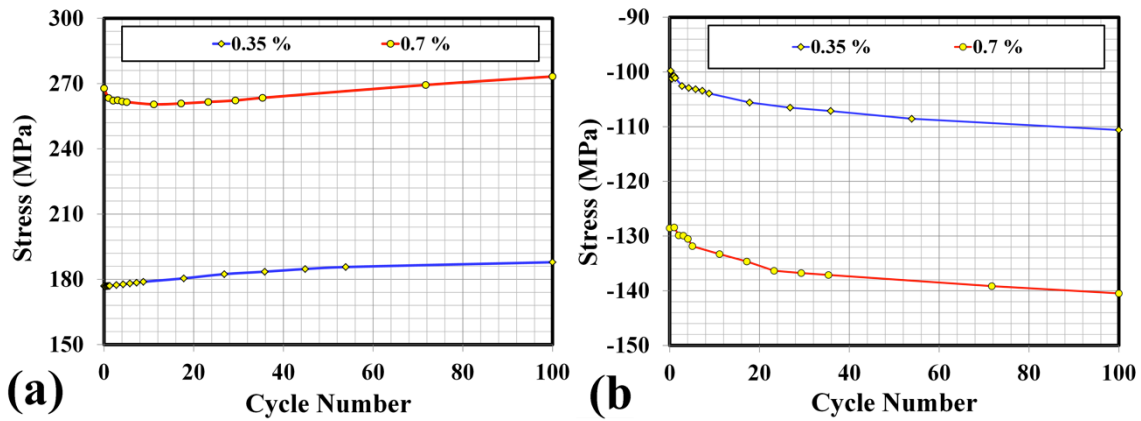
Figure 4-13: a) Peak stresses from the first cycle to the stabilized cycle of the strain-control fatigue test (ε=0.35% and ε=0.7%); b) valley stresses from the first cycle to the stabilized cycle of the strain-control fatigue test (ε=0.35% and ε=0.7%).
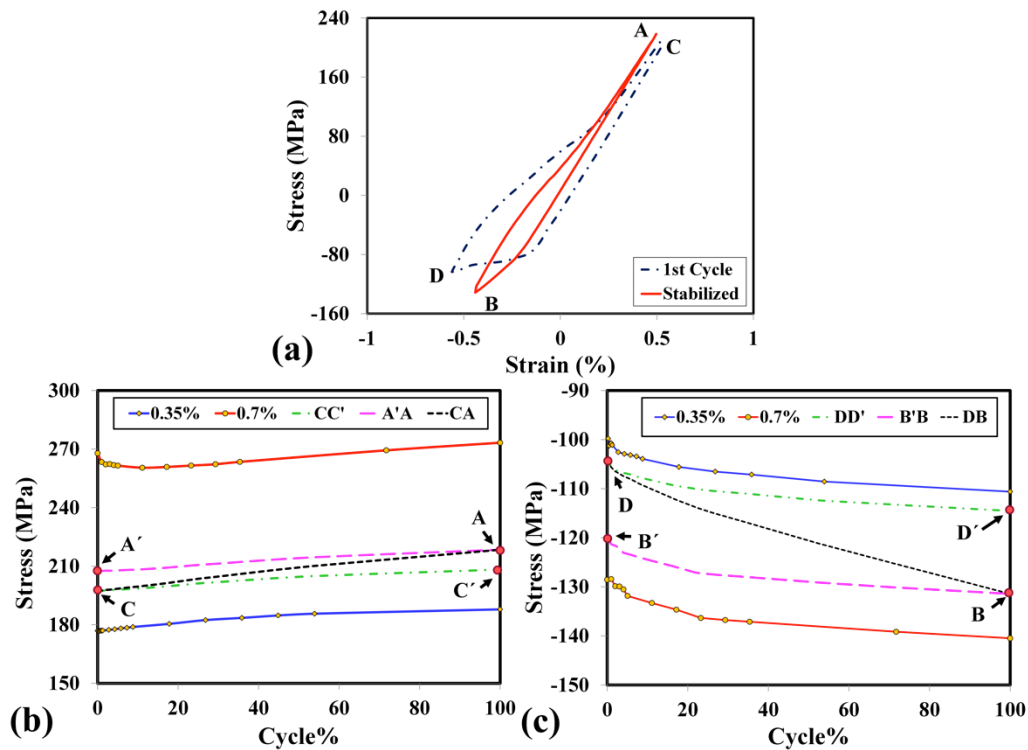
Figure 4-14: a) First and stabilized VMP cycle of the RBT; b) peak stresses versus cycle% (ε=0.35% and ε=0.7%); c) valley stresses versus cycle% (ε=0.35% and ε=0.7%).

52

Ultimately, by using curve fitting and the VMP method, the hysteresis curves between the first and the stabilized cycles were found using the stress value from the CA and DB curves and the strain found during experiments.

4.6 Summary

In this chapter, the proposed VMP model for simulating the RBT was introduced. The stress distribution in the cross section when the sample was under a constant bending moment, and the alternative method, were discussed. The VMP procedure for calculating the stress distribution and the corresponding strain in the cross section of the sample was explained. To do these calculations, the CSSC and monotonic curves were employed. To predict the unloading and reloading reversals by VMP, the reference curves were calculated by interpolation between the strain-control hysteresis loops of AZ31B extrusion obtained from experimental results. In the last section, the combining method for calculating the VMP-FBG hysteresis was explained. In addition, it was reported that the stress evolution between the first and stabilized cycles was calculated by linear interpolation between the experimental data of strain-control tests.

Chapter 5
Results and Discussion

In this chapter, the results of the experiments and simulations that were conducted are presented and discussed. Then, the hysteresis loops of the AZ31B extrusion samples under RBT were calculated using this experimental data and the VMP simulation results were extracted for different bending moments. Finally, the fatigue life curves for the AZ31B magnesium sample during load-control RBT, generated based on the VMP-FBG results and the fatigue life prediction method, were compared with experimental results to verify the accuracy of the stress-strain calculation proposed in this research.

5.1 Experimental Results

The deformation of the AZ31B extrusion rotating bending samples under different applied loadings was measured using the FBG sensors. Generally, two configurations exist in a sensor output: power versus wavelength and wavelength versus time. By stretching the sensor due to a tensile load on the sample, the wavelength of the sensor increases; in contrast, when a compressive load is applied to the sample the distance between the Bragg gratings (and consequently the wavelength of the sensor) decreases. Figure 5-1 shows the output of the FBG sensor at three different positions of the rotating sample in one reversal: neutral axis, maximum tension, and maximum compression. In this figure, the inset schematically shows the physical position of the sensor on the sample surface during a revolution. The output signal at the neutral axis was the same as the output signal of the FBG recorded before installation on the machine, showing a zero state of stress. Therefore, the location of the neutral axis in plastic deformation can be easily found by considering the position of the sensor, in spite of the asymmetric behaviour of the material. On the other hand, when the sample experienced tensile stress, the sensor output signal as well as the peak with maximum intensity shifted to the right of the neutral axis (blue signal), and shifted to the left (red signal) of neutral axis when the sample was under compressive stress. The magnitudes of the shifted signal were not equal for the AZ31B specimen because of the asymmetric behaviour of this material.

Another output of the sensor is wavelength versus time, which is constructed by tracing the position of the maximum intensity peak versus time. During rotation, the FBG sensor signal generates a sinusoidal curve. The peak of this sinusoidal curve represents the maximum wavelength that was

induced due to the maximum tensile loading. The valley of the sinusoidal curve demonstrates the minimum wavelength recorded due to the maximum compressive applied loading. In order to more easily interpret the results, the wavelength changes were converted to mechanical strain using Equations (2-8) under constant temperature, and the time of the rotation was transformed into the rotation angle (i.e., the position of the sensor on the sample).
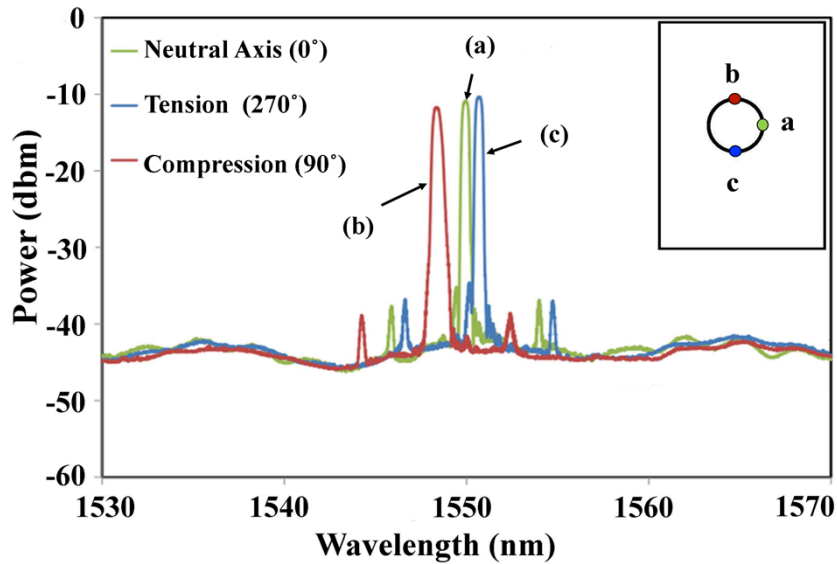
Figure 5-1: FBG sensor power output versus wavelength at three different positions: a) neutral axis; b) compression; c) tension

Figure 5-2 shows the recorded strain values obtained from an FBG sensor versus the position of the sensor for four different bending moments: 2.5, 3.5, 4.5 and 5.5 Nm. In one full cycle (two reversals) of the sample, the FBG readings showed maximum tension (the sensor at the bottom) and maximum compression (the sensor at the top). Depending on the initial location of the FBG sensor before starting each test, the FBG could have gone through compression or tension reversals first. In the case of the 2.5 and 3.5 Nm tests, the FBG sensor was under compression initially. The other two experiments started with the FBG sensor at the bottom of the sample and so tensile stress was experienced first.

The 2.5 and 3.5 Nm bending moments corresponded to elastic deformation due to the symmetrical strain fluctuation. Higher bending moments caused plastic deformation that is depicted by asymmetric

strain curves. This behaviour was observed because the yield strength of AZ31B under compression is less than the yield strength under tension.
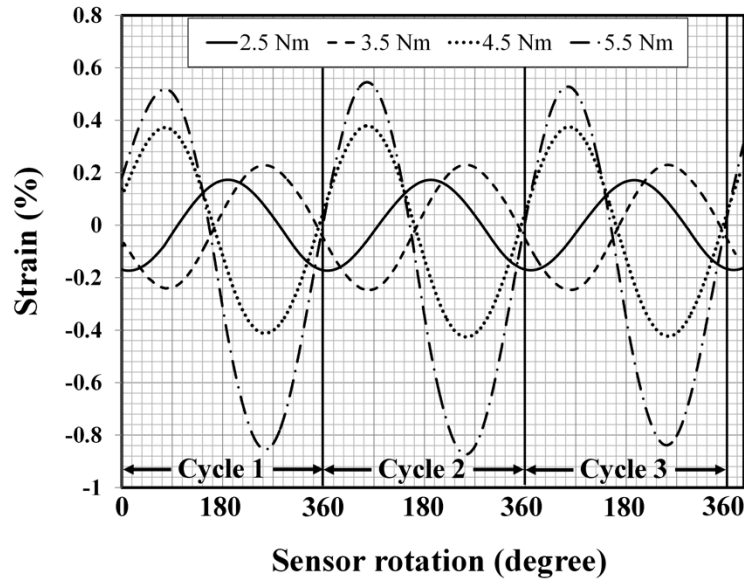
Figure 5-2: Strain of the as-received sample during the first three cycles of RBT under four different bending moments: 2.5, 3.5, 4.5 and 5.5 Nm.

To examine the accuracy of the measured results, the strains of the sample under the bending moments of 2.5 and 3.5 Nm were calculated using the elastic flexural equation and compared with the strains measured by the FBG sensor. According to the results, which are listed in Table 5-1, the strains measured by the sensor are close to the elastic flexural calculated strain with only a 1.2% difference. This error percentage is the same for both the material stress relief and as-received samples in the elastic region. The low error percentages in the elastic regime, and the agreement of the FBG results with the extensometer results in both the elastic and plastic regimes (see Section 3.2.4), assure the reliability of the FBG sensor results.

Table 5-1: Comparison between obtained strain from the analytical solution and measured strain by the FBG sensor

Bending moment (Nm)	Stress (MPa)	Strain (σ/E)(%)	Strain FBG (%)	Error (%)
2.5 (stress relief)	73.4	0.163	0.165	1.2
3.5 (as-received)	102.75	0.228	0.2304	1.2

In summary, Figure 5-1 and Figure 5-2 reveal that the FBG sensor is able to demonstrate the strain of the AZ31B in low- and high-cycle fatigue during the RBT. They also confirm the asymmetric behaviour of the magnesium alloy under plastic deformation. The measured strains of the sample in the elastic region were matched to the strains calculated with the elastic equation.

5.2 Variable Material Property Modeling Verification

The VMP simulation was set up to run in the MATLAB program. This simulation was verified by solving an elastic-perfectly plastic problem and comparing the obtained results with those generated by the analytical solution. In this case study, the VMP program was customized to find the distribution of the stresses and residual stresses in a member of uniform rectangular cross section 50 by 120 mm, under a bending moment of 36.8 KN.m. The member is made of an elasto-plastic material with yield strength of 240 MPa and a modulus of elasticity of 200 GPa. The thickness of the elastic core, the stress distribution in the cross section of the sample and the residual stress distribution were calculated using established analytical solution [46]. Figure 5-3a illustrates that the thickness of the elastic part of the cross section was 80 mm which was surrounded by 20 mm plastic deformation on both sides. The behaviour of the elastoplastic material was expressed with stress versus strain, obtained by modeling (Figure 5-3b). In addition, the distribution of the residual stresses, calculated by summing the stresses obtained from loading and unloading of the member, is shown in Figure 5-3c. These results were in good agreement with the analytical solution; hence, the MATLAB code was qualified to use for analyzing the elasto-plastic behaviour of AZ31B under different bending moments.
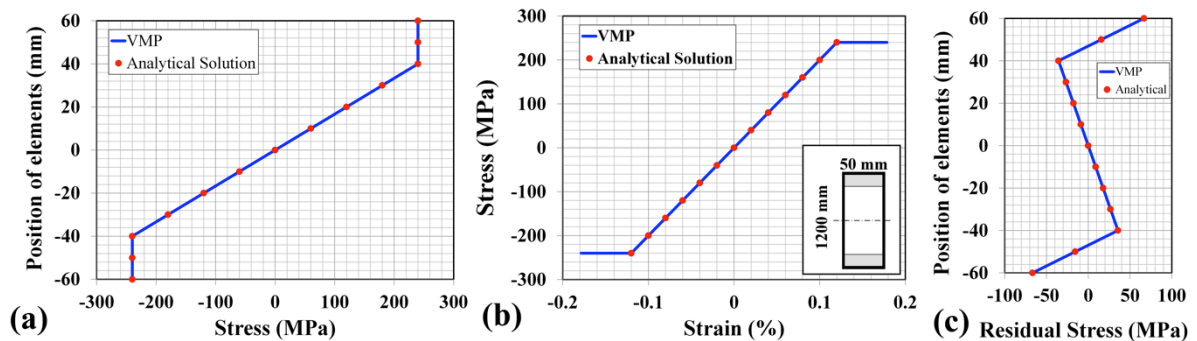
Figure 5-3: Distribution of a) stresses in loaded member; b) stress-strain loading curve; c) residual stresses upon removal of load

After that, the program was developed to obtain the stress and strain responses of the asymmetric material AZ31B for four different bending moments of 3, 7, 10, and 12 Nm under loading. Figure 5-4 depicts the loading of the elements superimposed on the CSSC of AZ31B extrusion magnesium alloy. Since the cross section of the sample was divided into 100 elements, the loading curves consisted of 100 data points, and each of them expressed the specific stress and strain of an element. The stress and strain obtained for these elements overlaid exactly on the experimental CSSC, in both the elastic and plastic regimes. Therefore, the VMP model is able to predict various deformation conditions, such as fully elastic, elasto-plastic, and completely plastic deformation. The asymmetric behaviour of AZ31B under loading was clearly revealed in high-applied bending moments. As in the case with the anisotropic monotonic behaviour under uniaxial testing, the basal plane texture in extruded magnesium alloy is responsible for activating the different deformation systems under tension and compression. These systems can cause the asymmetric behaviour of the material under RBT. The stress and strain values at maximum compression were completely different than at maximum tension under a constant load due to anisotropic yield strength in the tension and compression parts of the plastic regime.
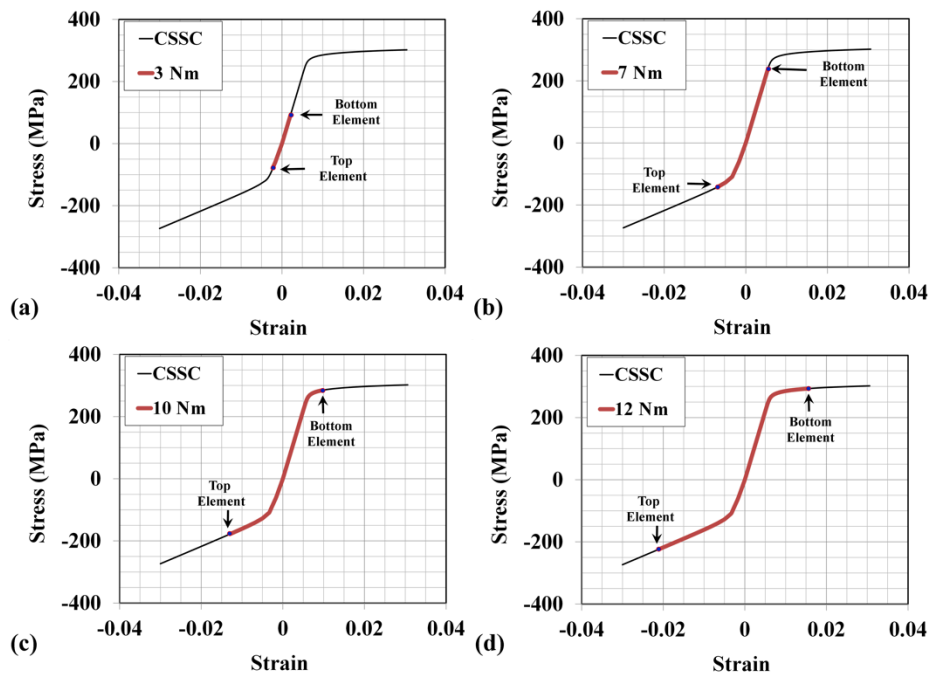
Figure 5-4: VMP loading curves superimposed on the CSSC of AZ31B extrusion for four different bending moments; a) 3 Nm; b) 7 Nm; c) 10 Nm; d) 12 Nm

Moreover, the asymmetric behaviour of AZ31B extrusion leads to displacement of the neutral axis when the sample plastically deformed. The tensile yield strength is more than the compressive; hence, more plastic deformation is observed in the compression side. Figure 5-5a reveals the displacement of the neutral axis during loading of a sample under a bending moment of 10 Nm. The inset shows schematically the location of the neutral axis in the cross section of the sample. Since the upper part was under compression and the lower part of the sample was under tension, the neutral axis shifted downward. Hence, more than half of the cross section was under compressive stress. When the bending moment was increased, the displacement of the neutral axis was increased, and the compression side of the cross section became larger than the tensile part. Figure 5-5b illustrates the displacement of the neutral axis position for different bending moments in the range of 5 to 10 Nm, which confirms this statement.
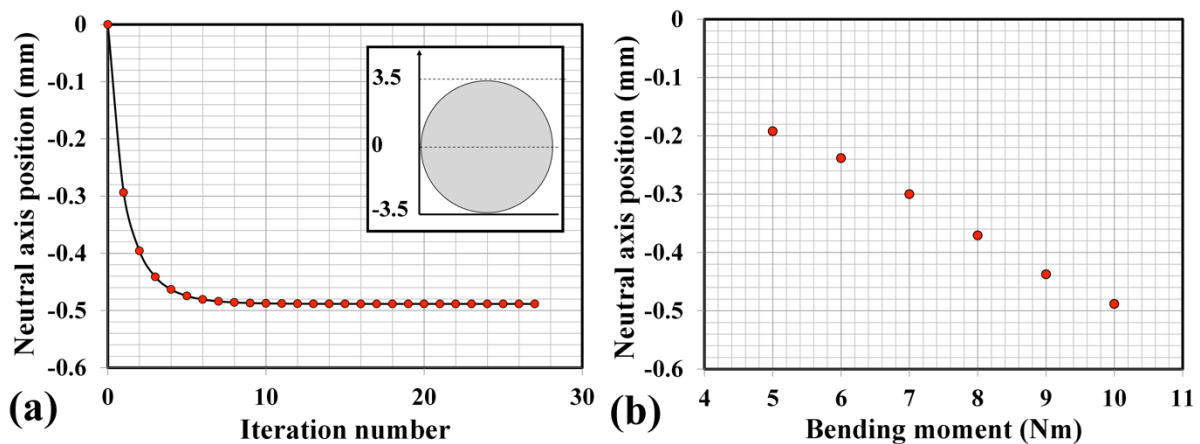
Figure 5-5: a) Displacement of the neutral axis during VMP iterations, (M=10Nm); b) position of the neutral axis versus applied bending moments

The response of the stress for all elements under the applied loading in the elastic regime can be easily obtained based on the flexural equation, however, in low-cycle fatigue, the stress was determined for each element individually by using the proposed VMP method. Since the top element was under the maximum compressive loading and the bottom element experienced the maximum tensile loading, the stress distributions under different applied loads were obtained for these two critical elements. Figure 5-6 shows the response of the stresses for different ranges of applied loadings. The plastic deformation was initiated from 80 N, which was equivalent to a bending

moment of 4 Nm under compressive loading. The slope of the curve in the compression part changed after 80 N loading. The slope of the tension was constant up to 130 N, and after that the sample was plastically deformed in tension. The stress values for 80 N and 130 N under compression and tension represent the compressive and tensile yield strengths, respectively, and confirm anisotropic yield strength in this material.
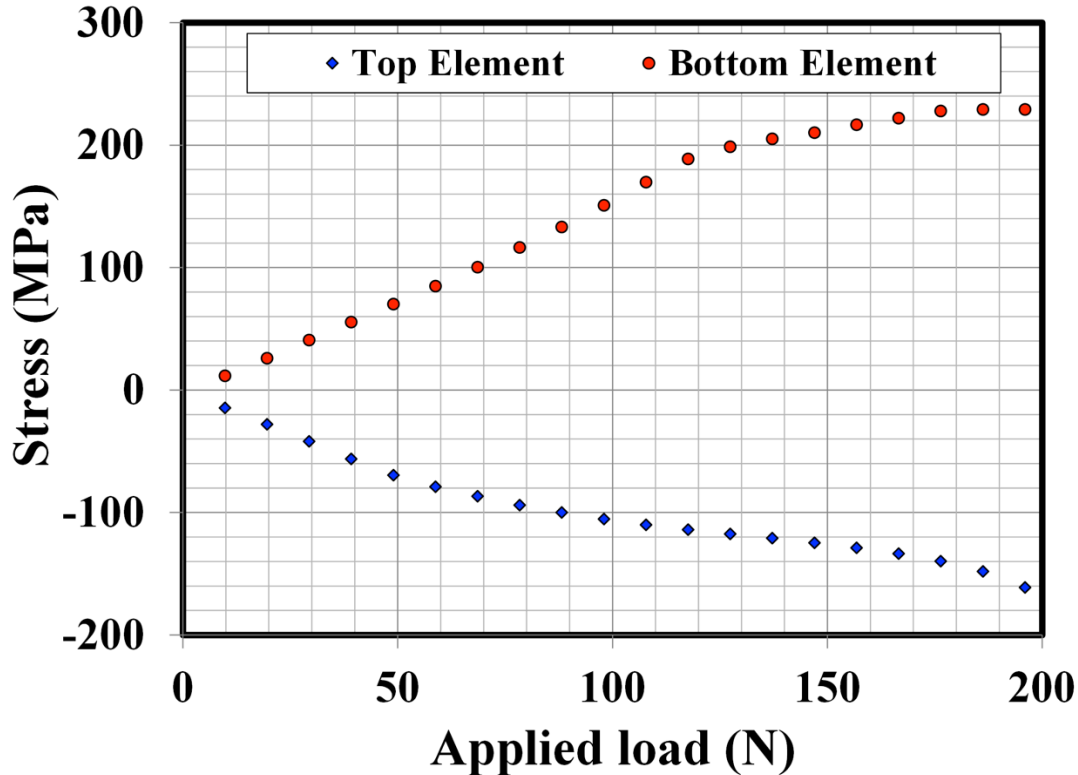
Figure 5-6: Stress versus applied load in RBT

The stress distribution inside of the sample from the top element to the bottom element (100 elements in total) can be calculated versus the position of the elements. When the position of the elements changed from zero (neutral axis) to the maximum or minimum, the induced stresses in the elements alternated from zero at the neutral axis to maximum tension or compression. In the proposed VMP model, the stress was considered to be constant for all material points of an element resulting in equal stresses at points A and C (see inset in Figure 5-7). However, the stress of each element was different and changed based on the position of the elements under a constant bending moment. Figure 5-7 shows the stress changes under the bending moment of 8 Nm versus angle. In this case, the neutral axis was changed from 0° to -7°. The absolute value of the maximum tension stress was higher than

60

the maximum compression stress and occurred at -90°. Moreover, all of the elements positioned between -40° to 5° were deformed elastically, whereas the rest of the cross section experienced plastic deformation. In this situation, the number of elements that deformed plastically in the compression part was greater than in the tension part due to anisotropic yield stresses in tension and compression.
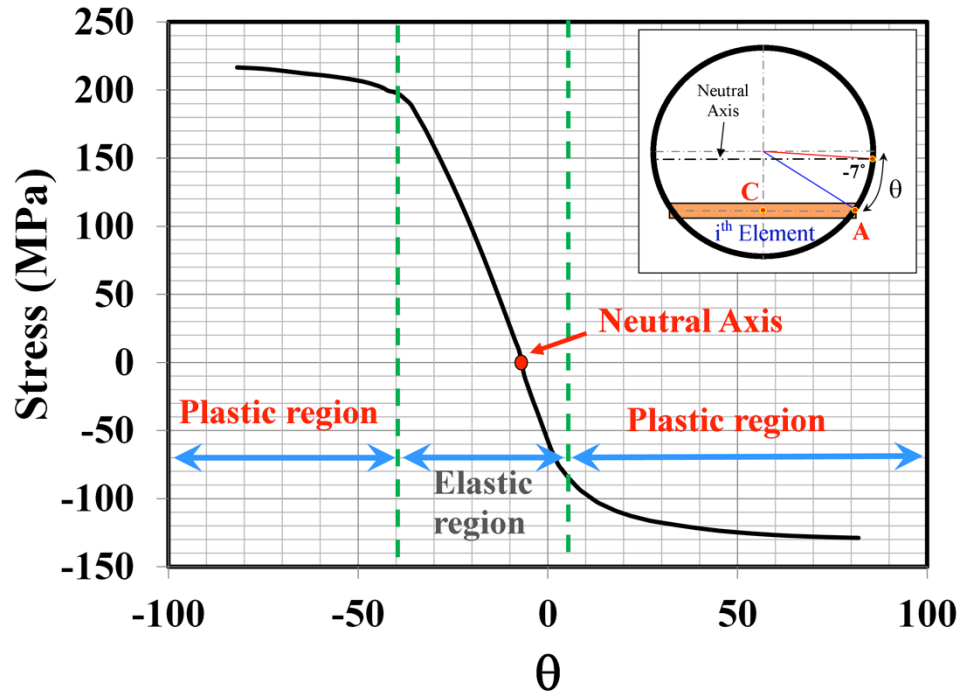
Figure 5-7: Stress versus angle (M=8 Nm)

To continue the investigation into the cyclic behaviour of the material under load-control conditions based on the VMP, it was necessary to obtain the stress and strain responses of each element during the unloading and reloading reversals. The evaluation of the hysteresis curves for the top and bottom element are essential to this, since they are under maximum compressive and tensile stresses due to their maximal distance from the neutral axis. Moreover, in the alternative method, cracks are initiated and propagated from these elements [102]. Figure 5-8 depicts the hysteresis stress-strain curves for the bottom element of the samples under different bending moments, which calculated by using stabilized strain-control curves. Elastic deformation was observed when the samples were under bending moment equal to 2.5Nm. However, by increasing the bending moments, the material was deformed plastically and the hysteresis curves became asymmetric.

61

In the current study, the predicted hysteresis curves, which calculated using the stabilized strain-control hysteresis curves, were not closed. However, a stabilized cycle is a hysteresis loop for which the behaviour of the material remains constant for the rest of subsequent cycles. This apparent inconsistency may be at least partially explained by the following two conjectures. First, in this simulation the strain-control cyclic curves were used as reference curves for the VMP simulation in load-control RBT by assuming that the CSSC represented a material property that was independent of the condition of loading. This is true for symmetric materials [17]. However, for asymmetric materials as explained in Section 2.2.5, the stabilized stress and strain control cyclic curves are not exactly the same based on the comparison between the published data in the literature by different authors, and it is also expected that for load-control condition would be different. Second reason could be the prediction method, which was employed to find the reference curve for unloading and reloading reversals. It was conducted based on the assumption that reversals follow a strain control hysteresis curve. Therefore, to find the corresponding unloading or reloading curves, the element's strain value at the end of loading was selected as a point on the transferred unloading/reloading curves (ε_P in Figure 4-9). By this assumption, the reference curve and the CSSC cross each other at ε_P; however, the VMP model predicts a point on the reference curve, which is not on the CSSC due to the load-control condition and asymmetric behaviour of AZ31B.
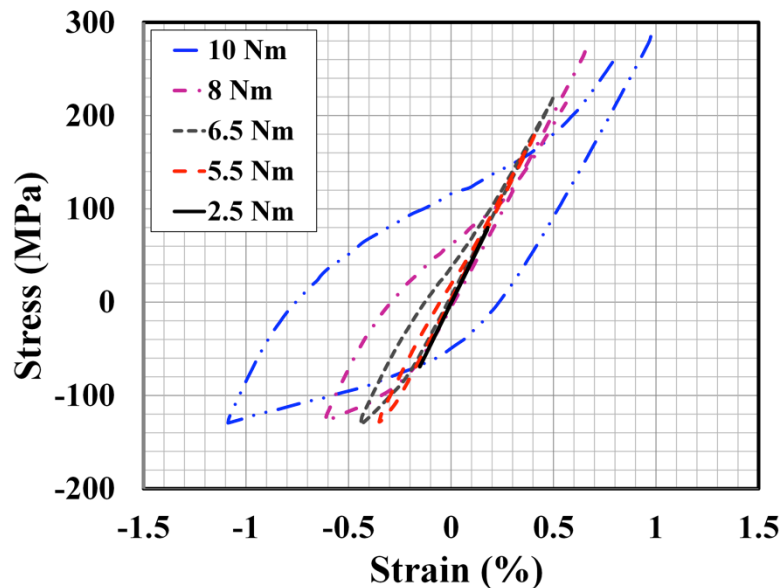
Figure 5-8: The hysteresis curves of bottom element as predicted by the VMP simulation for different bending moments.

62

5.3 Combining Experimental Results and Variable Material Property

Obtaining cyclic hysteresis curves is essential to evaluate the fatigue behaviour of the AZ31B extrusion under load-control condition. The stress responses of the material can be predicted by VMP simulation based on the alternative method, in which a constant sample is under fluctuating loading. As mentioned in section 4.1, it was reported that the predicted stress by alternative method is same as the RBT, while the axial strain range of the alternative method is lower than the RBT (Figure 5-9) [102]. Therefore, the VMP stress responses based on the alternative method can be employed to build the hysteresis loops, however the strain response of the VMP should be replaced by more accurate data. As previously mentioned, the FBG sensor was employed to measure the strain of the sample during the RBT. Then, the stress-strain responses of the bottom element were obtained by VMP simulation under load-control rotating bending experiments. Based on the mapping function explained in Section 4.5, the FBG measured strain data was substituted for the VMP strain to generate the VMP-FBG hysteresis loops under load-control conditions. It is important to mention that when a sample rotates downward (tension part) from the neutral axis during the first cycle of the experiment, the obtained strain values should be replaced with the VMP strain responses of the bottom element. In contrast, when the sample is rotated upwards (compression part), the VMP hysteresis obtained for the top element should be employed to obtain the VMP-FBG cyclic curves.
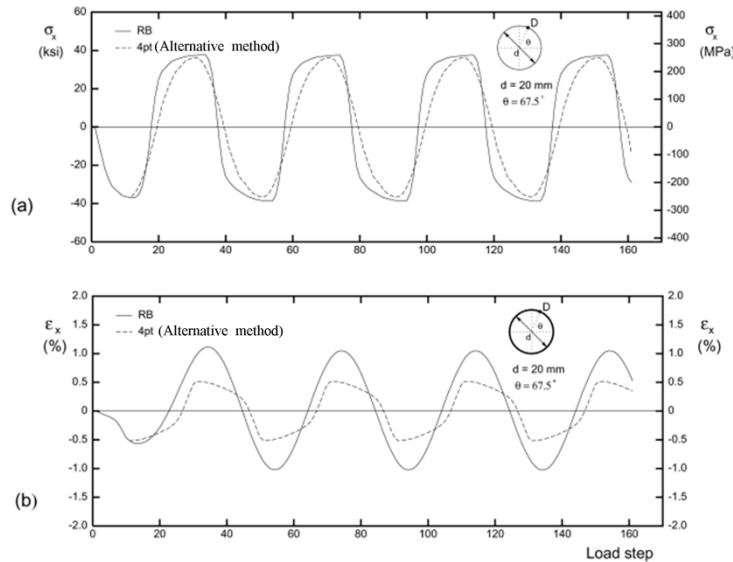
Figure 5-9: (a) Stress and (b) strain responses at point D (67.5°) of the cross section for RBT and alternative method [102]

63

In this section, the VMP-FBG hysteresis curves for three bending moments, 2.5 Nm, 6.5 Nm, and 5 Nm, were generated. In these experiments, all of the samples rotated towards tension parts at the beginning of the tests, hence, the results obtained from the bottom element were employed to calculate the VMP-FBG curves. In addition, the accuracy of the VMP-FBG hysteresis curves was examined by designing a specific strain-control uniaxial test.

The first observations were done at a bending moment equal to 2.5 Nm. The VMP stress and strain responses of the bottom element for the first and stabilized cycles are demonstrated in Figure 5-10. A symmetric and linear cyclic deformation was observed due to elastic deformation. Some discrepancy between the first and stabilized cycles and the non-closing hysteresis loops may have originated from the experimental references curves and/or the numerical calculation VMP method as mentioned before.

After combining the VMP stress responses and FBG strain measurements, the VMP-FBG curves were generated. Figure 5-11 shows the first and stabilized cycles for the elastic range of 2.5 Nm. The strain of the sample was monitored from the first cycle to the 100,000th cycle. This observation uncovered that the behaviour of the sample was uniform; the strain amplitude was constant during the rotation in high-cycle fatigue testing. The stress amplitudes of the first and stabilized cycles were almost identical and depict the linear behaviour of AZ31B extrusion under the bending moment of 2.5 Nm.
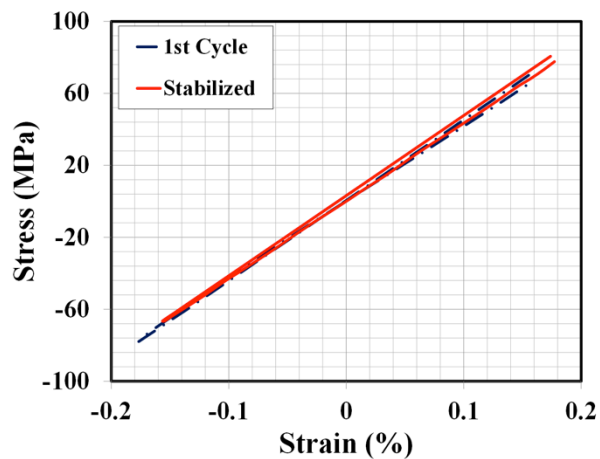
Figure 5-10: VMP hysteresis curve (M=2.5 Nm)
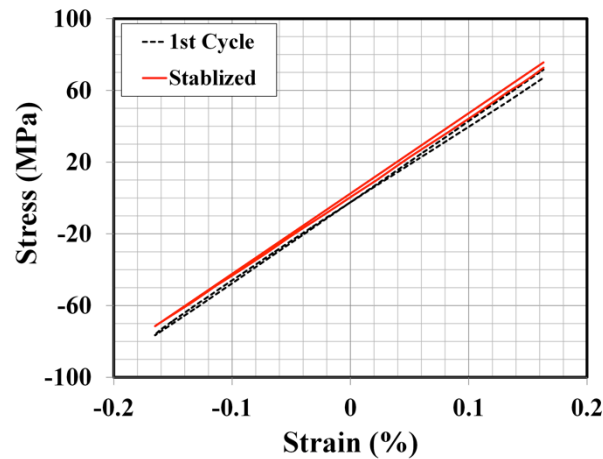
Figure 5-11: VMP-FBG hysteresis for the first and the stabilized cycles (M=2.5 Nm)

In the second case, a bending moment of 6.5 Nm was applied to the sample. This bending moment can provide enough stress to deform the sample plastically under tension and compression. Figure 5-12 shows the simulated stress-strain curve of the initial tensile loading using the monotonic curve, and the unloading and reloading reversals obtained using the first cycles of the strain-control experiments, and the stabilized cyclic hysteresis curves. The presented loading curve of Figure 5-12 shows that plastic deformation of the sample occurred during loading.
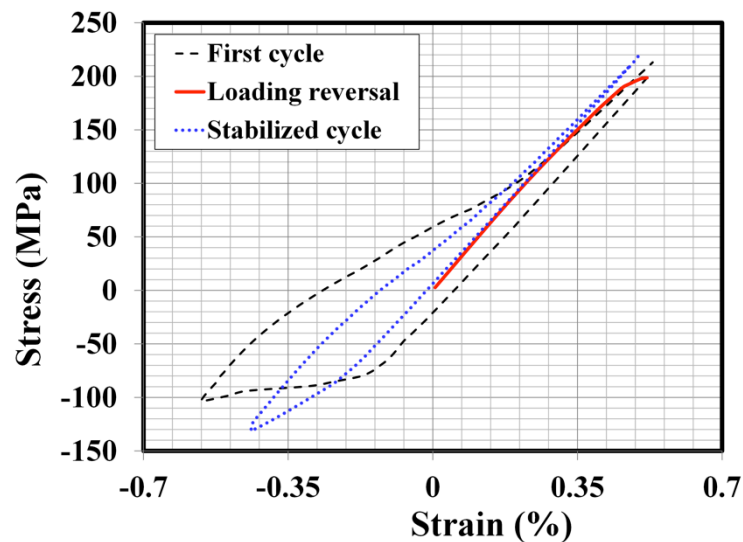
Figure 5-12: Loading reversal, the first cycle, and stabilized cycle hysteresis curve obtained by VMP (M=6.5 Nm)

In the experimental part of this case, the strain responses of an AZ31B extrusion sample were measured by an FBG sensor under a 6.5 Nm bending moment over 5,000 cycles. Figure 5-13 shows the strain of the sample approximately follows a sinusoidal curve from the first cycle to the 5,000th cycle number. However, the strain amplitude was decreased as the number of cycles increased, and the peak strain values were not equal to the valley strain values. Inequality of the peaks and valleys of the strain indicate more compressive deformation due to the lower compressive yield strength versus the tensile strength.
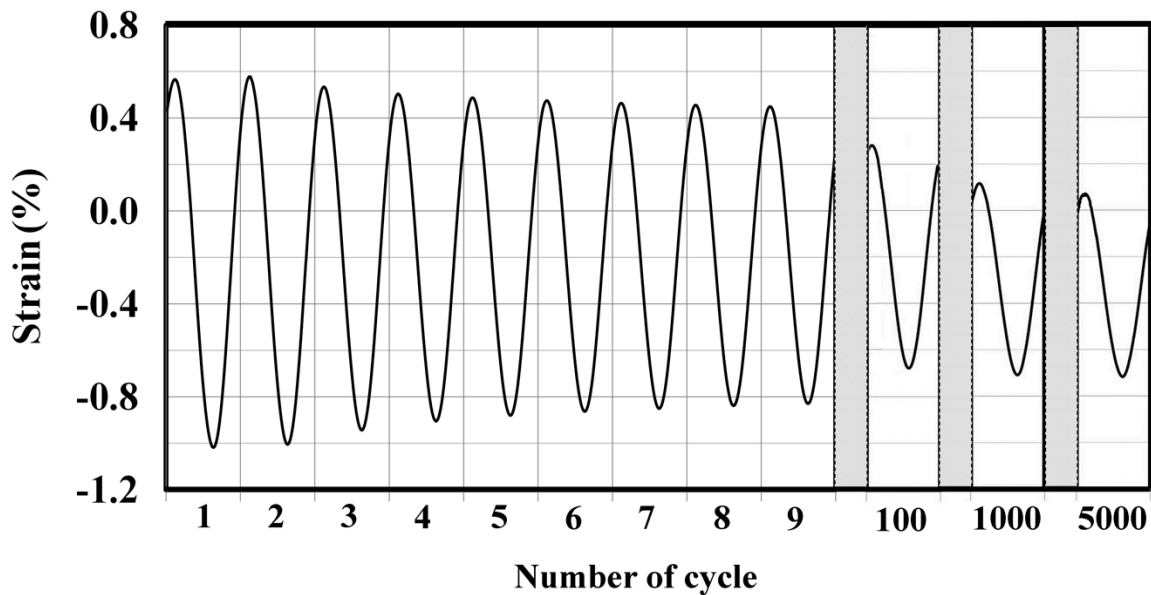
Figure 5-13: Stain of the stress relief sample (M=6.5 Nm)

Figure 5-14 show the changes in strain amplitude and mean strain of the sample under RBT. The strain amplitude of the sample in the second cycle is a little bit larger than in the first cycle. From the 3rd cycle number to the 2,000th, the strain amplitude as well as the absolute values of the peak and valley strains was reduced. During the first 10 cycles, the mean strain of the sample was increased slightly, but remained approximately constant between the 10th and 100th cycles. After that, a negative mean strain was developed in the sample from cycle number 100 to 2,000. From the 2,000th to the 5,000th cycle, the strain amplitude as well as the mean strain remained almost constant, leading to the conclusion that the cyclic behaviour of the sample had become stable.

Albinmousa reported that AZ31B extrusion has a considerable plastic strain recovery [47]. It was also reported that during a stress-control uniaxial cyclic test of AZ31B magnesium alloy with a mean stress equal to zero, ratcheting occurred and the peak strain decreased and valley strain increased as the number of cycles increased [27, 28, 31, 105]. In this regard, the stress-control hysteresis loop narrows with as the number of cycles increases due to the cyclic hardening behaviour of AZ31B. As discussed in Chapter 2, different deformation mechanisms can be activated during the cyclic deformation. A significant amount of strain was observed during the first cycle when the sample was plastically deformed under a stress-control condition. Twin deformation was responsible for a large amount of strain in the compressive reversal. In the next (tensile) reversal, most of the twinned grains were detwinned; however, some residual twins would remain in the material. The residual twins accumulate during cyclic loading and can increase the critical resolved shear stress of twining in the next loading reversal. Increasing the critical resolved shear stress makes the material harder, as it makes the activation of twin deformation more difficult. Therefore, the strain amplitude decreases as the number of cycles increases [56]. The same trend is observed in the load-control testing condition (i.e., the amplitude of the strain is decreased during the cyclic loading). Based on the stress-control results, the hysteresis became symmetric and narrow and the strain amplitude became almost constant after a few cycles. However, this research depicts that in the load-control rotating bending experiments, more cycles were required to reach the stable condition [56, 8]. The findings may be related to the nature of the loading conditions in which both the stress and strain amplitudes were variable. Moreover, a comparison between the peak and the valley strains confirmed the asymmetric behaviour of AZ31B under 6.5 Nm, which is compatible with the data presented data in Figure 5-2. Also, there was a noticeable negative mean normal strain of -0.32% in the stabilized cycles. This is another indication of AZ31B's asymmetric behaviour, which is due to the lower yield value in compression, and hence larger compressive strains compared to tension values.
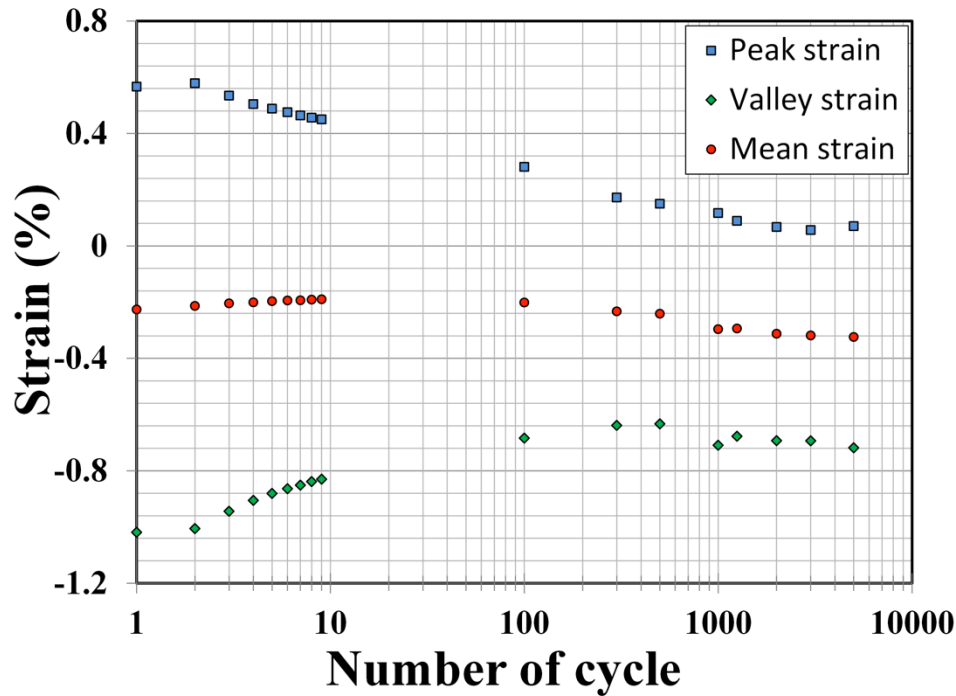
Figure 5-14: The peak, valley, and mean strains versus number of cycles (M=6.5 Nm)

The FBG data and VMP simulation results were employed to calculate the VMP-FBG hysteresis curves for different cycles when the sample was tested under a 6.5 Nm bending moment. Figure 5-15 depicts the load-control cyclic behaviour of AZ31B, which was obtained based on the VMP-FBG results. This observation demonstrates the inconstancy of the stress amplitudes during the cyclic loading. The stress values of 48 ± 151 MPa during the first cycle increased to 44 ±172 MPa by the stabilized cycles. Figure 5-16 shows the trend of the peak and valley stress changes versus the number of cycles. Based on this graph, the rate of increasing peak stress is around 9% while the shifting rate of valley stress shows a reduction of 21% from the first to the stabilized cycles. This difference can be attributed to differences between the CSSC and monotonic tension-compression tests of AZ31B (Figure 4-5). This difference in compression is higher than the tension. Therefore, during the stabilizing process in which the behaviour of a sample gradually changes from the monotonic curve in the first cycle to the CSSC in the stabilized cycle, more change should be observed under compression. The same increasing trend in stress amplitude was reported for strain-control cyclic tests. These changes were attributed to the cyclic hardening characteristics of AZ31B [47, 51, 96]. On the other hand, the strain amplitude was reduced during the cyclic loading and a significant amount of compressive mean strain remained in the stabilized hysteresis curves. As a consequence, the peak and

68

valley stress, and the strain shift, and the hysteresis loops become narrower and narrower as the number of cycles increases. This is evidence of cyclic hardening in the AZ31B magnesium sample. Moreover, ratcheting was observed and the peak points of the hysteresis loops shifted in the compressive direction and the valley points shifted in the direction of tension due to the specifications of the cyclic hardening.

Load control stress-strain hysteresis curves can be compared with stress- and strain-control fatigue tests with a stress and strain in the range of the presented results from Figure 5-15. Based on the literature, the strain- and stress-control cyclic hysteresis loops in this loading condition are asymmetric, in which the downward halves are convex, and the upward halves are concave with an inflection point [56]. This trend was also seen in the results obtained in this research (Figure 5-15) and can be explained by different deformation mechanisms. The twinning deformation mechanism is activated in the downward side of the hysteresis loop whereas in the upward sides there are two different deformation mechanisms, detwinning and dislocation slip, which leads to an inflection point on the upward side of the hysteresis loop.
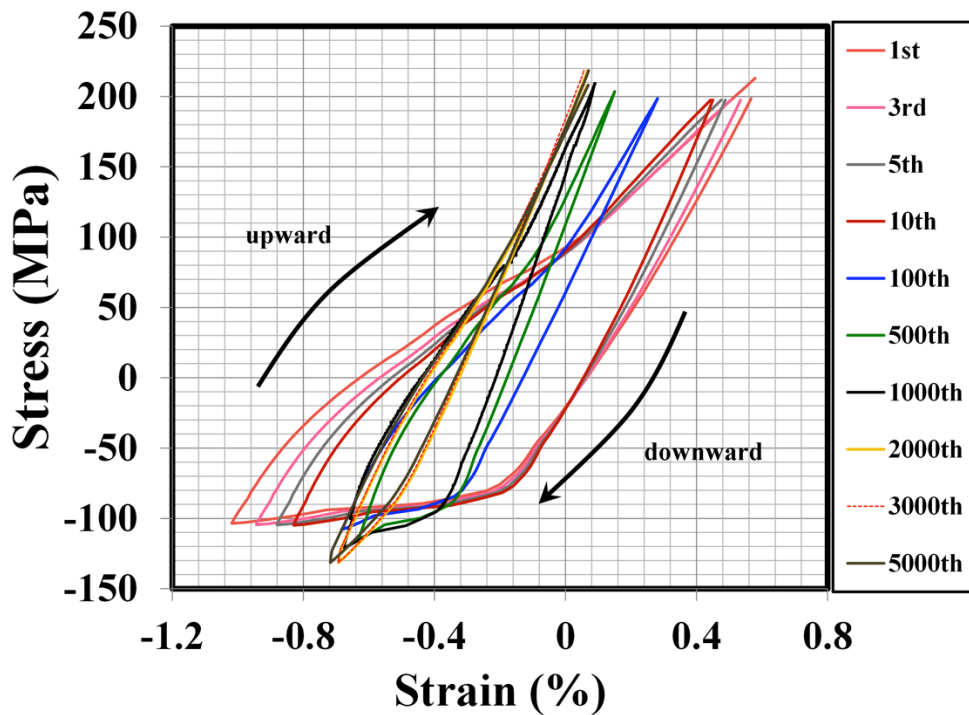
Figure 5-15: VMP-FBG hysteresis curves for different cycles under (M=6.5 Nm)
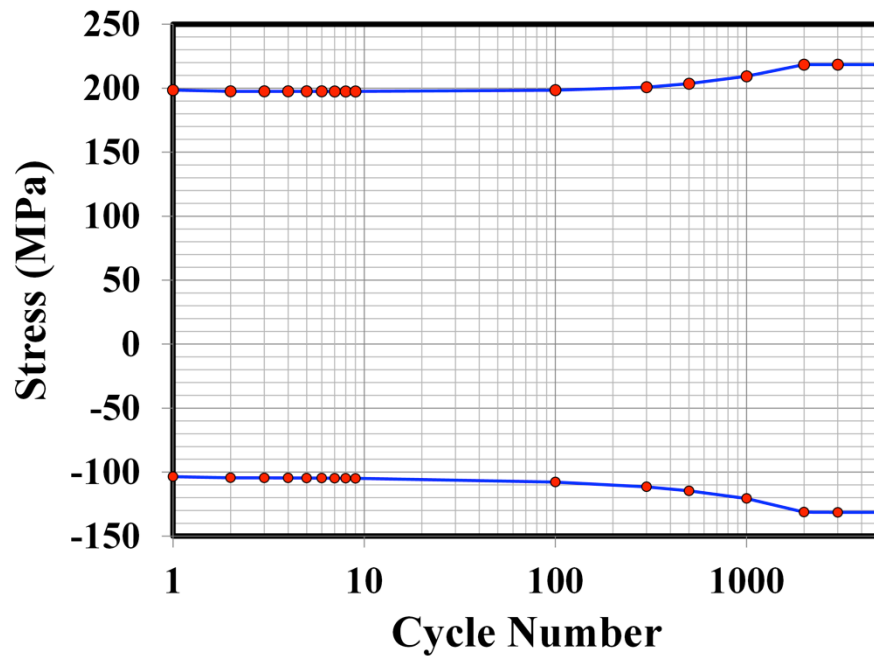
Figure 5-16: Peak and valley stresses versus the number of cycles for RBT with a 6.5 Nm bending moment.

To verify the VMP-FBG results, an experiment was proposed. The uniaxial push-pull test was conducted under specified strain-control condition for 9 cycles. In this test, the strains imposed on the sample were the strains measured by the FBG sensor for the corresponding cycles under the RBT. Figure 5-17 depicts the first cycle of the experiment that was superimposed on the first cycle of the VMP-FBG. The peak and valley strains and stresses are close to each other in the experimental results and VMP-FBG cycles. The hysteresis loops are almost similar. The difference between them may originate from the simulation algorithm employed to match the FBG and VMP strains; the upward and downward sides of VMP-FBG curves were calculated by using a quadratic equation which fitted on the three points. To obtain more precise unloading and reloading curves, more points and/or more advanced mathematical methods would be required.
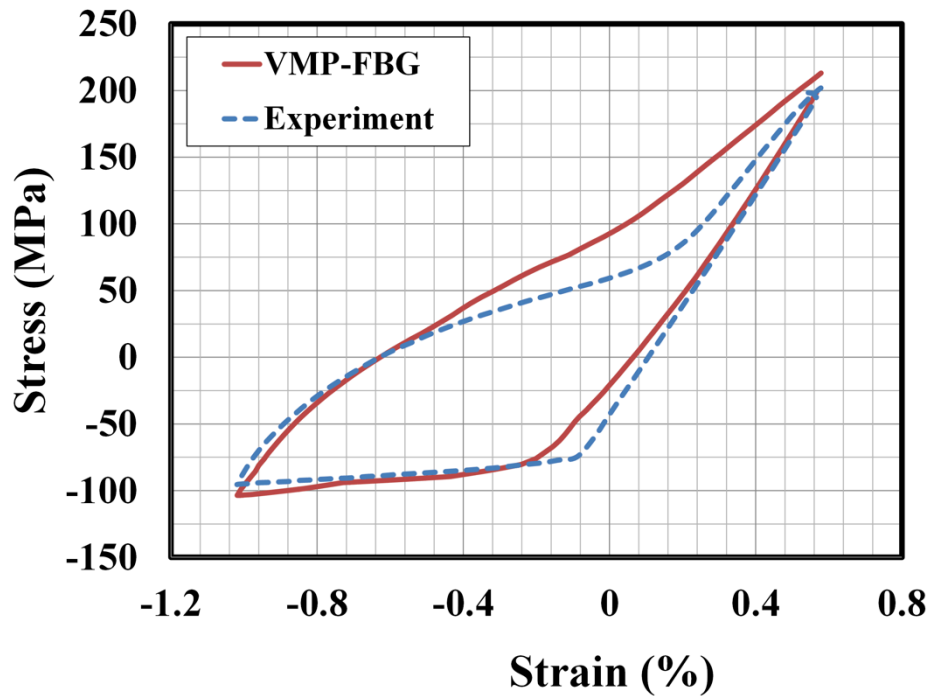
Figure 5-17: The first cycle of the VMP-FBG hysteresis curve and the first cycle of experimental test.

The experimental results of the nine cycles are shown in Figure 5-18a. For the sake of comparison, the first 9 cycles of VMP-FBG curves are also presented in Figure 5-18b. It can be observed in Figure 5-17 that the stress level of the uniaxial push-pull experiments and VMP-FBG hysteresis loops are in the same range at the first cycle. However, the rate of the peak and valley stresses changed during the 9 experiments and the subsequent hysteresis loops are different, especially for the valley stresses. The inset of Figure 5-18b demonstrates a close-up view of the valley stress of VMP-FBG curves that confirms the same trend as the push-pull experiments, but at a lower rate. This can be justified by the comparison between the first cycles of strain-control reference hysteresis loops. Figure 5-19 shows the 3rd, 6th and 12th cycles, which superimposed on each other for three different strain amplitudes [16]. Based on the reference curves that were used in the VMP simulation, a high rate stress change does not exist, particularly in the compression parts, and as a consequence, the VMP-FBG curves are not able to predict the stress changes of the first 9 cycles of the proposed experiment.

Comparison between the VMP-FBG hysteresis loops and the push-pull experiment with the same strain range proved that the VMP simulation was able to predict the peak and valley stresses with a good approximation. In addition, the strains were measured accurately by the embedded FBG sensor

71

during RBT. Hence, the VMP-FBG hysteresis loops can predict the behaviour of the AZ31B magnesium alloy under load-control RBT with a good approximation.
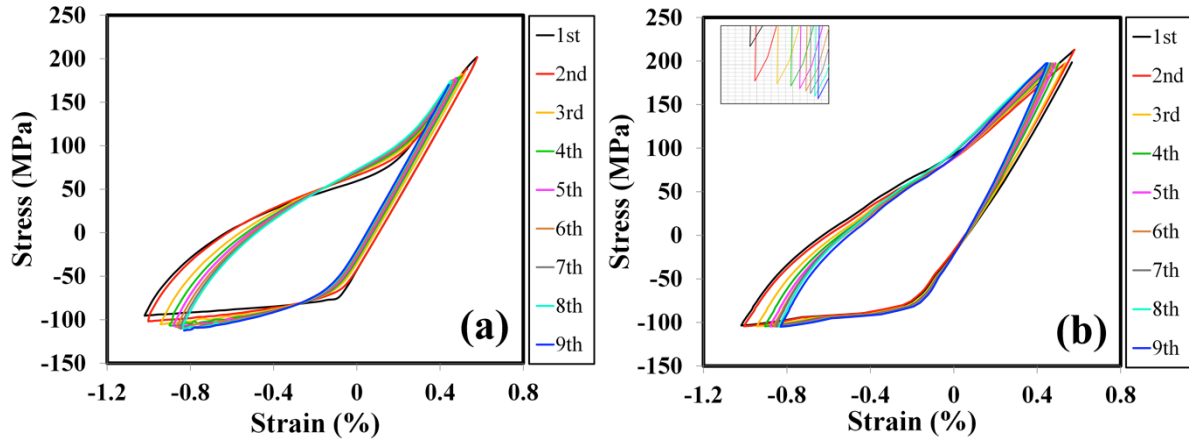
Figure 5-18: a) Proposed strain-control experimental results; b) VMP-FBG response under (M=6.5 Nm) for the first cycle
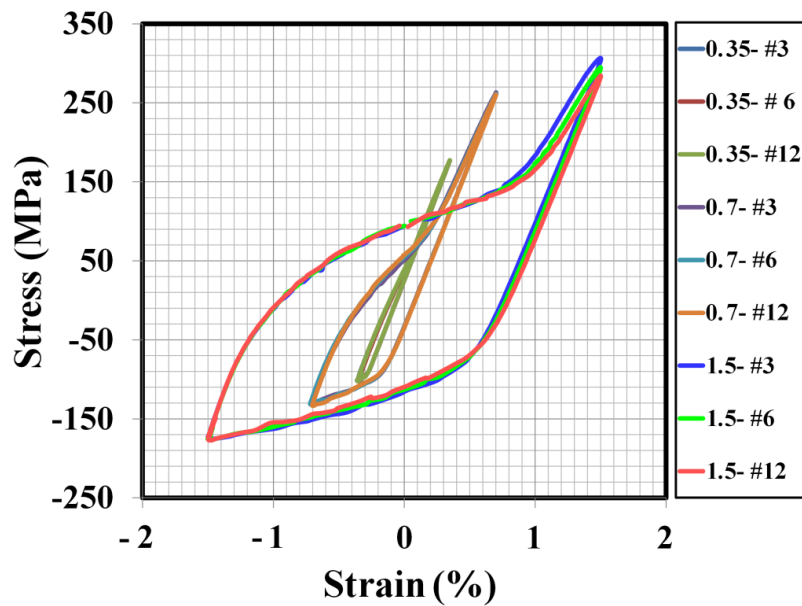
Figure 5-19: Comparison of three cycles of the hysteresis curves under three different strain amplitudes obtained from uniaxial strain-control cyclic tests [16].

Finally, the behaviour of a sample under a bending moment of 5 Nm was investigated. Figure 5-20 shows the VMP simulation results for the first and stabilized cycles, demonstrating that the sample

was plastically deformed in compression. However, the stress induced in the bottom element of the sample was lower than the tensile yield stress; hence, elastic deformation was observed under tensile loading.
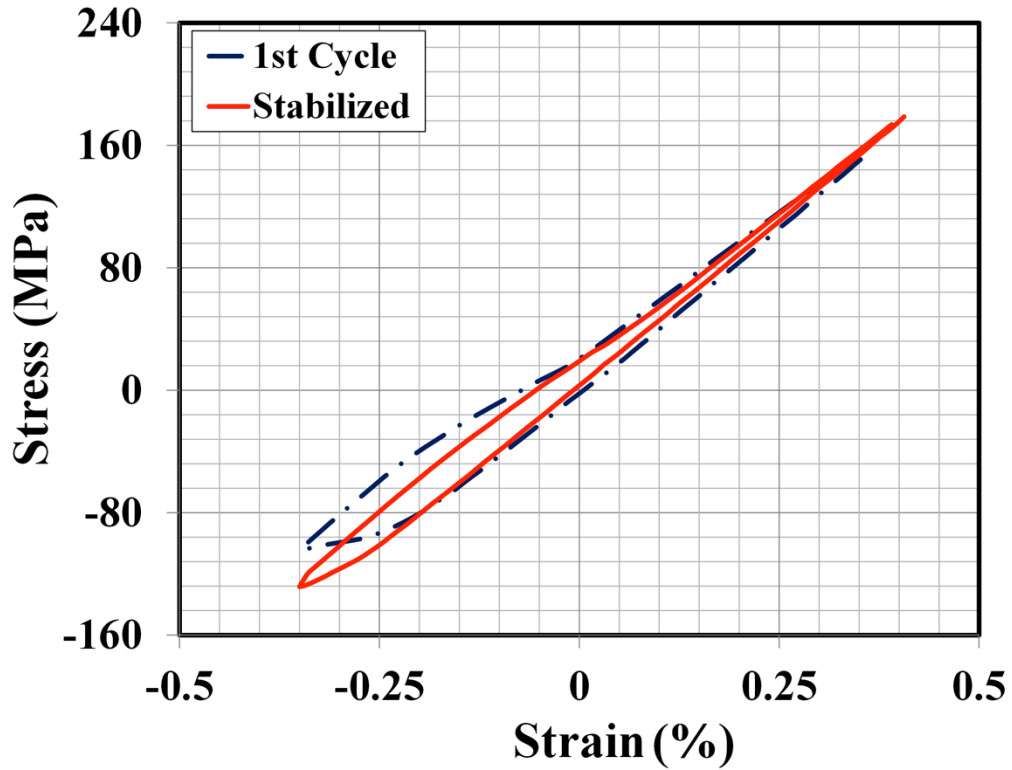
Figure 5-20: VMP hysteresis for the first and the stabilized cycles (5 Nm)

Figure 5-21 depicts the peak and valley strains of the sample, measured by the FBG sensor. The peak strains decreased, and the valley strains increased, as the number of cycles increased. After 500 cycles the FBG sensor failed, therefore, it is difficult to conclude whether the sample became stable or not. However, it was assumed that the sample became stable after the 500 cycles and the VMP stabilized curve was employed to calculate the VMP-FBG hysteresis for this cycle.
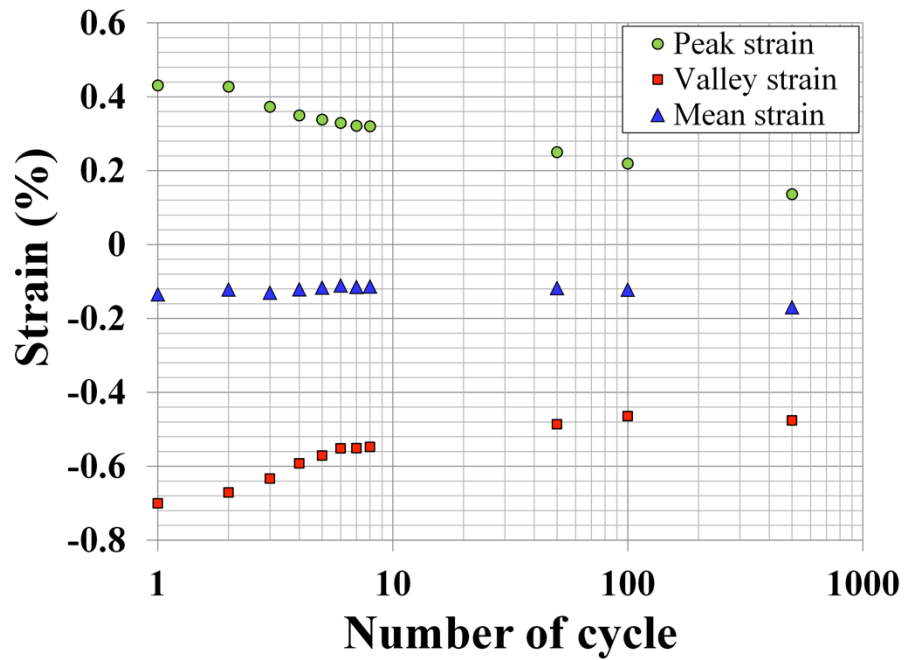
Figure 5-21: Peak and valley strains versus number of cycles (M=5 Nm)

Figure 5-22 illustrates the VMP-FBG hysteresis loops of the sample under the bending moment of 5 Nm. The absolute values of the maximum tensile stress and maximum compressive stress were not equal for each cycle due to the asymmetric behaviour of AZ31B, which is compatible with the previous results. The strain amplitudes were gradually decreased as the number of cycles increased and the stabilized hysteresis curve became narrower and narrower during cyclic loading. Moreover, a negative mean strain of -0.17% remained in the stabilized cycle which demonstrates the asymmetric behaviour of AZ31B alloys. This mean strain confirms that more than half of the cross section of the sample experienced compressive deformation.
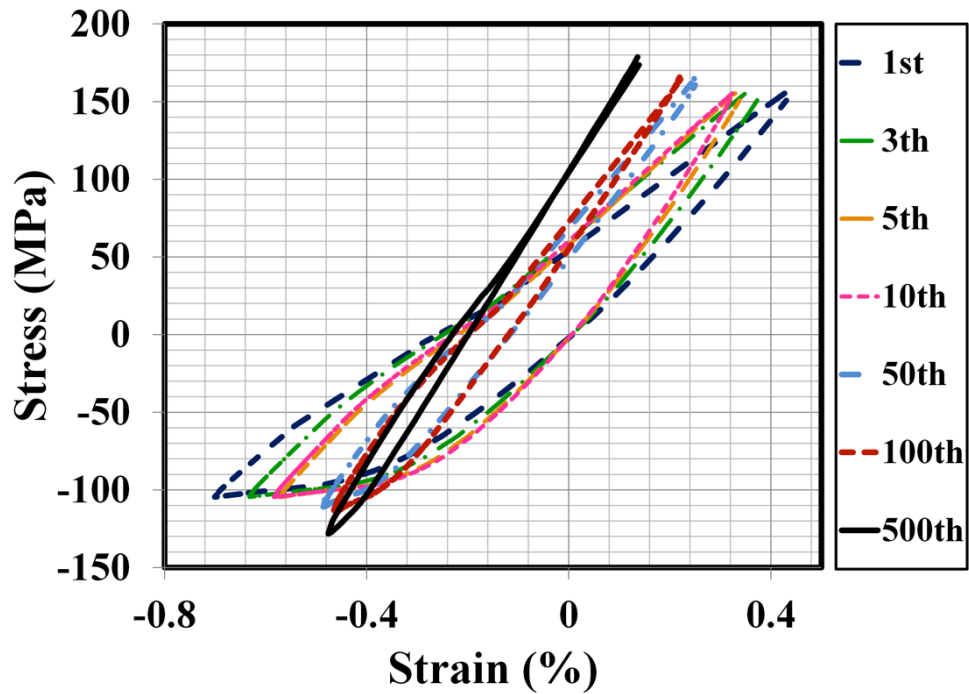
Figure 5-22: VMP-FBG hysteresis curves for different cycles (M=5 Nm)

The fatigue life estimation of the AZ31B sample under three bending moments of 2.5, 5 and 6.5 Nm were calculated based on the energy method. The stabilized VMP-FBG hysteresis curves for these moments were employed to make these calculations. The plastic strain energy density was calculated for each bending moment based on the stabilized hysteresis curve using the Equation (2-13). Then, the positive elastic strain energy was obtained by Equation (2-14), and the results were added to the plastic strain energy to generate the total strain energy densities. According to Equation (2-15), and inserting the energy-based fatigue parameter for AZ31B extrusion (found in material cyclic characteristics listed in Table 5-1 [47, 96], the fatigue life was estimated for the three identified bending moments. To verify the accuracy of VMP-FBG responses of the sample under load-control conditions, the calculated life prediction versus the maximum tensile stresses that the sample experienced during the bending moment were plotted (Figure 5-23). These results were compared with the S-N curve obtained from the RBT experiments for stress relief AZ31B extrusion samples [106]. The comparison results demonstrate that the stabilized VMP-FBG hysteresis using the energy-based approach predicted the life with a good approximation. However, more investigation is required to strengthen the validity of this claim.

Table 5-1: Energy-based fatigue parameters for AZ31B [47, 96]

Elastic regime	
E_f (Fatigue strength coefficient)	5
b (Fatigue strength exponent)	-0.278
Plastic regime	
W_f (Fatigue toughness coefficient)	190
c (Fatigue toughness exponent)	-0.848
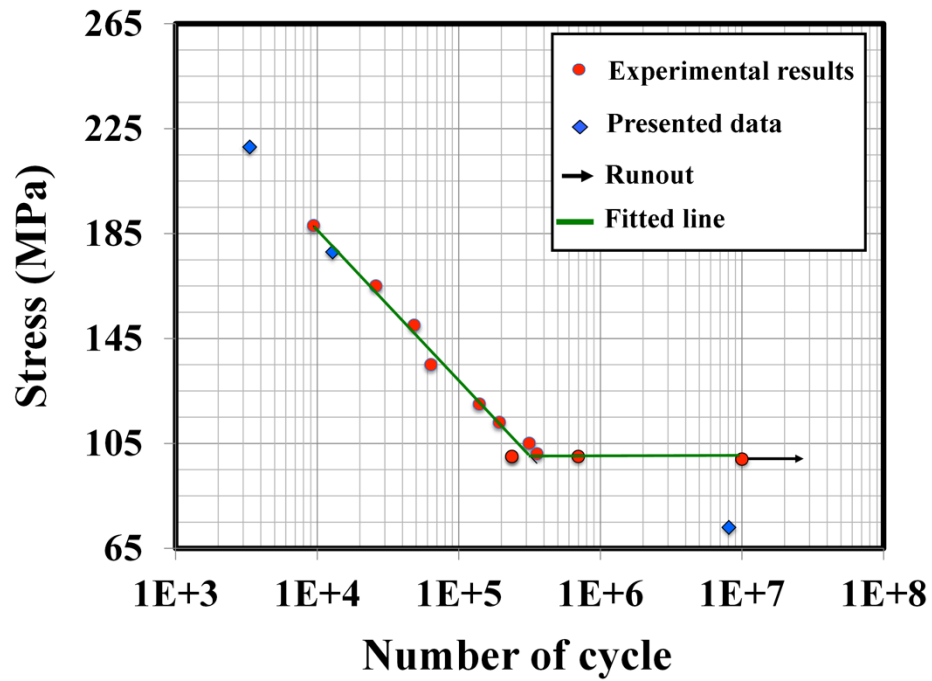
Figure 5-23: Comparison between prediction of life using VMP-FBG hysteresis, and experimental results for stress relief samples

76

Chapter 6

Conclusion and Recommendations for Future Work

6.1 Summary and Conclusion

The present research was conducted to investigate the fatigue behaviour of AZ31B extrusion magnesium alloy under load-control conditions. The load-control condition was approximated through the RBT performed by an RBM. To obtain the cyclic deformation hysteresis of the AZ31B sample, it was necessary to measure the strain and stress during rotating under constant bending moments. An FBG sensor was embedded on the sample to measure the induced strains of the material during rotating. To adhere the sensor, two types of adhesive were tested and the optical epoxy (Norland Optical Adhesive 61) was selected for use in all experiments. The RBM machine was modified for installation of the sample equipped with the FBG sensor. Through this modification, it was possible to rotate the sample with an appropriate frequency compatible with the interrogator, which was used for reading the sensor output. The strain of the sample was measured during bending moments of 2.5, 5, and 6.5 Nm. On the other hand, the cyclic hysteresis loop of the sample under those bending moments was modeled by VMP simulation to find the stress of the hysteresis loops. Finally, the stress-strain hysteresis of the sample under the load-control condition was obtained by combining the strain measured by the FBG sensor and the stress calculated by the VMP simulation. The following is a summary of the results of this project, which is presented here as conclusion:

1) Two different adhesives, thermal epoxy (EPO-TEK 353ND) and optical epoxy (Norland Optical Adhesive 61) were tested to adhere FBG sensors to AZ31B extrusion samples. For each epoxy resin, a curing process was developed to successfully attach the FBG sensors to the substrate. The accuracy of the strain measurements made by the FBG sensors attached with each type of adhesive, was examined in comparison to that of measurements made by standard extensometers. Results confirmed that the FBG sensors precisely measured the strain.

2) The temperature of the sample was monitored during curing of the optical adhesive, which revealed that the sample warmed up to 86°C; however, the temperature and duration of the curing process for the thermal epoxy was much higher than for the optical epoxy. Therefore, for material samples that are sensitive to high temperatures the optical adhesive is preferable.

3) The curing process creates a residual compressive stress on the sample because of the difference between the coefficient of thermal expansion of the sample and the cured adhesive. Based on this observation, the induced residual stress after curing of the optical epoxy was much less than the curing of the thermal epoxy. This residual stress and its related strain should be considered in the further strain measurements.

4) The accuracy of FBG sensor strain measurements was verified through a push-pull test and the use of a calibrated axial extensometer. The results demonstrated that both of the adhesives could be used for strain measurement in elastic and plastic regimes, however, the thermal epoxy generated a stiffer bond and could measure the strain precisely up to 1.3%. In this study, the optical Norland adhesive was selected due to the lower temperature range of curing and its simple curing procedure.

5) The change of the peak and valley strains with respect to the cycles of the sample during rotating bending was obtained. This experiment revealed that under load-control rotating bending, the strain amplitude of the sample decreased as the number of cycles increased and became nearly stable after 2000 cycles when a bending moment of 6.5 Nm was applied to the sample.

6) A large negative mean strain developed in the load-control cyclic tests of magnesium AZ31B. This can be attributed to the asymmetric behaviour of wrought magnesium alloys and the anisotropic yield stress in tension and compression. Similar to stress-control test, ratcheting behaviour was observed during the load-control conditions.

7) The VMP simulation was successfully implemented to calculate the stress-strain hysteresis loops of the stabilized and first cycles of the RBT.

8) A comparison between the strains measured by the FBG sensor and the strains calculated by the VMP simulation, illustrated that the real strains of the sample was larger than the strains predicted by the VMP model. This can be attributed to the simulation method in which the RBT was modeled by fixed beam under alternative loading, and/or the assumption that the CSSC represented the material's properties.

9) The stress evolution of the sample from the first to the stabilized cycle was predicted by linear interpolation between the "stress versus cycle number" curves obtained in the strain-control experiments. The stresses obtained from this approach were used to predict the other hysteresis between the first and stabilized cycles.

10) The VMP-FBG hysteresis loops of the samples were calculated under bending moments of 2.5, 5, and 6.5 Nm for different cycles. These bending moments presented various combinations of elastic and plastic deformations. Based on the VMP-FBG hysteresis curves, when the bending moment is equal to 2.5 Nm, the material is elastically deformed under both tension and compression. By increasing the bending moment to 5 Nm, the VMP-FBG curve revealed that plastic deformation occurred in the sample under compression while the sample was elastically deformed under tension. Finally, by applying a bending moment of 6.5 Nm, the sample was plastically deformed under both tension and compression.

11) To assess the accuracy of the calculated VMP-FBG hysteresis, a strain-control experiment was conducted on the AZ31B extrusion sample based on the peak and valley strains measured by the FBG for the first nine cycles under a bending moment of 6.5 Nm. This experiment revealed that the stress predicted by the VMP simulation was very close to the experimental data. Moreover, the shape of the hysteresis loops predicted by the VMP-FBG model was very similar to the experimental hysteresis curves. This experiment illustrated that the VMP-FBG model can be employed to predict the behaviour of materials under load-control conditions.

12) The fatigue life of the AZ31B sample for three different bending moments (2.5, 5, and 6.5 Nm) was predicted. The energy-based method was employed to estimate the fatigue life of the material by using the calculated total strain energy densities for the stabilized hysteresis

VMP-FBG. These data were compared with the AZ31B experimental S-N curve and showed very good compatibility between the prediction life method and experimental data.

13) The cyclic hysteresis deformation loops of AZ31B extrusion during rotating bending tests were obtained in this research. These hysteresis curves represent the fatigue behaviour of the material under both low- and high-cycle fatigue tests. In load-control condition, the asymmetric behaviour of AZ31B extrusion was observed same as stress-control and strain-control experiments.

6.2 Future Work

In this research, a combined numerical-experimental method was successfully developed to investigate the fatigue behaviour of AZ31B extrusion magnesium alloy under load-control bending tests. To achieve the most accurate results, a list of recommended future research directions is provided below:

1) It was demonstrated that the curing process of the adhesive used to attach the FBG sensors in this research could generate a residual stress in the sample, which may interfere with the actual behaviour of the material. Investigations into adhesives and/or curing, which do not impose residual stresses would enable mounted sensors to more accurately and efficiently measure strains of the sample.

2) In order to obtain more accurate VMP hysteresis loops, more strain-control experiments with strain amplitudes between 0.4% and 0.7% (the region of transition from elastic to plastic deformation) need to be conducted.

3) To predict the unloading curve, it was assumed that the material would follow the strain-control hysteresis curve under load-control conditions. This assumption may not be correct for asymmetric material, as the strain under tension and compression are not equal. The accuracy of this assumption should be investigated experimentally.

4) The accuracy of the VMP-FBG hysteresis loops for the first nine cycles were experimentally examined. The same experiment should be performed for the stabilized hysteresis curves to confirm the precision of the results.

5) To measures the strain of the sample by FBG sensor, the experiments were done in such a way that the sensor experienced tensile stress at the beginning of the first cycle. This test can be done such that the material first undergoes compression. It would be important to conduct future research with a compression starting point as more deformation occurs under compression due to the lower compressive yield stress of AZ31B magnesium alloy and this could affect the findings of all subsequent cycles.

6) To verify the accuracy of the VMP-FBG method for estimating fatigue life based on the energy method, it is necessary that future research be done to collect data reflecting VMP-FBG hysteresis loops at different bending moments.

7) The quadratic mapping function that was employed for replacement FBG strain with VMP strain is not adequate for all hysteresis shapes. More accurate mapping function is needed to construct more realistic hysteresis curves for different bending moments.

Appendix A

Table 5.   The R.R. Moore loading factor chart.

Dia.	Factor	Dia.	Factor	Dia.	Factor	Dia.	Factor	Dia.	Factor	Dia.	Factor	Dia.	Factor	Dia.	Factor
0.050	0.0061	0.100	0.0491	0.150	0.1657	0.200	0.3927	0.250	0.7670	0.300	1.3254	0.350	2.1046	0.400	3.1416
0.051	0.0065	0.101	0.0506	0.151	0.1690	0.201	0.3986	0.251	0.7762	0.301	1.3387	0.351	2.1227	0.401	3.1652
0.052	0.0069	0.102	0.0521	0.152	0.1723	0.202	0.4046	0.252	0.7855	0.302	1.3521	0.352	2.1409	0.402	3.1890
0.053	0.0073	0.103	0.0536	0.153	0.1758	0.203	0.4106	0.253	0.7949	0.303	1.3655	0.353	2.1592	0.403	3.2128
0.054	0.0077	0.104	0.0552	0.154	0.1793	0.204	0.4167	0.254	0.8044	0.304	1.3791	0.354	2.1776	0.404	3.2368
0.055	0.0082	0.105	0.0568	0.155	0.1828	0.205	0.4228	0.255	0.8139	0.305	1.3928	0.355	2.1961	0.405	3.2609
0.056	0.0086	0.106	0.0585	0.156	0.1864	0.206	0.4291	0.256	0.8235	0.306	1.4065	0.356	2.2147	0.406	3.2851
0.057	0.0090	0.107	0.0601	0.157	0.1899	0.207	0.4354	0.257	0.8332	0.307	1.4203	0.357	2.2334	0.407	3.3094
0.058	0.0096	0.108	0.0618	0.158	0.1936	0.208	0.4417	0.258	0.8430	0.308	1.4342	0.358	2.2523	0.408	3.3339
0.059	0.0101	0.109	0.0636	0.159	0.1973	0.209	0.4481	0.259	0.8528	0.309	1.4482	0.359	2.2712	0.409	3.3585
0.060	0.0106	0.110	0.0653	0.160	0.2010	0.210	0.4546	0.260	0.8628	0.310	1.4624	0.360	2.2902	0.410	3.3832
0.061	0.0111	0.111	0.0671	0.161	0.2048	0.211	0.4611	0.261	0.8728	0.311	1.4766	0.361	2.3094	0.411	3.4079
0.062	0.0117	0.112	0.689	0.162	0.2087	0.212	0.4677	0.262	0.8828	0.312	1.4908	0.362	2.3286	0.412	3.4329
0.063	0.0123	0.113	0.0708	0.163	0.2126	0.213	0.4744	0.263	0.8930	0.313	1.5052	0.363	2.3479	0.413	3.4579
0.064	0.0129	0.114	0.0727	0.164	0.2165	0.214	0.4811	0.264	0.9032	0.314	1.5197	0.364	2.3674	0.414	3.4831
0.065	0.0135	0.115	0.0747	0.165	0.2205	0.215	0.4878	0.265	0.9135	0.315	1.5343	0.365	2.3869	0.415	3.5084
0.066	0.0141	0.116	0.0766	0.166	0.2245	0.216	0.4947	0.266	0.9239	0.316	1.5489	0.366	2.4066	0.416	3.5339
0.067	0.0148	0.117	0.0786	0.167	0.2286	0.217	0.5016	0.267	0.9343	0.317	1.5637	0.367	2.4264	0.417	3.5594
0.068	0.0154	0.118	0.0807	0.168	0.2328	0.218	0.5086	0.268	0.9449	0.318	1.5785	0.368	2.4463	0.418	3.5851
0.069	0.0161	0.119	0.0827	0.169	0.2369	0.219	0.5156	0.269	0.9555	0.319	1.5935	0.369	2.4663	0.419	3.6109
0.070	0.0168	0.120	0.0848	0.170	0.2412	0.220	0.5227	0.270	0.9662	0.320	1.6085	0.370	2.4864	0.420	3.6368
0.071	0.0176	0.121	0.0869	0.171	0.2455	0.221	0.5298	0.271	0.9769	0.321	1.6236	0.371	2.5066	0.421	3.6628
0.072	0.0183	0.122	0.0891	0.172	0.2498	0.222	0.5371	0.272	0.9878	0.322	1.6388	0.372	2.5270	0.422	3.6889
0.073	0.0191	0.123	0.0913	0.173	0.2542	0.223	0.5443	0.273	0.9988	0.323	1.6541	0.373	2.5474	0.423	3.7153
0.074	0.0199	0.124	0.0936	0.174	0.2586	0.224	0.5517	0.274	1.0100	0.324	1.6696	0.374	2.5679	0.424	3.7417
0.075	0.0207	0.125	0.0959	0.175	0.2631	0.225	0.5591	0.275	1.0209	0.325	1.6851	0.375	2.5886	0.425	3.7682
0.076	0.0215	0.126	0.0982	0.176	0.2676	0.226	0.5666	0.276	1.0320	0.326	1.7006	0.376	2.6093	0.426	3.7949
0.077	0.0224	0.127	0.1005	0.177	0.2722	0.227	0.5742	0.277	1.0432	0.327	1.7163	0.377	3.6303	0.427	3.8217
0.078	0.0233	0.128	0.1029	0.178	0.2768	0.228	0.5818	0.278	1.0546	0.328	1.7321	0.378	2.6512	0.428	3.8486
0.079	0.0242	0.129	0.1054	0.179	0.2815	0.229	0.5895	0.279	1.0661	0.329	1.7481	0.379	2.6723	0.429	3.8756
0.080	0.0251	0.125	0.0959	0.180	0.2863	0.230	0.5972	0.280	1.0776	0.330	1.7641	0.380	2.6935	0.430	3.9028
0.081	0.0261	0.126	0.0982	0.181	0.2911	0.231	0.6051	0.281	1.0891	0.331	1.7801	0.381	2.7148	0.431	3.9301
0.082	0.0271	0.127	0.1005	0.182	0.2959	0.232	0.6129	0.282	1.1008	0.332	1.7963	0.382	2.7363	0.432	3.9575
0.083	0.0281	0.128	0.1029	0.183	0.3008	0.233	0.6209	0.283	1.1126	0.333	1.8126	0.383	2.7578	0.433	3.9850
0.084	0.0291	0.129	0.1054	0.184	0.3058	0.234	0.6289	0.284	1.1244	0.334	1.8289	0.384	2.7795	0.434	4.0127
0.085	0.0301	0.135	0.1208	0.185	0.3108	0.235	0.6370	0.285	1.1363	0.335	1.8454	0.385	2.8012	0.435	4.0405
0.086	0.0312	0.136	0.1235	0.186	0.3158	0.236	0.6452	0.286	1.1484	0.336	1.8620	0.386	2.8231	0.436	4.0685
0.087	0.0323	0.137	0.1262	0.187	0.3210	0.237	0.6535	0.287	1.1619	0.337	1.8787	0.387	2.8451	0.437	4.0965
0.088	0.0335	0.138	0.1288	0.188	0.3262	0.238	0.6617	0.288	1.1726	0.338	1.8955	0.388	2.8672	0.438	4.1247
0.089	0.0346	0.139	0.1318	0.189	0.3314	0.239	0.6701	0.289	1.1849	0.339	1.9123	0.389	2.8895	0.439	4.1530
0.090	0.0358	0.140	0.1347	0.190	0.3367	0.240	0.6786	0.290	1.1972	0.340	1.9293	0.390	2.9118	0.440	4.1815
0.091	0.0370	0.141	0.1376	0.191	0.3420	0.241	0.6871	0.291	1.2096	0.341	1.9464	0.391	2.9342	0.441	4.2100
0.092	0.0382	0.142	0.1406	0.192	0.3474	0.242	0.6957	0.292	1.2221	0.342	1.9635	0.392	2.9568	0.442	4.2387
0.093	0.0395	0.143	0.1435	0.193	0.3529	0.243	0.7043	0.293	1.2347	0.343	1.9809	0.393	2.9795	0.443	4.2676
0.094	0.0408	0.144	0.1466	0.194	0.3584	0.244	0.7131	0.294	1.2474	0.344	1.9982	0.394	3.0023	0.444	4.2965
0.095	0.0421	0.145	0.1497	0.195	0.3639	0.245	0.7219	0.295	1.2602	0.345	2.0157	0.395	3.0251	0.445	4.3256
0.096	0.0434	0.146	0.1528	0.196	0.3696	0.245	0.7308	0.296	1.2730	0.346	2.0333	0.396	3.0482	0.446	4.3648
0.097	0.0448	0.147	0.1559	0.197	0.3753	0.247	0.7397	0.297	1.2860	0.347	2.0510	0.397	3.0714	0.447	4.3842
0.098	0.0462	0.148	0.1594	0.198	0.3810	0.248	0.7487	0.298	1.2991	0.348	2.0687	0.398	3.0946	0.448	4.4137
0.099	0.0476	0.149	0.1624	0.199	0.3868	0.249	0.7578	0.299	1.3122	0.349	2.0866	0.399	3.1181	0.449	4.4433

Note:

The Loading Factor Chart (Table 5) is in English units. When a metric weight set is used with the machine, be sure to convert the dimension values to English units before using the chart.

Bibliography

1. Miller, W.S., et al., *Recent developement in aluminium alloys for the automotive industry.* Materials Science & Engineering A, 2000. **280**(1): p. 37-49.
2. Blawert, C., N. Hort, and K.U. Kainer, *Automotive applications of magnesium and its alloys.* Trans. Indian Inst. Met., 2004. **57** (4): p. 397-408.
3. Gupta, M. and N.M.L. Sharon, *Magnesium, Magnesium Alloys, and Magnesium Composites.* 2011: Wiley.
4. Friedrich, H. and S. Schumann, *Research for a new age of magnesium in the automotive industry.* Journal of Materials Processing Technology, 2001. **117**(3): p. 276-281.
5. Avedesian, M.M. and H. Baker, *ASM Specialty Handbook: Magnesium and Magnesium Alloys,.* 1999: Asm International.
6. Kulekci, M.K., *Magnesium and its alloys applications in automotive industry.* The International Journal of Advanced Manufacturing Technology, 2008. **39**(9-10): p. 851-865.
7. Fuchs, H.O. and R.I. Stephens, *Metal Fatigue in Engineering,.* 1980, New York: Wiley.
8. Hasegawa, S., et al., *Evaluation of low cycle fatigue life in AZ31 magnesium alloy.* International Journal of Fatigue, 2007. **29**: p. 1839–1845.
9. Park, S.H., et al., *Low-cycle fatigue characteristics of rolled Mg-3Al-1Zn alloy.* International Journal of Fatigue, 2010. **32**(11): p. 1835-1842.
10. Jordon, J.B., et al., *Effect of twinning, slip, and inclusions on the fatigue anisotropy of extrusion-textured AZ61 magnesium alloy.* Materials Science and Engineering a-Structural Materials Properties Microstructure and Processing, 2011. **528**(22-23): p. 6860-6871.
11. Lou, X.Y., et al., *Hardening evolution of AZ31B Mg sheet.* International Journal of Plasticity, 2007. **23**(1): p. 44-86.
12. Li, M., et al., *An efficient constitutive model for room-temperature, low-rate plasticity of annealed Mg AZ31B sheet.* International Journal of Plasticity, 2010. **26**(6): p. 820-858.
13. Wu, L., et al., *The effects of texture and extension twinning on the low-cycle fatigue behaviour of a rolled magnesium alloy, AZ31B.* Materials Science and Engineering a-Structural Materials Properties Microstructure and Processing, 2010. **527**(26): p. 7057-7067.
14. Wu, L., et al., *Internal stress relaxation and load redistribution during the twinning–detwinning-dominated cyclic deformation of a wrought magnesium alloy, ZK60A.* Acta Materialia, 2008. **56**(14): p. 3699-3707.
15. Yu, Q., J. Zhang, and Y. Jiang, *Direct observation of twinning–detwinning–retwinning on magnesium single crystal subjected to strain-controlled cyclic tension–compression in [0 0 0 1] direction.* Philosophical Magazine Letters, 2011. **91**(12): p. 757-765.
16. Albinmousa, J., *Multiaxial Fatigue Characterization and Modeling of AZ31B Magnesium Extrusion*, in *Mechanical Engineering*. 2011, University of Waterloo: Waterloo.
17. Stephens, R.I., et al., *Metal Fatigue in Engineering*. 2nd ed. 2001: Wiley.
18. Dowling, N.E., *Mechanical Behaviour of Materials: Engineering Methods for Deformation, Fracture, and Fatigue*. 4th ed. 2012: Prentice Hall.
19. Jahed, H. and R.N. Dubey, *An Axisymmetric Method of Elastic-Plastic Analysis Capable of Predicting Residual Stress Field.* Transactions of the ASME, 1997. **119**: p. 264-273.
20. Knight, D., *Oxford Dictionary of National Biography*. 2004: Oxford University Perss.
21. Mordike, B.L. and T. Ebert, *Magnesium: Properties-applications-potential.* Materials Science & Engineering A, 2001. **302**(1): p. 37-45.
22. Ashby, M.F., *Materials Selection in Mechanical Design*. 2007: Elsevier.
23. Emley, E.F., *Principles of Magnesium Technology*. 1966: Oxford Pergamon Press Inc.

24.   Watarai, H., *Trend of research and development for magnesium alloys-reducing the weight of structural materials in motor vehicles.* Science and Technology Trends, 2006. **18**: p. 84-87.

25.   Luo, A., *Magnesium: Current and potential automotive applications.* JOM Journal of the Minerals, Metals and Materials Society, 2002. **52**(2).

26.   Roberts, C.S., *Magnesium and its alloys.* 1960: Wiley.

27.   Graff, S., W. Brocks, and D. Steglich, *Yielding of magnesium: From single crystal to polycrystalline aggregates.* International Journal of Plasticity, 2007. **23**(12): p. 1957-1978.

28.   Gharghouri, M.A., et al., *Study of the mechanical properties of Mg-7.7at.% Al by in-situ neutron diffraction.* Philosophical Magazine A, 1999. **79**(7): p. 1671-1695.

29.   Cáceres, C.H. and P. Lukáč, *Strain hardening behaviour and the Taylor factor of pure magnesium.* philosophical Magazine, 2008. **88**(7): p. 977-989.

30.   Staroselsky, A. and L. Anand, *A constitutive model for hcp materials deforming by slip and twinning.* International Journal of Plasticity, 2003. **19**(10): p. 1843-1864.

31.   Oppedal, A.L., et al., *Effect of dislocation transmutation on modeling hardening mechanisms by twinning in magnesium.* International Journal of Plasticity, 2012. **30-31**(41-46).

32.   Huppmann, M., et al., *Analyses of deformation twinning in the extruded magnesium alloy AZ31 after compressive and cyclic loading.* Journal of Materials Science, 2011. **46**(4): p. 938-950.

33.   Polmear, I., *Light Alloys: from Traditional Alloys to Nanocrystals.* 2006: Butterworth-Heinemann.

34.   Bettles, C. and M. Gibson, *Current Wrought Magnesium Alloys: Strengths and Weaknesses.* JOM Journal of the Minerals, Metals and Materials Society, 2005. **57**(5): p. 46-49.

35.   Kainer, K.U., *Magnesium Alloys and Technologies* 2003: Wiley-VCH.

36.   Shih, T., W. Liu, and Y. Chen, *Fatigue of as-extruded AZ61A magnesium alloy.* Materials Science and Engineering A, 2002. **325**(1-2): p. 152-162.

37.   Zhihao, Z., M. Yi, and C. Jianzhong, *Effect of Mn on microstructures and mechanical properties of Al-Mg-Si-Cu-Cr-V alloy.* China Foundry, 2012. **9**(4): p. 349-355.

38.   ASTM, *Standard Practice for Codification of Unalloyed Magnesium and Magnesium-Alloys, Cast and Wrought.* 2011.

39.   Ishihara, S., Z. Nan, and T. Goshima, *Effect of microstructure on fatigue behaviour of AZ31 magnesium alloy.* Materials Science and Engineering: A, 2007. **468–470**(0): p. 214-222.

40.   Nan, Z.Y., et al., *On the sharp bend of the S-N curve and the crack propagation behaviour of extruded magnesium alloy.* Scripta Materialia, 2007. **56**(8): p. 649-652.

41.   Ochi, Y., et al., *High-cycle rotating bending fatigue property in very long-life regime of high-strength steels.* Fatigue & Fracture of Engineering Materials & Structures, 2002. **25**(8-9): p. 823-830.

42.   Tosha, K., et al., *A study on P-S-N curve for rotating bending fatigue test for bearing steel.* Tribology Transactions, 2008. **51**(2): p. 166-172.

43.   Zhao, A., et al., *Effects of strength level and loading frequency on very-high-cycle fatigue behaviour for a bearing steel.* International Journal of Fatigue, 2012. **38**: p. 46-56.

44.   Smith, R.N., P. Watson, and T.H. Topper, *A stress-strain function for the fatigue of metal.* J. Mater., 1970. **5**(5): p. 767-778.

45.   Lorenzo, F. and C. Laird, *A new approach to predicting fatigue life behaviour under the action of mean stresses.* Mater. Sci. and Eng., 1984. **62**(2): p. 205-210.

46.   Beer, F., E.R. Johnston, and J.T. Dewolf, *Mechanics of Materials.* 4th ed. 2006: McGraw Hill.

47.   Albinmousa, J., H. Jahed, and S. Lambert, *Cyclic behaviour of wrought magnesium alloy under multiaxial load.* International Journal of Fatigue, 2011. **33**(8): p. 1127-1139.

48. Noster, U. and B. Scholtes, *Stress-controlled fatigue of magnesium wrought alloy AZ31 in the temperature range 20-300 degrees C.* Zeitschrift Fur Metallkunde, 2001. **92**(3): p. 260-264.

49. Begum, S., et al., *Effect of strain ratio and strain rate on low cycle fatigue behaviour of AZ31 wrought magnesium alloy.* Materials Science and Engineering a-Structural Materials Properties Microstructure and Processing, 2009. **517**(1-2): p. 334-343.

50. Begum, S., et al., *Strain-Controlled Low-Cycle Fatigue Properties of a Newly Developed Extruded Magnesium Alloy.* Metallurgical and Materials Transactions a-Physical Metallurgy and Materials Science, 2008. **39A**(12): p. 3014-3026.

51. GENG, C.-j., et al., *Low cycle fatigue behaviour of extruded AZ31B magnesium alloy.* Trans. Nonferrous Met. Soc. China, 2013. **23**: p. 1589-1594.

52. Lv, F., et al., *Fatigue properties of rolled magnesium alloy (AZ31) sheet: Influence of specimen orientation.* International Journal of Fatigue, 2011. **33**(5): p. 672-682.

53. Park, S.H., S.-G. Hong, and C.S. Lee, *Enhancing in-plane fatigue resistance of rolled AZ31 magnesium alloy by pre-straining*, in *Magnesium Technology 2009*, E.A. Nyberg, et al., Editors. 2009. p. 71-76.

54. Mirza, F.A., et al., *Effect of strain ratio on cyclic deformation behaviour of a rare-earth containing extruded magnesium alloy.* Materials Science and Engineering a-Structural Materials Properties Microstructure and Processing, 2013. **588**: p. 250-259.

55. Mirza, F.A., et al., *Low cycle fatigue of a rare-earth containing extruded magnesium alloy.* Materials Science and Engineering a-Structural Materials Properties Microstructure and Processing, 2013. **575**: p. 65-73.

56. Kang, G., et al., *Uniaxial ratchetting of extruded AZ31 magnesium alloy: Effect of mean stress.* Materials Science & Engineering A, 2014. **607**: p. 318-327.

57. Albinmousa, J., H. Jahed, and S. Lambert, *Monotonic and multiaxial cyclic behaviour of the extruded az31b magnesium alloy*, in *Magnesium Technology 2010*, S.R. Agnew, et al., Editors. 2010. p. 261-266.

58. Xiong, Y., Q. Yu, and Y. Jiang, *An experimental study of cyclic plastic deformation of extruded ZK60 magnesium alloy under uniaxial loading at room temperature.* International Journal of Plasticity, 2014. **53**: p. 107-124.

59. Zhang, J., et al., *An experimental study of cyclic deformation of extruded AZ61A magnesium alloy.* International Journal of Plasticity, 2011. **27**(5): p. 768-787.

60. Abbaschian, R., L. Abbaschian, and R.E. Reed-Hill, *Physical Metallurgy Principles*. 2008: Cengage Learning.

61. Hertzberg, R., *Deformation and fracture mechanics of engineering materials*. 4th ed. 1996: Wiley.

62. Suresh, S., *Fatigue of materials*. 2nd ed. 1998: Cambridge University Press.

63. Lv, F., et al., *Effects of hysteresis energy and mean stress on low-cycle fatigue behaviours of an extruded magnesium alloy.* Scripta Materialia, 2011. **65**(1): p. 53-56.

64. Shiozawa, K., et al., *Low-Cycle Fatigue Deformation Behaviour and Evaluation of Fatigue Life on Extruded Magnesium Alloys*, in *11th International Conference on the Mechanical Behaviour of Materials*, M. Guagliano and L. Vergani, Editors. 2011. p. 1244-1249.

65. Wu, L., et al., *Twinning–detwinning behaviour during the strain-controlled low-cycle fatigue testing of a wrought magnesium alloy, ZK60A.* Acta Materialia, 2008. **56**(4): p. 688-695.

66. Yin, S.M., et al., *Influence of Grain Size and Texture on the Yield Asymmetry of Mg-3Al-1Zn Alloy.* Journal of Materials Science & Technology, 2011. **27**(1): p. 29-34.

67. Lv, F., et al., *Tensile and low-cycle fatigue properties of Mg-2.8% Al-1.1% Zn-0.4% Mn alloy along the transverse and rolling directions.* Scripta Materialia, 2009. **61**(9): p. 887-890.

68. Yin, S.M., et al., *Cyclic deformation behaviour of as-extruded Mg-3%Al-1%Zn.* Scripta Materialia, 2008. **58**(9): p. 751-754.

69. Lin, Y.C., et al., *Investigation of uniaxial low-cycle fatigue failure behaviour of hot-rolled AZ91magnesium alloy.* International Journal of Fatigue, 2013. **48**: p. 122-132.

70. Udd, E. and W.B. Spillman, *Fiber Optic Sensors: An Introduction to Engineer and Scientists.* 2nd ed. 2011: Wiley.

71. Ha, J.-H., P. Muralidharan, and D.K. Kim, *Hydrothermal synthesis and characterization of self-assembled h-WO3 nanowires/nanorods using EDTA salts.* Journal of Alloys and Compounds, 2009: p. 446–451.

72. Werneck, M.M., et al., *A Guide to Fiber Bragg Grating Sensors.* Current Trends in Short- and Long-period Fiber Gratings, ed. C. Cuadrado-Laborde. 2013: InTech.

73. Hill, K.O., et al., *Photosensitivity in optical fiber waveguides: Application to reflection filter fabrication.* Appl. Phys. Lett., 1973. **32**(10): p. 647-649.

74. Meltz, G., W.W. Morey, and W.H. Glenn, *Formation of Bragg gratings in optical fibers by a transverse holographic method.* Optics Letters, 1989. **14**(15): p. 823-825.

75. Kreuzer, M., *Strain Measurement with Fiber Bragg Grating Sensors*, HBM, Editor: Darmstadt, Germany.

76. Erdogan, T., *Fiber Grating Spectra.* Light. Technol. J., 1997. **15**(8): p. 1277-1294.

77. Canning, J., *Fiber Grating and Devices for Sensors and Lasers.* Lasers and Photonics Review, 2008. **2**(4): p. 275-289.

78. Erdogan, T., *Fiber Grating Spectra.* Journal of Lightwave Technology, 1997. **15**(8): p. 1277-1294.

79. Dockney, J.M. and R. Tatam, *Simultaneous independent temperature and strain measurement using in-fiber Bragg grating sensors.* Electronic Letter, 1996. **32**(12).

80. Jülich, F., et al., *Gauge factors of fibre Bragg grating strain sensors in different types of optical fibres.* Measurement Science and Technology, 2013. **24**(9): p. 094007 (1-7).

81. Montero, A., et al., *Fiber Bragg Gratings, IT Techniques and Strain Gauge Validation for Strain Calculation on Aged Metal Specimens.* Sensors, 2011. **11**(1): p. 1088-1104.

82. Maron, R. and A. Kersey, *Multi-parameter fiber optic sensor for use in harsh environments*, U. Pat., Editor. 1999.

83. Wnuk, V.P., et al., *Process for mounting and packaging of Fiber Bragg Grating strain sensors for use in harsh environment application*, in *Smart structures conference, SPIE.* 2005. p. 5758-6.

84. Brotzu, A., et al., *Use of Fiber Optic sensors for monitoring crack growth in fatigue and corrosion-fatigue tests.* Advance Materials Research, 2008. **38**: p. 166-160.

85. Gu, X., et al., *Application of Flat-Clad Optical Fiber Bragg Grating Sensor in Characterization of Asymmetric Fatigue Deformation of Extruded Magnesium Alloy.* Ieee Sensors Journal, 2011. **11**(11): p. 3042-3046.

86. Feng, A., et al., *Flat-Cladding Fiber Bragg Grating Sensors for Large Strain Amplitude Fatigue Tests* sensors 2010. **10**: p. 7674-7680.

87. Fokin, M., *Underlying mechanisms, applications, and limitations of chemical composition gratings in silica based fibers.* Journal of Non-Crystalline Solids, 2004. **349**: p. 98-104.

88. Li, C., et al., *Localized Cyclic Strain Measurements of Friction Stir Welded Aluminum Alloy Using a Flat-Clad Optical Fiber Sensor Array.* IEEE Sensors Journal, 2010. **10**(4): p. 888-892.

89. Jahed, H. and G. Ghanbari, *Actual Unloading Behaviour and Its Significance on Residual Stress in Machined Autofrettaged Tubes.* Journal of Pressure Vessel Technology, 2003. **125**(3): p. 321.

90.   Kalatehmollaei, E., H. Mahmoudi-Asl, and H. Jahed, *An asymmetric elastic–plastic analysis of the load-controlled rotating bending test and its application in the fatigue life estimation of wrought magnesium AZ31B.* International Journal of Fatigue, 2014. **64**: p. 33–41.

91.   Lin, X.Z. and D.L. Chen, *Strain controlled cyclic deformation behaviour of an extruded magnesium alloy.* Materials Science and Engineering a-Structural Materials Properties Microstructure and Processing, 2008. **496**(1-2): p. 106-113.

92.   Begum, S., et al., *Low cycle fatigue properties of an extruded AZ31 magnesium alloy.* International Journal of Fatigue, 2009. **31**: p. 726–735.

93.   Albinmousa, J. and H. Jahed, *Multiaxial effects on LCF behaviour and fatigue failure of AZ31B magnesium extrusion.* International Journal of Fatigue, 2014.

94.   Park, S.H., et al., *Effect of anisotropy on the low-cycle fatigue behaviour of rolled AZ31 magnesium alloy.* Materials Science and Engineering a-Structural Materials Properties Microstructure and Processing, 2010. **527**(3): p. 417-423.

95.   Jahed, H., et al., *An energy-based fatigue life assessment model for various metallic materials under proportional and non-proportional loading conditions.* International journal of fatigue, 2007. **29**(4): p. 647-655.

96.   Albinmousa, J., H. Jahed, and S. Lambert, *Cyclic axial and cyclic torsional behaviour of extruded AZ31B magnesium alloy.* International Journal of Fatigue, 2011. **33**(11): p. 1403-1416.

97.   *Metals Handbook.* 9th ed. Vol. 2. 1989: ASM.

98.   Manual, *Model R.R. Moore High speed Rotating Beam Fatigue Testing Machine.* 2004, Instron.

99.   Liang, T.Y.R., *Dual-Parameter Opto-Mechanical Fiber Optic Sensors for Harsh Environment Sensing: Design, Packaging, Calibration, and Applications*, in *Mechanical Engineering.* 2014, University Of Waterloo.

100.   *Technical Data Sheet: 353ND*: , EPO-TEK.

101.   *Technical Data Sheet: Norland Optical Adhesive 61*: Norland Products.

102.   Hassan, T. and Z. Liu, *On the Difference of Fatigue Strengths from Rotating bending, Four point Bending, and Contilever bending tests.* pressure Vessels and Piping, 2001. **78**: p. 19-30.

103.   Manson, S.S., *Fatigue: a complex subject - some simple approximations.* Experimental Mechanic, 1965. **5**: p. 193-226.

104.   Palin-Luc, T. and S. Lasserre, eds. *High cycle multiaxial fatigue energy criterion taking into account the volume distribution of stresses*. Multiaxial fatigue and fracture, ed. E. Macha, W. Bedkowski, and T. Lagoda. 1999, Elsevier.

105.   Hama, T., et al., *Work-hardening behaviours of magnesium alloy sheet during in-plane cyclic loading.* Materials Science and Engineering: A, 2012. **551**: p. 209-217.

106.   Mahmoudi-Asl, H., *The Effect of Residual Stress Induced by Cold Spray Coating of Fatigue Life of Magnesium Alloy, AZ31B*, in *Mechanical Engineering.* 2011, University of Waterloo.